

A neural state of resilience? Encoding resilience as set points of cortical microcircuit activity

Dissertation
zur Erlangung des Doktorgrades des
Dr. rer. nat.

Am Fachbereich Biologie
der Johannes Gutenberg-Universität Mainz

Vorgelegt von

Hendrik Andreas Backhaus
Geboren am 30.04.1986 in Darmstadt, Deutschland

Mainz, 08.10.2024

Dekan: [REDACTED]

1. Betreuerin: [REDACTED]

2. Betreuer: [REDACTED]

1. Gutachter: [REDACTED]

2. Gutachter: [REDACTED]

Tag der mündlichen Prüfung: 18.02.2025

"[...] These creatures you call mice, you see, they are not quite as they appear. They are merely the protrusion into our dimension of vast hyperintelligent pandimensional beings. The whole business with the cheese and the squeaking is just a front."

The old man paused, and with a sympathetic frown continued.

"They've been experimenting on you, I'm afraid."

— Douglas Adams

I. Abstract

Stress resilience describes the capability of an individual to maintain mental health during or after traumatic, stressful or emotionally challenging situations or to return to a mental state similar to that before the crisis onset. The aim of resilience research is to identify mechanisms that enables an individual to maintain mental health, rather than developing mental disorders and has increasingly come into focus. Studies indicate that resilience is an active adaptive process and not just the absence of symptoms observed in individuals who are deficient in these defense mechanisms and therefore susceptible to stressors. Up to date, no universal concept to grasp resilience exists, but several mechanisms that putatively contribute to stress-resilient or -susceptible behavioral phenotypes were identified. In humans, psychological and socio-environmental factors as adaptive coping and social support can contribute to the maintenance of normal psychological function and avoid serious mental illness, but also a wide range of neurobiological markers such as changes in the neuroendocrinological system or genetic factors have been associated with resilience. Yet, to which extend stress resilience is reflected in a differing functional architecture of neuronal network activity remained largely unexplored. There is evidence of hyperactive neuronal network activity within networks of the primary visual cortex (V1) in animal models of multiple sclerosis, Huntington's or Alzheimer disease, present long before phenotypic changes become measurable at the behavioral level. It is hypothesized that changes in network activity do not serve the purpose to preserve long-term functionality to achieve behavioral functionality but instead aim for short-term stability to maintain the *status quo* of network function, coining the term of a selfish network. There is mounting evidence that the historic view on brain architecture of distinct brain regions executing well-defined tasks, does not accurately describe brain functionality. Instead, brain regions such as the sensory cortices are considered not only to process incoming sensory stimuli, but also contribute to action execution and decision making, forming a

functionally bound brain. The V1 poses a well suitable brain region to probe for network dysregulations as it receives information from other sensory cortices, locomotion and areas related to emotion.

This thesis aims to elucidate the concept of stress-resilience on the level of neuronal networks within V1 in a mouse model of chronic social stress. Mice are subjected to a behavioral paradigm of chronic social defeat (CSD). The behavioral phenotype is assessed by a social interaction-test (SI-test), dividing the population into a resilient and susceptible behavioral phenotype. Furthermore, a subgroup of mice which is not undergoing CSD is used to answer the question if non-stressed animals show neuronal network patterns comparable to resilient or susceptible animals, or whether they represent a third distinct network state. Neuronal network activity is measured in the awake behaving animal on single cell level in V1 layer II/III employing two-photon functional calcium imaging. The assessment of both spontaneous and sensory-evoked neuronal activity is used to obtain a fine-grained picture of the local functional architecture of a network. For improving the sensitivity of the detection of putative network dysregulation, the two-photon functional calcium imaging analysis pipeline has been streamlined and improved, for optimizing the correlation of calcium transient to underlying neuronal action potentials. Lastly, a three-photon functional calcium imaging microscope is implemented and imaging quality is compared with two-photon microscopy modalities.

It was found that the newly developed analysis pipeline outperforms commonly used analysis routines. Employed to functional calcium imaging data in a mouse model of chronic social defeat, neuronal networks in resilient classified animals exhibit lower spontaneous activity and a more accurate representation of visual afferents compared to susceptible litter mates. Non-stressed animals exhibit network activity close to the dynamics of susceptible animals, both in spontaneous network activity as well as in the representation of visual afferents. Lastly, employing three-photon microscopy revealed

an increase of the penetration depth at the cost of imaging frequency and size of the resolved field of view.

The findings underline the importance of the development of analysis routines capable of accurately capturing single cell activity to describe neuronal network patterns. In the field of resilience research, the results suggest that architectures of neuronal networks within sensory cortices itself might constitute a resilience mechanism, contributing to the outcome of a resilient or susceptible behavioral phenotype. Finally, the first datasets collected using three-photon microscopy represent a promising opportunity to resolve neuronal networks in deeper regions such as layer V of V1.

II. Zusammenfassung

Stressresilienz beschreibt die Fähigkeit eines Individuums, psychische Gesundheit während oder nach traumatischen, belastenden oder emotional herausfordernden Situationen aufrechtzuerhalten oder zu einem ähnlichen psychischen Zustand zurückzukehren wie vor Ausbruch der Krise. Ziel der Resilienzforschung ist es, Mechanismen zu ermitteln, die es einer Person ermöglichen, ihre psychische Gesundheit zu erhalten, anstatt psychische Störungen zu entwickeln, die zunehmend in den Blickpunkt rücken. Studien deuten darauf hin, dass Resilienz ein aktiver Anpassungsprozess ist und nicht nur das Fehlen von Symptomen, die bei Personen zu beobachten ist, denen es an diesen Abwehrmechanismen mangelt und die daher anfällig für Stressoren sind. Bislang gibt es kein universelles Konzept zur Erfassung der Resilienz, aber es wurden mehrere Mechanismen identifiziert, die vermutlich zu stressresistenten oder -anfälligen Verhaltensphänotypen beitragen. Beim Menschen können psychologische und sozio-ökologische Faktoren wie adaptive Bewältigung und soziale Unterstützung zur Aufrechterhaltung normaler psychologischer Funktionen und zur Vermeidung schwerer psychischer Erkrankungen beitragen, aber auch ein breites Spektrum neurobiologischer Marker wie Veränderungen im neuroendokrinen System oder genetische Faktoren wurden mit Resilienz in Verbindung gebracht. Inwieweit sich die Stressresilienz jedoch in einer unterschiedlichen funktionellen Architektur der neuronalen Netzwerkaktivität widerspiegelt, ist noch weitgehend unerforscht. In Tiermodellen der Multiplen Sklerose, der Huntington- oder der Alzheimer-Krankheit gibt es Hinweise auf eine hyperaktive neuronale Netzwerkaktivität in Netzwerken des primären visuellen Kortex (V1), die lange vor den auf der Verhaltensebene messbaren phänotypischen Veränderungen auftreten. Es wird angenommen, dass Veränderungen in der Netzwerkaktivität nicht dem Zweck dienen, die langfristige Funktionalität zu erhalten, um eine Verhaltensfunktionalität zu gewährleisten, sondern stattdessen auf eine kurzfristige Stabilität abzielen, um den

Status quo der Netzwerkfunktion aufrechtzuerhalten, wodurch der Begriff des „selfish networks“ geprägt wurde. Es gibt immer mehr Belege dafür, dass die historische Sichtweise auf die Gehirnarchitektur, wonach bestimmte Gehirnregionen genau definierte Aufgaben ausführen, die Funktionalität des Gehirns nicht genau beschreibt. Stattdessen wird davon ausgegangen, dass Hirnregionen wie die sensorischen Kortizes nicht nur eingehende sensorische Reize verarbeiten, sondern auch zur Ausführung von Handlungen und zur Entscheidungsfindung beitragen und somit ein funktionell verwobenes Gehirn bilden. V1 stellt eine gut geeignete Hirnregion für die Untersuchung von Netzwerkdysregulationen dar, da dieser Informationen von anderen sensorischen Kortizes erhält, sowie von Bereichen, die mit Bewegungen und Emotionen assoziiert sind. Ziel dieser Arbeit ist es, das Konzept der Stressresilienz auf der Ebene neuronaler Netzwerke innerhalb von V1 in einem Mausmodell für chronischen sozialen Stress zu erforschen. Mäuse werden einem Verhaltensparadigma der chronischen sozialen Niederlage (CSD) unterzogen. Der Verhaltensphänotyp wird anhand eines sozialen Interaktionstests (SI-Test) bewertet, wobei die Population in einen resilienten und einen anfälligen Verhaltensphänotyp unterteilt wird. Darüber hinaus wird eine Untergruppe von Mäusen, die keinen CSD durchläuft, verwendet, um die Frage zu beantworten, ob die nicht gestressten Tiere neuronale Netzwerkuster aufweisen, die mit denen der resilienten oder anfälligen Tiere vergleichbar sind, oder ob sie einen dritten unterschiedlichen Netzwerkzustand darstellen. Die neuronale Netzwerkaktivität wird im wachen Tier auf Einzelzellebene in der V1-Schicht II/III mit Hilfe der funktionellen Zwei-Photonen-Kalzium-Bildgebung gemessen. Die Bewertung sowohl der spontanen als auch der sensorisch evozierten neuronalen Aktivität wird verwendet, um ein detailliertes Bild der lokalen funktionellen Architektur eines Netzwerks zu erhalten. Um die Sensitivität der Erkennung von Netzwerkdysregulationen zu verbessern, wurde die Analysepipeline der funktionellen Zwei-Photonen-Kalzium-Bildgebung vereinheitlicht und verbessert, um die Korrelation

der Kalziumtransienten mit den zugrunde liegenden neuronalen Aktionspotenzialen zu optimieren. Schließlich wurde ein Drei-Photonen-Mikroskop für die funktionelle Kalzium-Bildgebung implementiert und die Qualität der Bildgebung mit den Modalitäten der Zwei-Photonen-Mikroskopie verglichen.

Es wurde festgestellt, dass die neu entwickelte Analysepipeline die üblicherweise verwendeten Analyseroutinen übertrifft. Bei der Anwendung auf funktionelle Kalzium-Bildgebungsdaten in einem Mausmodell chronischer sozialer Niederlagen zeigen neuronale Netzwerke in resilient klassifizierten Tieren eine geringere spontane Aktivität und eine genauere Darstellung der visuellen Afferenzen im Vergleich zu suszeptiblen Mäusen. Nicht gestresste Tiere weisen eine Netzwerkaktivität auf, die der Dynamik stresssuszeptibler Tiere nahe kommt, sowohl bei der spontanen Netzwerkaktivität als auch bei der Repräsentation der visuellen Afferenzen. Schließlich ergab die Anwendung der Drei-Photonen-Mikroskopie eine Erhöhung der Eindringtiefe auf Kosten der Bildgebungsfrequenz und der Größe des aufgelösten Sichtfelds.

Die Ergebnisse unterstreichen die Bedeutung der Entwicklung von Analyseroutinen, die in der Lage sind, die Aktivität einzelner Zellen genau zu erfassen, um neuronale Netzwerkmodelle zu beschreiben. Im Bereich der Resilienzforschung deuten die Ergebnisse darauf hin, dass die Architekturen der neuronalen Netzwerke in den sensorischen Kortexen selbst einen Resilienzmechanismus darstellen könnten, der zum Ergebnis eines resilienten oder anfälligen Verhaltensphänotyps beiträgt. Schließlich stellen die ersten mit der Drei-Photonen-Mikroskopie gesammelten Datensätze eine vielversprechende Möglichkeit dar, neuronale Netzwerke in tieferen Regionen wie der Schicht V von V1 aufzulösen.

III. Affidavit

I hereby certify that I have written this dissertation with the title

“A neural state of resilience? Encoding resilience as set points of cortical microcircuit activity”

independently and without outside help and that I have marked all ideas taken from other authors accordingly and have cited the relevant sources. The submitted thesis work has not been submitted to any other German or foreign university or comparable institution for the conferral of an academic degree.

I declare that I have not unsuccessfully ended another doctoral or equivalent program in the subject area of the current doctoral program.

IV. List of abbreviations

Short	Long
AMPA	α -amino-3-hydroxy-5-methyl-4-isoxazolepropionic acid
μg	Microgram
μL	Microliter
μm	Micrometer (Micron)
3D	3-dimensional
ACP	Autogenous cerebral process
AD	Alzheimer disease
AES	Adaptive excitation source
AO	Adaptive optics
AOM	Acousto-optic modulator
AP	Action potential
BS	Beamshaper
Ca^{2+}	Calcium
CaM	Calmodulin
ChR2	Channelrhodopsin-2
cm	Centimeter
CP	Critical period
cpGFP	Circularly permuted green fluorescent protein
CSD	Chronic social defeat
CV	Circular Variance
DHEA	Dehydroepiandrosterone
dLGN	Dorsal lateral geniculate nucleus
DM	Deformable mirror
ECG	Echocardiogram
EOM	Electro-optic modulator
ER	Endoplasmic reticulum
FGPA	Field-programmable gate array
FOV	Field Of View
fs	Femtosecond
GECI	Genetically Encoded Calcium Indicators
GFP	Green Fluorescent Protein
GRIN	Gradient-index
h	Hour
HD	Huntington's disease
HPA axis	Hypothalamic-pituitary-adrenocortical axis
HSF	Hybrid symptom-and-resilience factor
HVA	Higher visual cortex
Hz	Hertz
IGL	Intergeniculate nucleus
IP3	Inositol triphosphate
K^{+}	Potassium

kHz	Kilohertz
MEA	Microelectrode arrays
MHz	Megahertz
min	Minute
mm	Millimeter
MS	Multiple sclerosis
mW	Milliwatts
NA	Numerical aperture
Na ⁺	Sodium
nAChR	Nicotinic Acetylcholine Receptors
nAChR	nicotinic acetylcholine receptors
NCX	Na ⁺ /Ca ²⁺ Exchanger
NCX	Na ⁺ -/Calcium
nL	Nanoliter
nm	Nanometer
nm	Nanometer
NpHR	Halorhodopsin from Natronomonas
NPY	Neuropeptide Y
OC	Optic chiasm
OGB-1	Oregon Green Bapta-1
OPA	Optical parametric amplifier
OSI	Orientation Selectivity Index
pH	Potential of hydrogen
PMCA	Plasma membrane Calcium ATPase
PMT	Photomultiplier Tube
PV	Parvalbumin
RF	Resilience factor
RGC	Retinal ganglion cell
ROI	Region Of Interest
s	Seconds
SBR	Signal-to-background ratio
SC	Superior colliculus
SD	Standard Deviation
SEM	Standard Error of The Mean
SERCA	Sarcoendoplasmic Reticulum Ca ²⁺ -Atpase
SERCA	Sarco-/Endoplasmatic Reticulum Calcium ATPase
SI	Social interaction
SLM	Spatial light modulator
SNR	Signal-To-Noise Ratio
SP	Sensitive period
SWE	Slow wave event
SWS	Slow wave sleep
TF	Temporal focusing
Ti:Sa	Titanium-Sapphire
TRPC	Transient receptor potential channels type c
TTL	Transistor–Transistor Logic

V1	Primary Visual Cortex
VGCC	Voltage Gated Ca ²⁺ Channels
vLGN	Ventral lateral geniculate nucleus
VR	Virtual reality
WT	Wildtype

V. Table of figures

Figure 1: Schematic representation of the visual pathway.	8
Figure 2: Retinotopic organization and mapping of the visual cortex.....	9
Figure 3: Illustration of a novel approach to grasp resilience factors upon stress exposure.	18
Figure 4: Social interaction test for classifying stress resilient or susceptible phenotypes.	21
Figure 5: The action potential.....	22
Figure 6: Neuronal calcium signaling.	23
Figure 7: OGB-1 allows for an accurate representation of APs.	26
Figure 8: Representation of APs by amplitude of calcium transients of different indicators.	27
Figure 9: Principle of optogenetics.....	28
Figure 10: Principles of fluorescence excitation.....	31
Figure 11: Initial description of multiphoton absorption by Maria Goeppert-Mayer.....	32
Figure 12: Cerebral blood vessels (in vivo) imaged using a two-photon fluorescence microscope.	33
Figure 13: Illustration of a two-photon microscope and the raster-scanning principle.	34
Figure 14: Workflow of a pipeline for an event related analysis of all-optical data.....	46
Figure 15: Evaluation of photostimulation artefacts.....	53
Figure 16: A selection of calcium indicator opsin pairs and their spectral properties under a two-photon regime.	55
Figure 17: Comparison of a threshold-based algorithm with a deconvolution approach in terms of sensitivity and specificity in the detection of putatively AP-related calcium transients.	59
Figure 18: Functional two-photon calcium imaging reveals neuronal activity during slow wave events.	61
Figure 19: The relationship of single-cell activity with slow wave events persists across different animals.	62

Figure 20: Experimental design of intertwining the chronic social defeat and social interaction paradigms with awake two-photon calcium imaging.....65

Figure 21: Local network activity in V1 reflects social stress vulnerability.68

Figure 22: Non-stressed animals show similar activity levels as susceptible animals.....70

Figure 23: Resilient animals outperform susceptible and non-stressed mice in processing visual afferents.72

Figure 24: Resilient and non-stressed networks exhibit network topologies efficient for information processing.....74

Figure 25: Assessment of the long-term stability of the local network activity. .75

Figure 26: Comparison of imaging qualities in dependence of imaging depth between a two-photon and a three-photon excitation regime.....76

Figure 27: Three-photon imaging is comparable to two-photon imaging in terms of assessment of single cell activity.....78

Table of Contents

I. Abstract.....	VII
II. Zusammenfassung.....	XI
III. Affidavit.....	XV
IV. List of abbreviations.....	XVI
V. Table of figures.....	XIX
1. Introduction.....	1
1.1 Motivation.....	2
1.2 Processing of visual afferents in the primary visual cortex.....	7
1.2.1 From the retina to the visual cortex.....	7
1.2.2 Processing of visual afferents, orientation selectivity and neuronal plasticity in V1.....	10
1.3 The bound brain and the selfish network.....	11
1.4 The importance of translational models for stress assessment.....	16
1.4.1 The concept of resilience.....	16
1.4.2 Mimicking traumatic experiences in mice – Chronic Social Defeat and Social Interaction Tests.....	20
1.5 Physiological basis of calcium imaging as a surrogate marker of neuronal activity.....	22
1.6 Making the brain glow – the revolutionary concept of genetically encoded calcium indicators.....	25
1.6.1 Have you tried to turn it off and on again? Circuit manipulation by optogenetics.....	28
1.7 Microcircuit mapping by multi-photon microscopy.....	29
1.7.1 Principles of fluorescence: one-photon excitation.....	31
1.7.2 Principles of fluorescence: two-photon excitation.....	32
1.7.3 Principles of fluorescence: three-photon excitation.....	34
2. Material & Methods.....	37
2.1 Chronic Social Defeat and Social Interaction Test.....	38
2.2 Preparation.....	39
2.3 Habituation.....	39
2.4 In vivo awake two-photon imaging.....	40
2.5 In vivo anesthetized two- and three-photon imaging.....	41
2.6 Imaging data analysis.....	41
2.7 Statistical tests.....	43
3. Results.....	45
3.1 A Roadmap for processing functional calcium imaging data.....	46

3.1.1 System integration.....	47
3.1.2 Image data acquisition.....	48
3.1.3 Segmentation	49
3.1.4 Trace extraction.....	51
3.1.5 Artefact removal	52
3.1.6 Towards cross-talk-free experimental designs.....	54
3.1.7 Event-related binarization	56
3.2 Accuracy assessment: Verifying putatively Action Potential-related calcium transient representation in an analysis pipeline.....	58
3.2.1 Probing the algorithm for accuracy of sensitivity and specificity	58
3.2.2 Characterization of neuronal single cell activity during slow waves.....	60
3.3 Stress resilience is reflected in cortical microcircuit architecture.....	64
3.3.1 Combining the behavioral paradigms of chronic social defeat and social interaction with awake two-photon neuronal microcircuit recordings in the visual cortex	64
3.3.2 Susceptible mice exhibit higher spontaneous activity levels in neuronal microcircuits of the primary visual cortex	67
3.3.3 Non-stressed animals exhibit activity dynamics close to the dynamics of susceptible animals	69
3.3.4 Resilient microcircuits surpass susceptible and non-stressed microcircuits in the accuracy of the representation of visual afferents	71
3.3.5 Functional network topology of resilient networks is characterized by efficient small-world architecture	73
3.3.6 The stability of systemic resilience mechanisms - a permanent state?	75
3.4 How deep can we go? A qualitative comparison of imaging depths in two-photon and three-photon functional calcium imaging	76
3.4.1 Three-photon microscopy enables imaging of neuronal network activity in layer 5 of the cortex.....	76
3.4.2 The imaging quality using three-photon excitation is comparable to two-photon excitation	77
4. Discussion	79
4.1 The success of neurophysiological experiments using optical methods relies on an appropriate analysis pipeline.....	80
4.2 Single cell activity during SWEs can be grasped by two-photon microscopy	81
4.3 Resilient phenotypes are reflected in their network activity within the visual cortex.....	82
4.4 What comes first? The chicken or the egg?	85
4.5 Examining cortical micronetworks by three-photon microscopy – a game changer?.....	86
5. Acknowledgements	91

6. References	93
7. Appendix	113
7.1 Curriculum Vitae	114
7.2 List of publications and presentations	115
7.3 Spontaneous activity per animal	117
7.4 Connectivity maps of resilient animals	118
7.5 Connectivity maps of susceptible animals	119
7.6 Connectivity maps of non-stressed animals	120

1. Introduction

1.1 Motivation

The prevalence of posttraumatic stress disorders continues to rise in western countries (Zhang et al., 2021, Koenen et al., 2017, Global Burden of Disease Study, 2015). While a significant portion of individuals respond to traumatic events with the development of post-traumatic disorders, another segment achieves mental stability, termed resilience (Kalisch et al., 2017). Exploring the characteristics of these resilient individuals could provide insights into mechanisms that prevent the transition to disease (Kalisch et al., 2019). Resilience can be seen as an outcome influenced by resilience mechanisms, and, even though no universal concept to grasp resilience exists up to date, several mechanisms that putatively contribute to stress-resilient or -susceptible behavioral phenotypes were identified. In humans, psychological and socio-environmental factors as adaptive coping and social support can contribute to the maintenance of normal psychological function and avoid serious mental illness, but also a wide range of neurobiological markers such as changes in the neuroendocrinological system have been associated with resilience: severe stress exposure is followed a) by an activation of the hypothalamic–pituitary–adrenal axis (HPA axis) (Herman and Cullinan, 1997), a mediator of the impact of stress on the brain and behavior, b) an increase in dehydroepiandrosterone (DHEA) levels and cortisol (Rasmusson et al., 2003), which are released from the adrenal cortex, c) a decrease in Testosterone levels, impacting the perception of personal success and social status and d) differences in the levels of Neuropeptide Y (NPY) (Morgan et al., 2000, Morgan et al., 2002), where an increased level is associated with a decrease of symptoms of dissociation. Furthermore, genetic factors might play a crucial role in strengthening or weakening an individual's resilience towards stress exposure (Binder et al., 2008, Ressler et al., 2011, Polanczyk et al., 2009, Stein et al., 2009, Murrough and Charney, 2011, Domschke et al., 2010).

Traditionally, resilience has been understood and defined based on its observable features. However, these behavioral attributes could be seen as reflections of

underlying neuronal network dynamics. This thesis seeks to determine whether the phenotypic manifestation of resilience is mirrored by a distinct trajectory, a unique aspect of local network dynamics, particularly within the cortex.

To delve into the underlying neurophysiological processes triggered by stress exposure, the translation of paradigms for inducing chronic stress in mice is pivotal, forming the basis for relevant preclinical research. The chronic social defeat (CSD) paradigm, followed by measurement of social interaction (SI), was selected for this purpose. Interestingly, even among inbred mice, social interaction varies significantly among individuals. This variance hints at an individualized response of neuronal networks to stressors. Typically, animals are classified into stress-resilient and susceptible groups using a bimodal approach (Krishnan et al., 2007). This classification was adopted, using a threshold SI score of 100 to distinguish between stress-resilient and susceptible outcomes (Golden et al., 2011).

Drawing from the concept of a tightly interwoven brain (Singer, 2009, Zatzka-Haas et al., 2021), the hypothesis states that stress resilience should be evident in a cortex-wide functional pattern, extending beyond prefrontal circuits. This hypothesis also encompasses primary sensory cortices like the visual cortex, especially given the contribution of sensory discrimination to resilient outcomes. This research advances the notion of resilience from the realm of behavior to the domain of neural networks. The primary sensory networks were examined in the context of phenotypic resilience, seeking to understand whether network resilience is a broad adaptive network characteristic. To investigate this, mice were exposed to the classical CSD paradigm and the SI test (Krishnan et al., 2007), followed by two-photon calcium imaging of cortical networks in the awake, behaving animal's layer II/III of the visual cortex. Assessing both spontaneous and sensory-evoked neuronal activity with single-neuron precision offers a finely detailed perspective of the local functional arrangement

(Ellwardt et al., 2018, Arnoux et al., 2018, Rosales Jubal et al., 2021) within a resilient network.

The emergence of optogenetics, pioneered over a decade ago, has fundamentally transformed our comprehension of the roles played by distinct, genetically defined neurons within circuit function. It marked the first instance where we could ascertain the causal relationship between a specific genetic component of a network and the broader dynamics of the entire brain circuit, ultimately influencing behavior. Optogenetics has profoundly impacted every facet of neuroscience, but each field encountered its own unique challenges that had to be surmounted based on the core principle of optogenetics: the targeted illumination of a defined brain region with high-intensity light exceeding 1 mW mm^{-2} (Backhaus et al., 2023, Yizhar et al., 2011, Boyden et al., 2005, Aravanis et al., 2007). Various fields tackled distinct hurdles; for instance, single-cell electrophysiology addressed the Becquerel effect through specialized electrode design (Cardin et al., 2010, Laxpati et al., 2014), while behavioral research sought solutions for flexible, untethered light delivery (Yang et al., 2022). Many of these obstacles were overcome in the initial years following the advent of optogenetics.

However, a singular field within neuroscience remains a formidable challenge for integrating optogenetics: optical functional imaging. This domain, particularly the examination of individual neuron function within intact tissue, relies on detecting subtle fluctuations in light intensity. The development of two-photon microscopy combined with calcium indicators in the early 2000s enabled functional insights into neuronal circuits comprising hundreds of neurons in the rodent cortex (Grienberger and Konnerth, 2012, Grienberger et al., 2022, Grewe and Helmchen, 2009, Helmchen and Denk, 2005). This breakthrough significantly advanced our understanding of complex circuit dysfunctions, especially in the early stages of neurological disorders. The capacity to identify even a small fraction of dysregulated neurons within a circuit distinguishes this approach from single-cell or population-level analyses. Unsurprisingly, the integration of optogenetics

offers considerable potential in this arena, enabling the causal manipulation of individual dysregulated neurons while simultaneously monitoring circuit function. This convergence of optical imaging and optogenetics, known as "all optical physiology," became a reality in 2012 (Deisseroth, 2015, Boyden et al., 2005). However, early proof-of-concept studies quickly revealed the unique challenges posed by all optical approaches, encompassing issues related to system integration, experimental design, and, notably, analysis.

Several challenges emerged. Conventional line-scanning excitation methods proved to be inefficient. Additionally, only a limited number of opsins were found to be suitable for two-photon excitation (Chen et al., 2019), and predicting which opsins could be engineered for modified two-photon cross sections remains elusive, even though continuous efforts are taken to examine two-photon excitability of opsins (e.g. see (Sridharan et al., 2022)). Moreover, the light intensity required for two-photon optogenetics is orders of magnitude higher than that used for fluorophore excitation, leading to concerns about indicator bleaching and tissue heating (Papagiakoumou et al., 2010). Lastly, analysis hurdles included artifact removal and synchronization issues. These collective challenges have hindered the widespread adoption of all optical approaches despite their potential.

What is more, two-photon microscopy reaches its limits when neuronal networks are located deeper than 500 μm below pia mater. Due to effects based on the principle of nonlinear optics, a maximum penetration depth is inevitably reached when out of focus intensities approximate to in focus intensities (Sinefeld et al., 2022, Rodriguez and Ji, 2021, Takasaki et al., 2020, Rodriguez et al., 2021). This effect cannot be compensated by e.g. increasing the laser power, as the background intensity will increase together with the intensity in the focal plane (Svoboda and Yasuda, 2006). However, as the brain is a highly scattering organ (Al-Juboori et al., 2013) and scattering is depending on the applied wavelength (Meschede, 2015), shifting the excitation wavelength to near-

infrared can overcome the maximum penetration depth used in two-photon microscopy. By shifting the excitation wavelength regime into a range of 1300 – 1700 nm, the effect of three-photon excitation is exploited to further increase the penetration abilities and enables the experimenter to resolve neuronal networks below 500 μm (Xiao et al., 2023). However, this initially simple-sounding change to the excitation system presents the user with new challenges. First of all, commercially available light sources have a much lower repetition rate of usually 1 - 4 MHz than light sources employed in two-photon microscopy, which comprise repetition rates of up to 80 MHz. Although light sources with a higher repetition rate do exist, the complexity and maintenance requirements of these systems make them unsuitable for (neuro)biological laboratories. The reduced repetition rate makes it impossible to use resonant mirror systems, as these are too fast for the pulse frequency emitted by the laser. As a result, galvanometric mirrors must be employed, which result in a drastic reduction in the framerate. Furthermore, excitation of fluorescent dyes by a three-photon absorption process requires a photon density even higher compared to a two-photon absorption process, resulting in an increased output power of the three-photon light source. Even though these obstacles pose major challenges in the application of three-photon microscopy, the potential advantages such as increased penetration depth, reduced out of focus intensity and decreased photobleaching and toxicity effects, renders this technology a promising evolution of the already established two-photon microscopy, especially in the face of developing all optical approaches.

In this context, besides assessing the role of local neural network activity in maintaining a resilient behavioral phenotype upon social stress, another focus of this thesis is on the comprehensive workflow of an all optical experiment within circuit neuroscience. Recent advancements and the distinct requirements of all optical physiology will be discussed. In order to get a preliminary impression of the performance of a novel prototype light source that can be utilized for three-photon excitation, a microscope is

equipped with such a laser and data sets recorded with it are compared with data sets from a two-photon microscope in terms of imaging quality. The resulting findings are discussed and potential bottlenecks in the technology are identified.

1.2 Processing of visual afferents in the primary visual cortex

The visual system is one of the most important networks for perceiving our environment. We use it to navigate the world, to find food or to find our way in our society. It is a complex system that recruits different regions of the brain to represent the environment according to our needs (Hooks and Chen, 2020). Mouse models have formed the basis for research into the visual system due to the availability of genetic tools for analyzing gene functions and the architecture of neuronal circuits of precisely defined cell types (Seabrook et al., 2017, Ackman et al., 2012, Zhang et al., 2011). Furthermore, both *in vitro* studies for retinal function and *in vivo* studies that take the entire organism into account can be carried out in the mouse model. In addition, *in vivo* studies in the mouse allow the observation and manipulation of neuronal activity in larger animal cohorts in combination with behavior (Ackman et al., 2012, Glickfeld et al., 2013, Glickfeld et al., 2014, Sohya et al., 2007, Stirman et al., 2016, Zhang et al., 2011, Ko et al., 2014, Roth et al., 2016).

The following chapter shall serve as an overview of the visual stimuli processing.

1.2.1 From the retina to the visual cortex

Perception of visual afferents begins with photoreception. In the mouse two kinds of photoreceptors are present, the rods and cones. However, the rods, which operate best at low-light conditions, outnumber the cones (Fu and Yau, 2007, Seabrook et al., 2017). There are different subtypes of cones, which differ in their spectral sensitivity (Wang et al., 2011, Szatko et al., 2020). The spatial distribution of the cones in the retina is not uniform, but was, interestingly, adapted to ethnological needs in order to optimize both

contrast and color processing in the perceptive field environment (Applebury et al., 2000, Baden et al., 2013, Wernet et al., 2014). Rods on the other hand are necessary for contrast detection and negligibly contribute to render spectral information (Kelber, 2018). Photoreceptors convert light into electrical signals, which in turn are transmitted via retinal interneurons, called horizontal, bipolar and amacrine cells. They filter and shape the signals from the photoreceptors and transmit the signal to retinal ganglion cells (RGCs).

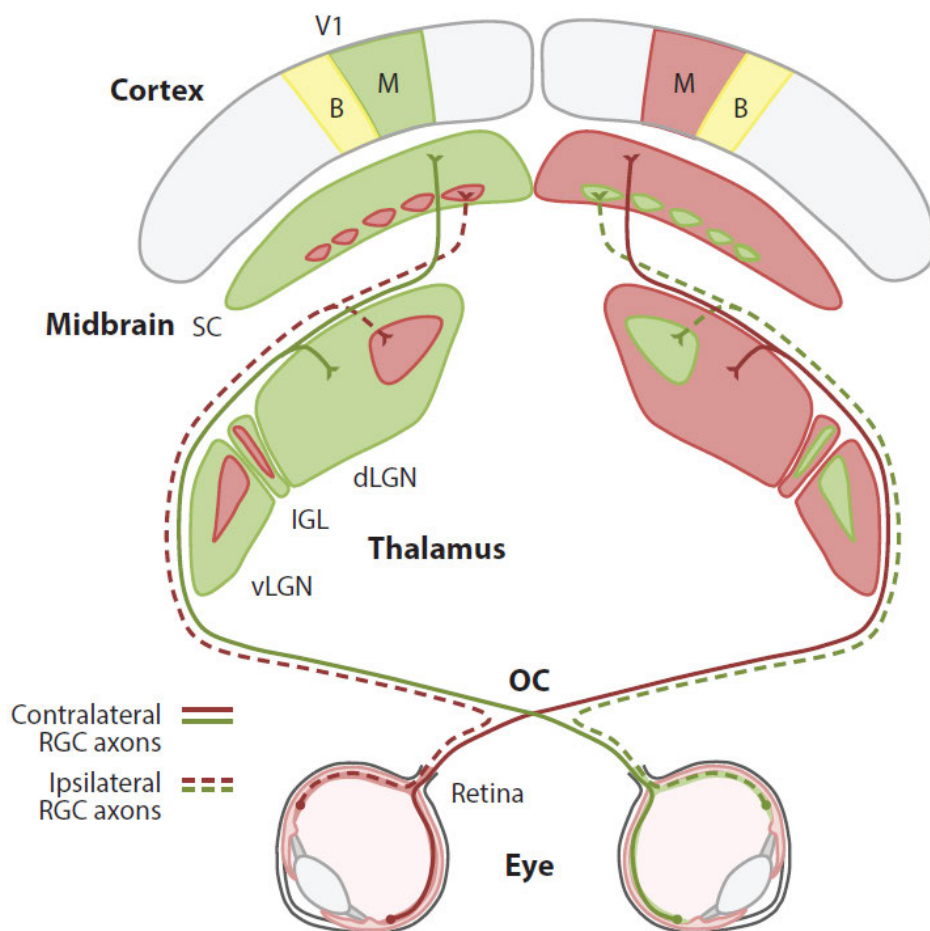


Figure 1: Schematic representation of the visual pathway. Photoreceptors located in the retina convert light into electrical signals which are transmitted via retinal interneurons to RGCs. The axons of RGCs form the optic nerve which is separated in a contralateral and an ipsilateral projection, crossing in the optic chiasm (OC). The projections are guided to the thalamus and visual cortex, where visual information is initially processed. (from (Seabrook et al., 2017))

The axons of these RGCs form the optic nerve, which is divided in two by each eye into an ipsilateral and contralateral projection. These projections cross in the optic chiasm (OC) and transmit to the corresponding areas of the brain, namely the Thalamus (consisting of the dorsal lateral geniculate nucleus (dLGN), intergeniculate nucleus (IGL) and ventral lateral geniculate nucleus (vLGN)), the Midbrain (the superior colliculus (SC)) and the visual Cortex (primary visual cortex (V1)). dLGN neurons send their axons to V1, which in the mouse consists of two zones: the monocular zone (M) receives information from dLGN exclusively from the contralateral eye, while the binocular zone (B) receives information from both eyes (Fig. 1) (Seabrook et al., 2017). We differentiate between two types of functions within the visual pathway, the “image-forming visual pathway” and the “non-image-forming visual pathway”. Whereas the non-image-forming visual pathway is needed for several key aspects necessary for vision, e.g. pupil reflexes, involuntary eye movements for image stabilization, regulation of hormone rhythms, sleep cycles and pain sensitivity (Dhande et al., 2013, Hattar et al., 2003, Nosedá and Burstein, 2011, Yonehara et al., 2009). However, the focus of this work is on the image-forming visual pathways, especially in the visual cortex V1. To grasp the environment as precise as possible, information collected by the retina needs to be represented in a topographic map, which is termed retinotopic mapping or retinotopic organization.

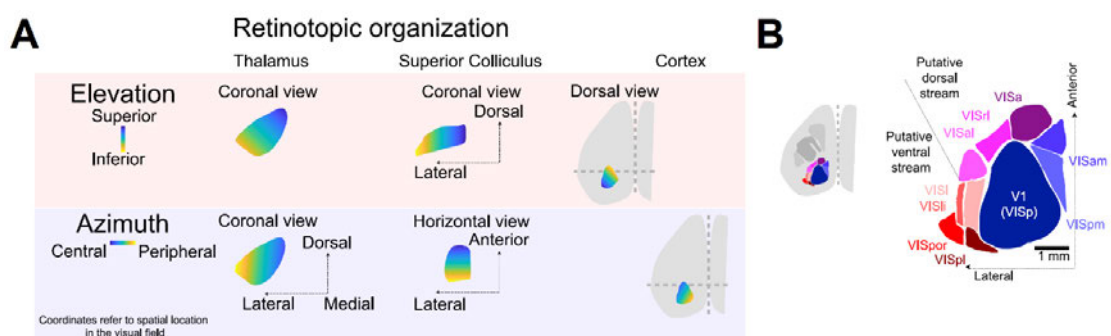


Figure 2: Retinotopic organization and mapping of the visual cortex. (A) Spatial arrangement of axonal projections in elevation and azimuth in dLGN (left), SC (center), and cortex (right) (B) The visual cortex in mice is subdivided into 9 areas adjacent to V1: V1(VISp), primary visual area; VISa, anterior area; VISal, anterolateral visual area; VISam, anteromedial visual area; VISl, lateral visual area; VISli, laterointermediate area; VISpl, posterolateral visual area; VISpm, posteromedial visual area; VISpor, postrhinal area; VISrl, rostralateral visual area. Scale bar: 1 mm. (adapted from (Hooks and Chen, 2020))

Retinotopic maps result from the spatial arrangement of axonal projections of RGCs onto a receptor target and the extent of postsynaptic neurons that collect synaptic input from the RGC axons (Fig. 2 A). Therefore, excitation patterns in the neighboring photoreceptors in the retina are also mapped onto neighboring neurons in the brain. This physiological organization for the detection of visual stimuli is present across the species (Garrett et al., 2014, Marshel et al., 2011, Wang and Burkhalter, 2007, Zeki, 1993).

The higher-order visual cortex (HVA) in mice has been parcellated more and more precisely over decades of research: Initial maps of the HVA were drawn by defining cytoarchitectural boundaries in terms of cell and fiber density and resulted in mainly two adjacent areas next to V1 (identified as Brodmann's area 17) on lateral (area 18a) and medial (areal 18b) side (Caviness, 1975). Applying intrinsic imaging lead to the identification of at least 9 distinct subareas (Fig. 2 B) surrounding V1 (Garrett et al., 2014).

1.2.2 Processing of visual afferents, orientation selectivity and neuronal plasticity in V1

One of the main tasks of the V1 is the perception of movements in the animal's environment. The so-called static and drifting grating stimulation is one way of simulating clearly defined movement patterns in *in vivo* studies. These stimulation patterns, consisting of alternating black and white bars arranged at different angles, which are either static or moving, i.e. drifting, in turn stimulate neurons that are specifically used to detect these high-contrast patterns. Neurons responding to these signals are termed direction- or orientation-selective. Orientation-selective neurons in V1 in mice, unlike in cats and monkeys, do not follow a clear pattern to one another in regards to the retinal surface, but rather show a so-called salt and pepper organization (Seabrook et al., 2017). This thesis will only focus on network activity in V1, even though recent studies showed that orientation selectivity is already processed in the dLGN shell

(Briggman et al., 2011, Huberman et al., 2009, Wei et al., 2011), the SC (Ahmadlou and Heimel, 2015, Feinberg and Meister, 2015) and evidence suggests that even some RGCs in mice might be orientation selective (Baden et al., 2016, Nath and Schwartz, 2016).

The development of the visual system begins in utero and undergoes an initial reorganization in early life, where a spontaneous activity- and experience-dependent restructuring takes place (Rocheffort et al., 2009). The uniqueness of the visual system is demonstrated by its resilience to disturbances during and after this early life development phase (Hooks and Chen, 2020). Network changes during the developmental phase have been the subject of intensive research and namely take place during sensitive periods (SPs) and critical periods (CPs). SPs describe windows during development where neuronal circuits are altered based on experience-dependent modifications. It is worth noting, that these changes can also occur outside of SPs in later life stages, albeit to a lesser extent. CPs on the other hand are subsets of SPs and are characterized by a sharp on and offset in which experience-induced changes can model the neuronal network. Furthermore, changes during CPs are considered crucial for subsequent normal connectivity and function (Voss, 2013), even though substantial plasticity during adulthood beyond CP can be induced by using stimulus paradigms that do not resemble experiences gained during CP (Espinosa and Stryker, 2012, Fong et al., 2016, Hensch and Quinlan, 2018, Sato and Stryker, 2010). In their joint review, Hooks and Chen summarize, that the visual circuit is indelibly altered by experience (Hooks and Chen, 2020).

1.3 The bound brain and the selfish network

The presence of cognitive and executive functions in the brain and higher mental abilities that we generally regard as consciousness, at least in humans, by consensus of the prevailing view, arise from a complex architecture of neural interactions. Efforts

to explain the behavioral patterns ultimately resulting from sequences of neuronal activity patterns have been conducted particularly in low-complexity species, such as *C. elegans* (Gottschalk, 2020, de Bono and Maricq, 2005, Atanas et al., 2023) and *Drosophila* (Fisher et al., 2015, Ketkar et al., 2022), which comprise a relatively well-defined and simple brain structure. Even brains in more highly evolved species, despite their increased complexity and refined behavioral capabilities, are still subject to the same principles of functionality. However, it must be taken into account that not only genetic inheritance determines the underlying pattern of neuronal activity, and thus observable behavior, but also epigenetic influences due to the presence of a socio-cultural environment. These external, behavioral influences have recently emerged as a focus of research in translational studies.

For example, different cortical areas, which perform well-defined neurophysiological functions, are based on similar processing algorithms. This is a fundamental necessity to guarantee a generalized and abstracted encoding of the environment. The wiring of the individual cortical areas does not follow a serial hierarchy, but shows to a considerable extent a parallelized structure based on reciprocity and decentralization. This results in neurons in sensory cortices being able to communicate directly with executive areas. A mesh of connections ultimately creates a highly structured entity that has properties of a small world network where representations of the environment are reflected by complex spatio-temporal patterns of neuronal activity, rather than a single locus or the historical concept of the presence of a homunculus.

The bottom-up (Britten et al., 1996) and top-down (Nienborg and Cumming, 2009) hypotheses have been the common explanations of how the brain processes incoming sensory stimuli and, in consequence, how actions are executed. In these classical hypotheses of well-defined allocations of tasks, carried out by specific brain regions (Strotzer, 2009), sensory cortical brain regions were attributed solely a sensory-processing function. In the last few years, the notion of sensory cortical areas being

associated exclusively with processing input related to its given modality, e.g. the visual cortex, attributed to visual perception only, has been challenged. Although the main function of the visual cortex unquestionably is the processing of visual input, there is evidence that an intensive exchange of different cortico-cortical and sub-cortical regions takes place before and during responses upon external stimulation, and that cortical regions also contribute to decision making, albeit to a lesser extent (Zatka-Haas et al., 2021).

In order to fully comprehend a visual object, physically perceptible properties such as shape, color, odor, surface texture, and other types of information are processed in the brain. The actual perceptual processing in different sensory cortices requires an integration of the multitude of information to fully grasp the entity of an object. There is evidence, that this is achieved by a much more complex interaction between sensory cortical regions than suggested by traditional theories, such as the conceptualization of autogenous cerebral processes (ACPs) as an explanation for the theory of “active sensing” highlighting the interplay of various motoric and sensory cortical areas (Maldonado et al., 2023).

What is more, many neurological diseases such as Multiple Sclerosis, Huntington’s disease or Alzheimer can already be diagnosed before phenotypical changes that are associated with progression of the disease become evident (Dominguez-Fernandez et al., 2023, Doroszkiewicz et al., 2022, Mukherjee et al., 2020, Sung et al., 2023, Zarhin et al., 2022, Safai et al., 2021, Helson et al., 2023, Ying et al., 2022, McTeague et al., 2020). For example, it has been shown that early-stage neurological diseases affect neuronal activity on the network level before the onset of disease-defined phenotypic changes and that an early shift of neural network activity might represent the actual onset of the disease (Stroh et al., 2024, Ellwardt et al., 2018, Arnoux et al., 2018). These changes can be manifested as neuronal hyperactivity in mouse models of Alzheimer and are only associated with subtle behavioral dysregulations (Rosales Jubal et al.,

2021, Zott et al., 2018) which can even occur in brain regions that were thought to not be affected by symptoms during late disease progression (Rosenberg et al., 2015). The aim of the shift of network activity is not to preserve or achieve a long-term stable architecture, but instead to maintain the momentary status quo of functionality. As this procedure can be interpreted as short-sighted and without regard to influences on the functionality of other brain regions, these networks are referred to as selfish networks. Indeed, a local network dysregulation governed by a selfish network can bidirectionally impact other selfish networks who share the same fate and therefore initiate an avalanche, forcing the organism to maintain functionality. When certain tipping points are reached, a rapid decline in behavioral functions can be observed. It is proposed that the principle of selfish networks renders boundaries of a maladaptive network in a spatio-temporally dynamic manner and that they can occur in all neuronal network spatial scales due to their tight interconnections, reinforcing the theory of a functionally bound brain.

Developed over millions of years of evolution, homeostatic processes within the organism are initiated upon network dysregulations and serve the purpose to maintain the neuronal set point, or the functionality of a network, and can vary from subject to subject (Styr et al., 2019, Wu et al., 2022, Wu et al., 2020, Torrado Pacheco et al., 2021). Initially, these compensator mechanisms may suffice to maintain functionality which will be preserved for a certain amount of time and deficits remain undetected at an organismic level, but the networks are inevitably driven away from their evolutionary dedicated set point. Only when severe signs of a disease are observable, a tipping point of compensation efforts is reached and a new metastable set point is established.

As mentioned before, early network dysregulations can occur in areas that are not associated to the typically affected brain regions of a disease. Therefore, primary sensory cortices may offer a promising opportunity to investigate these early impairments in local functional architecture. As postulated by the principle of a bound

brain (Zatka-Haas et al., 2021, Singer, 2009, Singer, 2013), disruptions in neural network architecture of distant regions also impair multiple local networks within the whole brain. Since the visual cortex is connected to many other areas and has input and feedback to, for example, the motor system, but also connections to areas attributed to emotional regulation, it is an ideal candidate to study network dysregulation. Indeed, in the presymptomatic phase of a mouse model of HD, with the disease onset marked by the occurrence of clinically significant motor symptoms, a local shift toward hyperactivity could be found within the visual cortex: an increase of synchronicity could be observed which is considered to be an active process in early disease progression (Arnoux et al., 2018). Furthermore, in a mouse model of AD, whilst amyloid plaque formation was still absent, a new neuronal set point within the visual cortex could be identified (Rosales Jubal et al., 2021). The dynamical systems theory provides tools suitable to describe and characterize properties of network states such as stability and trajectory (Breakspear, 2017). Describing a neural network employing systems theory, the network depicts a multidimensional system, mathematically translated into coupled differential equations with multiple parameters with corresponding multidimensional parameter spaces, which can result in trajectory dynamics composing of attractors, which are stable and self-stabilizing solutions, repellers, representing unstable solutions and saddles, which are semistable solutions (Deco and Jirsa, 2012). The challenge therefore lies in the multitude of potential states: Each neuron can be described by a binary functional state of inactive (0) and active (1). Taking into account that each neuron may have up to 10,000 synaptic connections, the number of potential states is hard to grasp.

However, when omitting the topological view of a network and instead apply a network-state-centered approach, where only a low number of network states exist over time, a dimensionality reduced approach with a limited set of discrete states can be employed (Finkelstein et al., 2021). By moving from neuronal to parameter space, most of the

variance of the system can be described in time. The parameters itself contain a subset of framework conditions, such as the molecular principle of a disease, network compensations or the functional outcome. By modelling the interaction between all parameters, a parameter landscape can be generated, containing attractors, repellers or saddles, whereas time represents the parameter describing the trajectory of the system that is moving through the parameter landscape (Freyer et al., 2012). The impact on the systems trajectory and a given outcome can vary: If certain boundaries are not crossed, the system will trace back to the given state. In case the impacts exceed these boundaries, the system can be driven into a different attractor state associated with change in functionality. These changes can be maladaptive in character, e.g. if strong risk factors hit the system in a vulnerable state, or, in case of an intervention, render an attractor state considered beneficial (Kaiser et al., 2022, Stiso et al., 2019).

Considering the bound brain theory that postulates a highly dynamic connectivity of brain areas in combination with the novel concept of selfish networks explaining the transition of a neuronal network upon exposure to adverse conditions, together with the high plasticity of the visual cortex even in adulthood that is formed on the basis of experience, renders the visual cortex a promising region to describe influences of chronic social stress on cortical micronetworks.

1.4 The importance of translational models for stress assessment

1.4.1 The concept of resilience

The concept of stress resilience describes an individual's capability to maintain or recover mental health during and after adversity (Kalisch et al., 2017). In 2019, Kalisch and colleagues proposed, to omit the generally prevailing view that resilience is a uniform personality construct that protects the individual from the progression into

mental illness and replaced it by a view that describes resilience as complex dynamic processes. These processes include adaptation to stressors by activation of independent protective factors, covered by biological, psychological and social levels and take stable predispositions like genotype or personality traits into account as well as alterable characteristics, abilities, capacities or external factors. In this fine-grained explanatory approach, psychiatric disorders are described by dynamic network nodes of interacting symptoms which might drive an individual into a stable and maladaptive state of disease, while on the other hand, resilience factors comprise of additional, independent network nodes which are able to weaken symptom-symptom interconnections.

In these symptom networks, each node represents a symptom (Fig. 3 A, symptom 1-4). These symptoms can be strongly statistically associated and are able to influence each other determined by the strength of interconnection. The network in Fig. 3 A a) represents a healthy network in which symptom interaction is low. The network in Fig. 3 A b) represents a symptom network with several symptoms showing high, correlated activation.

Since each node can undergo changes in its severeness of expressed symptoms, the network underlies dynamic changes. Measuring symptoms at different timepoints t allows for estimating cross-sectional contemporaneous which occur at the timepoint t (Fig. 3 B a)) and longitudinal symptom connections which undergo a time-delayed change from t to $t+1$ (Fig. 3 B b)). Temporal connections are directional, as indicated by the arrowheads and are shown here in a reciprocal manner. However, it has to be noted, that temporal symptom-symptom connections certainly can be unidirectional and the strength of the connection can differ. Furthermore, the model assumes that the time points of the evaluation of symptom severity and interconnection strength take place at regular intervals, but is in principle not restricted to it and could even consist of a continuous assessment of time processes.

An explanatory progression of a dynamic system into a maladaptive state is shown in Fig. 3 C: The considered network is free of high active nodes at the timepoint t , the system is in a stable state of “mental health” (Fig. 3 C “ t ”). At timepoint $t+1$, an external stressor (E) is introduced which leads to an increase of severeness of symptom $S1$ (Fig 3 C “ $t+1$ ”). Due to the postulated node interconnection, symptoms $S2$ and $S3$ are now also driven into a strong co-activation, exhibiting severe activity themselves (Fig 3 C “ $t+2$ ”). The system state thus achieved can be characterized as “reaching mental disorder” and, in some cases, can be stable or self-sustaining in its persistence (Fig 3 C “ $t+3$ ”) even in the absence of the stressor (E).

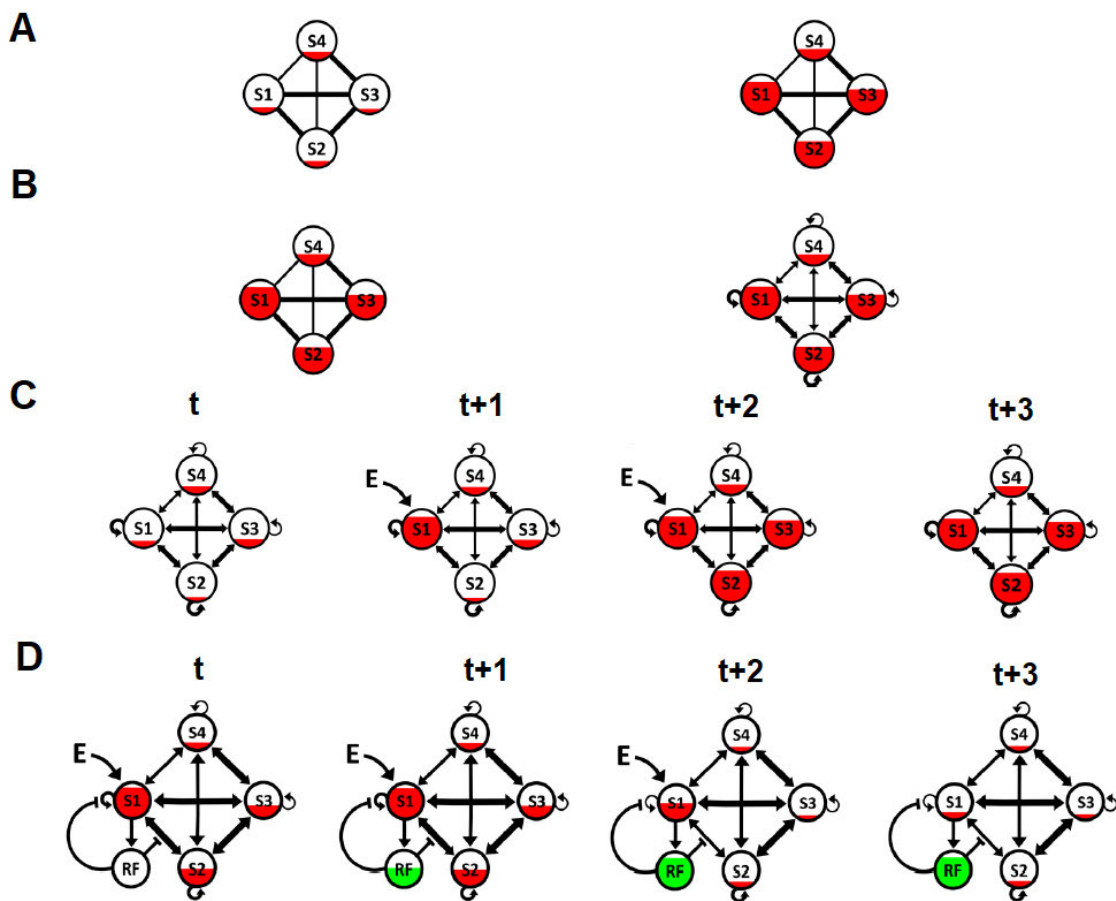


Figure 3: Illustration of a novel approach to grasp resilience factors upon stress exposure. $S1-S4$ represent nodes of psychiatric symptoms with the filling grade of the circle as a description of distinctiveness. Line thickness indicates the interaction between separated symptoms and their ability to increase each other. E represents the presence of a stressor and RF poses a resilience factor. (adapted from (Kalisch et al., 2019))

The question arises, how the variation of outcomes regarding mental health in different subjects can be explained while being exposed to the same stressors. Certainly, not only the strength of symptom-symptom interconnections plays a crucial role how an individual maintains mental health in the face of adversity, but also the presence of resilience factors poses a fundamental coping mechanism. These resilience factors are introduced as dynamic nodes themselves into the “hybrid symptom-and-resilience factor” (HSF) termed model (Fig 3 D). Resilience factors are activated in stressful situations and can be trained over time: The time-variant degree of efficiency/effectiveness of a resilience factor (RF) increases over time (Fig 3 D “t” to “t+1”), indicated by the green filling, and becomes stronger while effectively reducing symptom auto-connections (Fig 3 D “t+2”) or symptom-symptom interconnections (Fig 3 D “t+3”) (Kalisch et al., 2019).

The here presented refined HSF model, depicting maintenance of mental health as interplay of several symptom and resilience factor nodes, allows to grasp the complex network in a mathematical model. These models can be based on parametric stochastic Lotka-Volterra systems (van Nes and Scheffer, 2004), bifurcation theory (Scheffer et al., 2012) and auto-regressive models (Scheffer et al., 2009), as well as non-parametric methods, e.g. regularized partial correlation analysis for continuous variables (Friedman et al., 2008) or Ising models for binary data (van Borkulo et al., 2014). However, it has to be noted, that mathematical and computational limits occur due to the large number of resilience factors already identified (Kalisch et al., 2017, Bonanno et al., 2015) and the continuous increase of datasets in temporal dimensions and number of subjects. Furthermore, it still remains elusive, how to define the nodes and which ones need to be included in a given model, as an incorrect implementation into a mathematical model will inevitably lead to inconclusive results.

1.4.2 Mimicking traumatic experiences in mice – Chronic Social Defeat and Social Interaction Tests

The development of animal models to study depression poses a major challenge in psychiatric research. A vast variety of paradigms were developed to mimic forms of chronic stress to induce behavioral adaptations relevant to depression, e.g. chronic unpredictable stress, restraint stress and foot-shock stress, which are often followed by behavioral measures related to anhedonia or despair (Krishnan and Nestler, 2010, Krishnan and Nestler, 2008, Nestler and Hyman, 2010). However, there is a limited availability of animal models that address the dynamic ranges of reactions an individual can show in response to stressors and, what is more, can be employed to investigate the resiliency towards the exposure to stressors (Yehuda et al., 2006). Social stressors are known to drive affective behavioral responses in a variety of mammalian species. A repeated social stress exposure of rodents can for example lead to behavior linked to anhedonia, anxiety or social-avoidance (Kudryavtseva et al., 1991, Rygula et al., 2006a, Rygula et al., 2006b, Rygula et al., 2005, Berton et al., 2006).

In particular, Chronic social defeat (CSD)-induced social avoidance is considered to model a feature of stress-related mental dysfunction, while its absence can be used as a proxy of resilience in rodents (Ayash et al., 2020). In a chronic social defeat paradigm, the experimental mouse is forced to intrude the territory of a larger mouse of a more aggressive genetic strain, which ultimately leads to attacking behavior towards the intruder. In order to avoid a context-related aversion to a single attacker or a habituation of the aggressor towards intruders, this is carried out between 10 (Leschik et al., 2022, Wendelmuth et al., 2020, Krishnan et al., 2007) and 15 (Grandjean et al., 2016, Kumar et al., 2014, Azzinnari et al., 2014) days, depending on the paradigm, with changing residents in each trial (Golden et al., 2011). During an encounter phase the aggressor is allowed to attack the intruder, which is limited to an initial attack of a few seconds (Azzinnari et al., 2014, Wendelmuth et al., 2020, van der Kooij et al., 2018) or can last

up to minutes (Krishnan et al., 2007, Leschik et al., 2022). This phase is followed by a sensory phase in which both mice are separated from each other, e.g. by a metal grid, but sensory perception is still possible. To assess the level of social-avoidance, which is supposed to be related to a rather resilient or susceptible behavioral outcome of the experimental mouse, a social interaction test (SI-test) is carried out either on the following day of the final defeat trial, or up to 10 days later (Krishnan et al., 2007, van der Kooij et al., 2018, Wendelmuth et al., 2020). Here, the experimental animal is placed in an unfamiliar cage containing a separate container, which is surrounded by the so-called interaction zone. This container allows for sensory but not physical interaction and is either empty or contains a mouse of the aggressive substrain. By comparing the time a mouse spends in an interaction zone with an aggressive mouse within the container to the time it is empty, a social interaction value (SI-value) is calculated (Fig. 4).

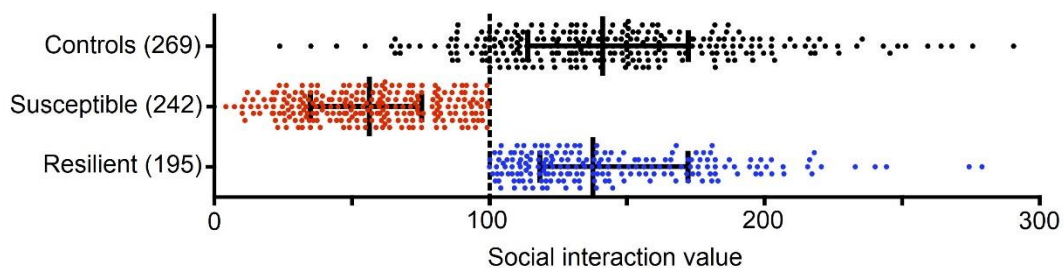


Figure 4: Social interaction test for classifying stress resilient or susceptible phenotypes. Outcome and classification of stress resilient and susceptible mice by carrying out a SI-test upon chronic social defeat (adapted from (Krishnan et al., 2007)).

It has been shown that when analyzing a large number of chronically defeated mice, there is a wide spread of responses, with 40-50% of the defeated mice showing similar interaction values to the non-defeated control subjects. Since the vast majority of control mice spend more time interacting with a social target than with an empty target enclosure, an interaction ratio of 100 (equal time in the presence and absence of the

aggressive substrain) was set as a cut-off value. Mice with values <100 are labeled "susceptible" and those with values ≥100 are labeled "resilient" (Krishnan et al., 2007).

1.5 Physiological basis of calcium imaging as a surrogate marker of neuronal activity

Neurons are surrounded by a cell membrane, a phospholipid bilayer, in which a variety of channels are embedded. These channels allow for the active and passive transport of ions into or out of the cell. While neurons are inactive, a potential difference of -70 mV results between the cytosol and the extracellular medium, termed resting potential (Fig. 5 B-I). When a neuron receives a stimulus, voltage gated Na⁺ channels begin to open and sodium can enter the cell. Here, a threshold potential of -50 mV needs to be reached in order to open additional Na⁺ channels. Should the threshold potential not be reached, the excitation is reversed.

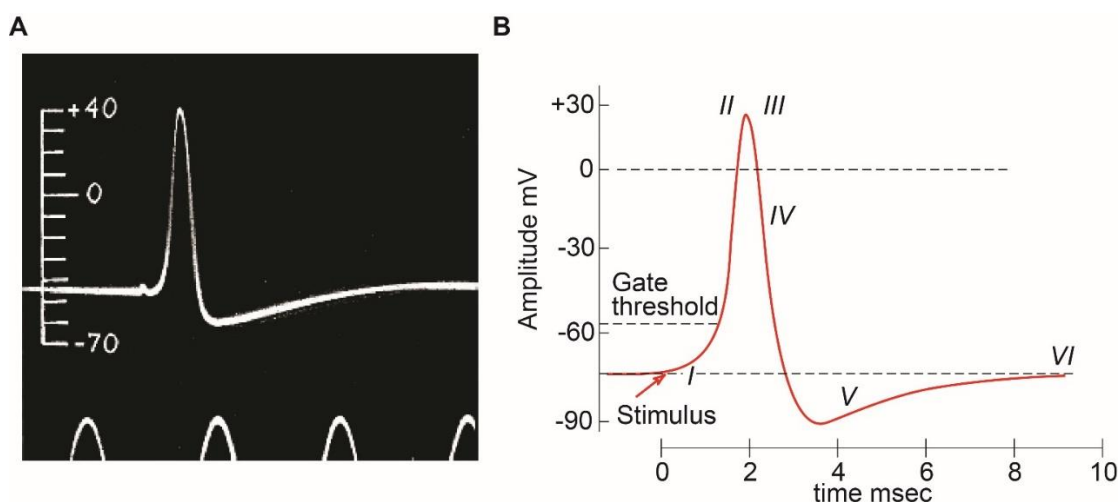


Figure 5: The action potential. (A) Historical measurement of an action potential by Huxley and Hodgkin. Recorded in the axon of a squid. (Hodgkin and Huxley, 1939). (B) Exemplary signal waveform of the membrane potential during an action potential. The neuron receives a stimulus (I) and Na⁺ channels begin to open. When a threshold of -50 mV is reached, more Na⁺ channels open and during the depolarization phase the membrane potential increases up to +30 mV. At +30 mV, the Na⁺ channels close (II) and K⁺ channels open (III), allowing potassium ions to migrate to the extra cellular, initializing the repolarization phase (IV). The slow kinetics of K⁺ channels lead to a membrane potential below resting potential, termed hyperpolarization (V). During hyperpolarization, no action potential can be carried out. By activation of Na⁺/K⁺ pumps, which transport sodium ions out and potassium ions inside the cell until the resting potential (VI) is reached again (adapted from (Sanei and Chambers, 2007)).

If the membrane potential surpasses the -50 mV, a rapid change of potential is initiated, which is referred to as action potential. It has to be mentioned that the generation of an

action potential follows an all-or-nothing principle: either the incoming stimulus is strong enough to evoke an action potential – or not. Upon surpassing the threshold potential, the depolarization phase is initiated and more sodium enters the cell until the membrane potential reaches +30 mV. At the peak of the action potential, most of the voltage gated Na^+ channels close again (Fig. 5 B-II), preventing further sodium ions to enter the cell. At commencement of the repolarization phase, K^+ channels open (Fig. 5 B-III), which in turn enable positive charged potassium ions to migrate from the cytosol to the extracellular medium, causing the membrane potential to recede towards the resting potential (Fig. 5 B-IV).

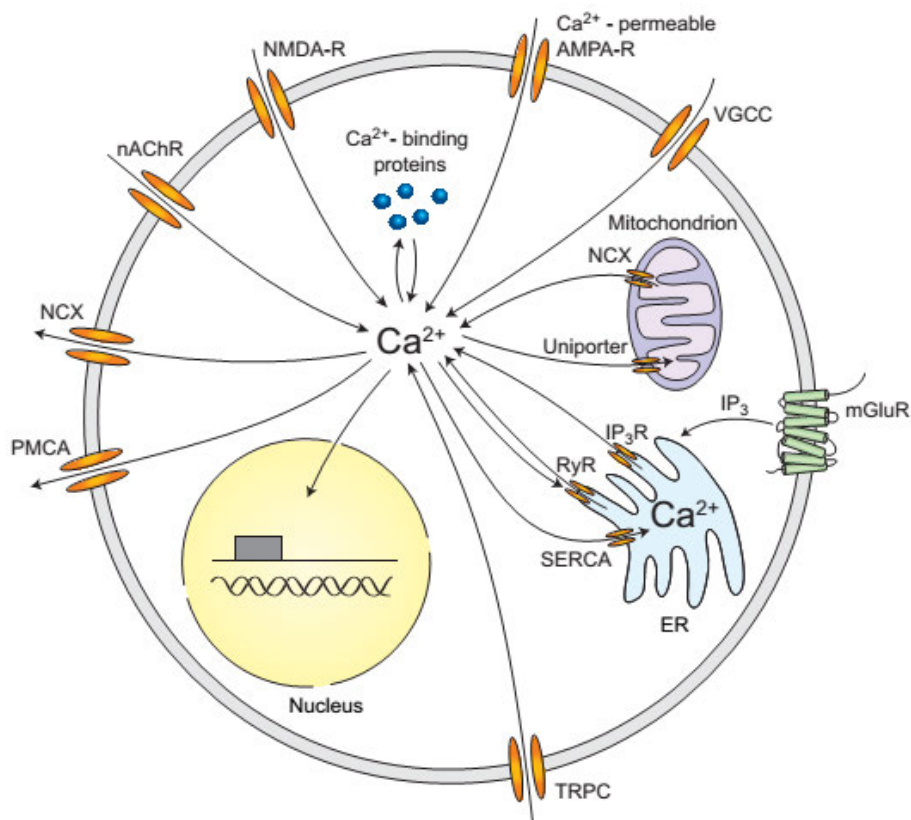


Figure 6: Neuronal calcium signaling. Calcium influx into the cell is mediated by NCX, NMDA, calcium permeable AMPA receptors, VGCC and TRPC channels. In addition, internal calcium storages in the ER are controlled by IP₃R and RyR receptors, but also storages in Mitochondrion release calcium. Calcium efflux into the extracellular medium is mediated by PMCA and NCX. (from (Grienberger and Konnerth, 2012))

As a consequence of the potassium efflux and the longer closing kinetics of K^+ channels compared to Na^+ channels, the membrane potential reaches for a short time potentials

below the resting potential, called refractory period or hyperpolarization (Fig. 5 B-V). During hyperpolarization, Na^+/K^+ pumps are activated and restore the resting potential by pumping sodium ions out of the cell and potassium ions into the cell (Fig. 5 B-VI). While the neuron is hyperpolarized it is not excitable (Kandel, 2013, Schmidt and Schaible, 2006).

Calcium is an essential intracellular messenger. At rest, most neurons have an intracellular Calcium concentration of approximately 50-100 nM, which can increase 10- to 100-fold when an action potential is occurring, and can therefore be utilized as a surrogate marker of action potential occurrence, at least in the neuronal soma (Berridge et al., 2003). Some of the key mechanisms are illustrated in Fig. 6: at each time point, cytosolic Calcium concentration is defined by the ratio of Calcium in- and efflux, as well as by the release and uptake of Calcium by internal storage units. In addition, Calcium-binding proteins such as parvalbumin, calbindin-D28k, or calretinin act as Calcium buffers and thus regulate the temporal dynamics of free Calcium in a neuron (Schwaller, 2010). It is worth mentioning that only free Calcium ions are relevant for cellular signal transduction. Many mechanisms lead to the influx of Calcium from the extracellular milieu into the cell, such as the opening of voltage-gated Calcium channels, ionotropic glutamate receptors, nicotinic acetylcholine receptors (nAChR), and TRP channels type C (TRPC, transient receptor potential channels type c) (Fucile, 2004, Higley and Sabatini, 2008, Ramsey et al., 2006). Efflux of Calcium from the cytosol is regulated by plasma membrane Calcium ATPase (PMCA) and by $\text{Na}^+/\text{Ca}^{2+}$ exchangers (NCX) (Berridge et al., 2003). Release from internal storage units, mainly from the endoplasmic reticulum (ER), is controlled by IP₃ receptors (IP₃: inositol triphosphate) and ryanodine receptor (Berridge, 1998). In this process, inositol triphosphate can be formed in neurons themselves, for example, through the activation of metabotropic glutamate receptors (Niswender and Conn, 2010). The high Calcium concentration within the ER is provided by the Sarco-/Endoplasmic Reticulum Calcium ATPase

(SERCA), which transport Calcium ions from the cytosol to the lumen of the ER. In addition to the ER, mitochondria are important for neuronal Calcium homeostasis because they act as buffers during the cytosolic Calcium rise by taking up Calcium through a uniporter and then slowly releasing it back into the cytosol through Na⁺/Calcium exchangers (Duchen, 1999).

1.6 Making the brain glow – the revolutionary concept of genetically encoded calcium indicators

Functional calcium imaging utilizes the action-potential related calcium influx into a cell as a correlate of neuronal activity (Boiroux et al., 2014, Chen et al., 2012, Adelsberger et al., 2014). For this, an indicator is injected into the brain region of interest. One of the indicators used is Oregon Green Bapta-1 (OGB-1), which is based on the molecule 1,2-bis-(2-amiophenoxy)ethane-N,N,N,N-tetraacetate (BAPTA). In addition to the Calcium-binding molecules, the dye consists of fluorophores, whose structure is responsible for the spectral property. OGB-1 is excited by light with a wavelength of 488 nm. The emission spectrum reaches its maximum at 520 nm (Paredes et al., 2008). The intensity of the emitted fluorescence of this dye increases with increasing Calcium binding. It has been shown that simultaneous recording of spontaneous Calcium transients using OGB-1 and current-clamp techniques (Fig. 7 A), in which a single cell attached to electrodes allows the membrane potential to be recorded and thus provides direct information as to whether a cell is performing an action potential (Fig. 7 B), leads to a linear increase in the intensity of fluorescent light (Rochefort et al., 2009). This indicates that the change in fluorescence is correlated directly with the number of action potentials carried out (Fig. 7 C).

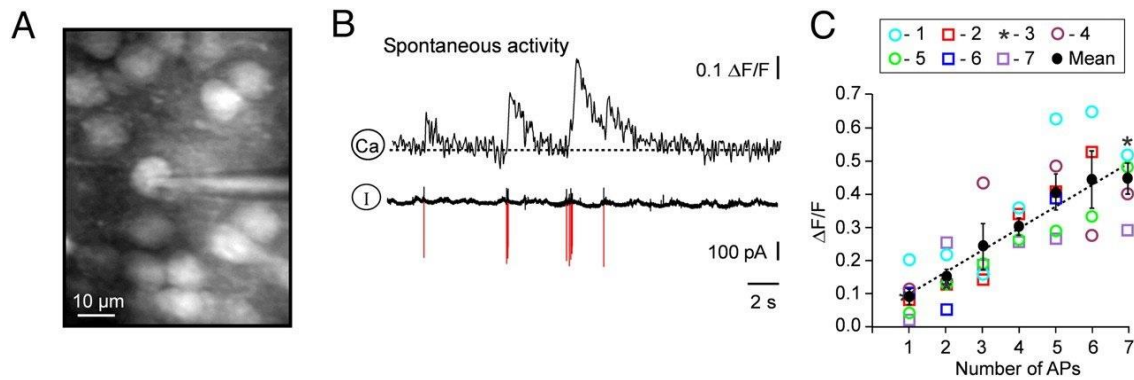
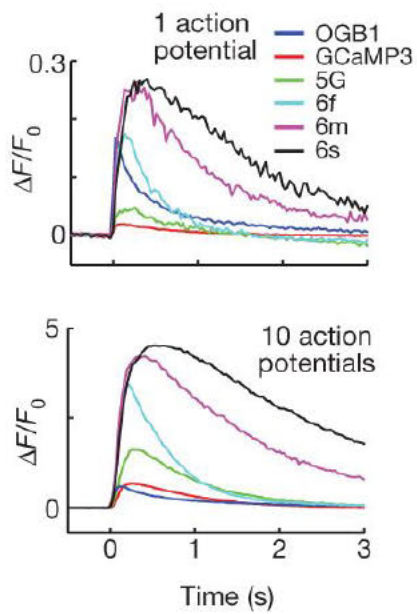


Figure 7: OGB-1 allows for an accurate representation of APs. (A) Simultaneous recordings of Calcium transients and underlying action potential firing of a neuron in layer 2/3 of the visual cortex. (B) Correlating fluorescence intensity of the indicator and single cell activity, measured using the current-clamp technique. (C) a linear relationship exists between AP's of a cell and the increase of changes fluorescence. (from (Rocheffort et al., 2009))

However, only the invention of genetically encoded calcium indicators (GECIs) truly revolutionized the field of *in vivo* fluorescence microscopy: here, viral transduction is used to express the GECI in a cell over a prolonged period of time. Currently, the most commonly employed GECIs are from the GCaMP-family. The first version of GCaMP was introduced by Nakai et al. in 2001 (Nakai et al., 2001) and has been further developed since then. To date, the GCaMP family has been developed up to version GCaMP8, even though its predecessor, GCaMP6, is still widely used today. In principle, all members of the GCaMP-family consist of a circularly permuted green fluorescent protein (cpGFP), Calcium binding calmodulin (CaM), and an M13 peptide that interacts with CaM (Chen et al., 2013a). A calcium-dependent conformational change in the CaM-M13 complex leads to a change in fluorescence properties with increasing Calcium concentration. Although GCaMP does not have the sensitivity and temporal resolution in detecting single action potential as (Fig. 8), for example, OGB-1, it offers the advantage that measurements can be made weeks after the vector is injected (Huber et al., 2012, Tian et al., 2009, Peters et al., 2014, Margolis et al., 2012). Furthermore, specific cell types and populations can be investigated by using

promoters. It has to be mentioned that there are different subtypes of GCaMP: GCaMPs



(the “s” stands for “slow”), exhibits a high SNR but slow Off kinetics, GCaMPm (“intermediate”) exhibits medium and GCaMPf (“fast”) fast kinetics (Chen et al., 2013a). The excitation spectrum of GCaMP6f has its maximum at 497 nm (Chen et al., 2013a) under a one-photon excitation regime.

Figure 8: Representation of APs by amplitude of calcium transients of different indicators. (Upper) one AP is carried out versus (lower) 10 APs. (from (Chen et al., 2013a)).

1.6.1 Have you tried to turn it off and on again? Circuit manipulation by optogenetics

The development of optogenetics enables the investigation of neuronal microcircuits through the possibility of cell-specific manipulation upon light exposure of individual neurons with millisecond temporal precision and minimal invasiveness (Boyden et al., 2005). Moreover, this method can be combined with other well-established methods for the detection of neuronal activity, for example single-cell electrophysiology, microelectrode arrays (MEA) (Yang et al., 2017), functional magnetic resonance

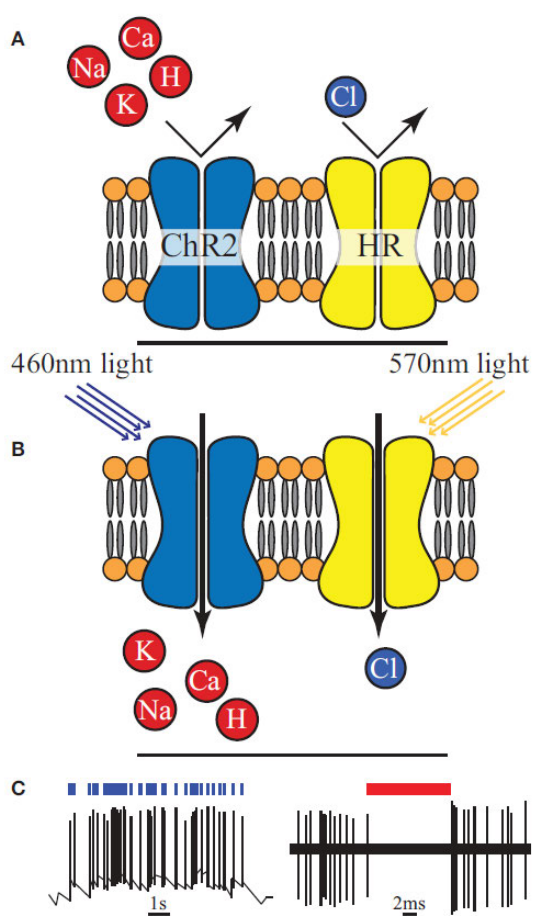


Figure 9: Principle of optogenetics. (A) An excitatory channel (left) and inhibitory ion-pump (right) prior excitation by light in their inactive state. (B) Upon excitation with 460 nm light, ChR2 undergoes a conformational change and ions can stream into the cell, whereas HR pumps chloride ions into the cell when excited with a wavelength of 570 nm. (C) This results in a depolarization (left) of the cell and generates an action potential, while activation of HR leads to an inhibition of the cell (right). (from Luan et al., 2014))

imaging (Schmid et al., 2017, Schmid et al., 2016, Schwalm et al., 2018), or optical methods such as two-photon calcium imaging. Within the opsins, a distinction is made between excitatory and inhibitory opsins. A commonly used representative of the excitatory opsins is channelrhodopsin-2 (ChR2), a cation-selective ion channel that is activated by light of a wavelength of 460 nm (Nagel et al., 2003, Nagel et al., 2002). In the absence of light, the channel remains closed and does not allow any influx of ions (Fig. 9 A, left). When the channel is excited with light at a wavelength of 460 nm, it opens due to an underlying conformational change upon photon absorption and allows the passive flow of different cations into the cell according to

the electrochemical gradient (Fig. 9 B, left), leading to a light mediated depolarization of the cell (Fig. 9 C, left).

An example of an inhibitory opsin is NpHR, a member of the Halorhodopsin family, which can be described as a hyperpolarizing light-driven chloride pump. Similar to excitatory opsins, the chloride pump stays inactive while not exposed to light (Fig. 9 A, right). Upon light exposure of a wavelength of 570 nm, chloride ions are pumped into the cell via the membrane pump (Fig. 9 B, right), ultimately suppressing neuronal activity by hyperpolarization (Fig. 9 C, right) (Schobert B, 1982, Han and Boyden, 2007, Zhang et al., 2007). Another inhibitory opsin, ArchT (Chow et al., 2010, Han et al., 2011), enables neuronal inhibition by pumping protons out of the cell after absorption of excitation photons, thereby changing the pH between intra/extra cellular space. What is more, all opsins can be fused with a promoter, allowing for well targeted, cell-specific perturbation of neuronal microcircuits.

1.7 Microcircuit mapping by multi-photon microscopy

Circuit neuroimaging historically originated in invertebrate species, and, alongside with the technique maturation and development, has been introduced in application of various model organisms, such as Zebrafish, allowing e.g. for the whole body imaging of transparent zebrafish larvae (Kim et al., 2017). In recent years, optical imaging of local circuits has been predominantly applied in mouse models. This is on the one hand due to the fact of the availability of mouse models of human disorders, and also due to the rather preserved cortical cytoarchitecture in comparison to humans. The limitation of penetration depth and of course the invasiveness of the method currently seems not to allow the implantation in human preclinical research. Here, we focus on the implementation of all optical approaches in mouse cortex. Cortical networks are critically involved in fundamental tasks of the brain, starting from sensory processing (Zagha et al., 2013, Crochet and Petersen, 2006, Petersen and Crochet, 2013), to

decision making (Francis et al., 2018, Gire et al., 2013, Chen et al., 2017) and mechanisms involved in consciousness (Redinbaugh et al., 2020, van Vugt et al., 2018). Optical neuroimaging using genetically encoded calcium indicators (Chen et al., 2013a) can resolve the activity of local neuronal population even with single-AP resolution of sparsely firing neurons. Recent advances (Ghanbari et al., 2019a, Ghanbari et al., 2019b) even allow for the detection of cortex-wide activity of thousands of neurons in real time. Certainly, despite these advances, genetically encoded calcium indicators are inherently slow, so single APs can only be resolved if the inter-AP interval is sufficiently long, preventing the resolution of individual spikes e.g. of fast spiking interneurons such as PV interneurons (Chen et al., 2013a). What is more, the frame rate of current commercially available two-photon microscopes is around 30 Hz for full-field imaging, at least for the majority of microscopes equipped with resonant scanners (Boiroux et al., 2014). Using random access scanning, the temporal resolution can be increased, but at the expense of a limited ability to do post-hoc operations for movement correction. While inertia free acousto-optic modulator (AOM) systems allow for a much higher framerate (Chen et al., 2012), the current standard in the field is single-plane full field imaging at 30 Hz, a good trade-off between speed, SNR and field of view size. This has important implications for the integration of optogenetics in an optical microcircuit imaging framework, and designing a framework which avoids the loss of even a single imaging frame is highly advisable. Here, with these limitations in mind, a concept is proposed that is focusing on artefact avoidance or removal, to retain the utmost temporal resolution. Even more so, for the relation of a per se unspecific signal i.e. the increase of fluorescence intensity to an underlying AP, specific criteria need to be met in terms of the temporal dynamics of an AP-related event. The entire work flow of an optical functional imaging approach has to be tailored, starting from the design of the hardware, to the experiment itself, and the subsequent analysis. This chapter does not strive for giving an overview of all possible solutions of the integration of

optogenetics for all-optical experiments, but rather focused on a few tried-and-tested pipelines.

1.7.1 Principles of fluorescence: one-photon excitation

Fluorescence describes the emission of light by a previously excited atom or molecule (Meschede, 2015). A photon hits an electron in the shell of the atom to be excited and raises it to the next higher energy level (Fig. 10 A, B). This electron then falls back to its basic level by emitting a photon, and the photon energy absorbed by the electron is converted into the fluorescence photon. According to the Stokes rule, the energy of the emitted photon is lower than the energy of the exciting photon. This can be explained by kinetic collision processes between the atoms. The difference in wavelength between the exciting photon and the emitted photon is known as the Stokes difference or Stokes shift (Fig. 10 C).

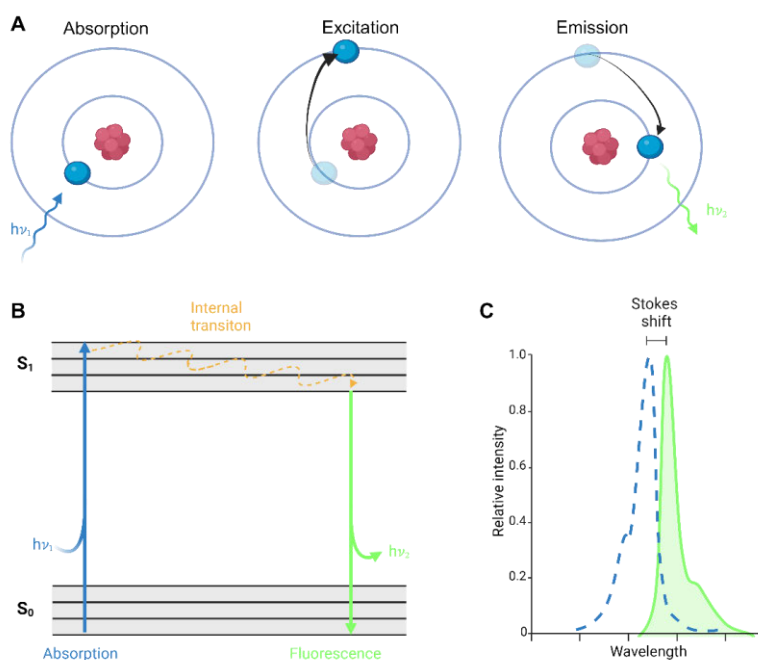


Figure 10: Principles of fluorescence excitation. (A) A photon hits an electron which in turn is shifted to the next higher shell, reaching the excitation state. Afterwards, the electron falls back to its original state while emitting a photon. (B) Representation of the absorption and emission by a Jablonski chart. (C) The emitted photon comprises a longer wavelength compared to the excitation photon. The difference between these wavelengths is called Stokes shift. Figure by Hendrik Backhaus.

1.7.2 Principles of fluorescence: two-photon excitation

An atom can also be excited under certain conditions, when two photons hit the target. Utilizing mechanisms of non-linear optics, two photons can be absorbed by the atom and contribute to the excitation if they hit the target within 10^{-15} to 10^{-18} s (Svoboda et al., 1997). The short duration is explained by the Heisenberg uncertainty principle: since there is no intermediate level between the two energy levels in the Jablonski diagram, a virtual intermediate level is used whose lifetime corresponds approximately to the duration of the absorption process (Baym, 2018). The process of two-photon absorption was first described by Maria Goepfert-Mayer in 1931 (Fig. 11).

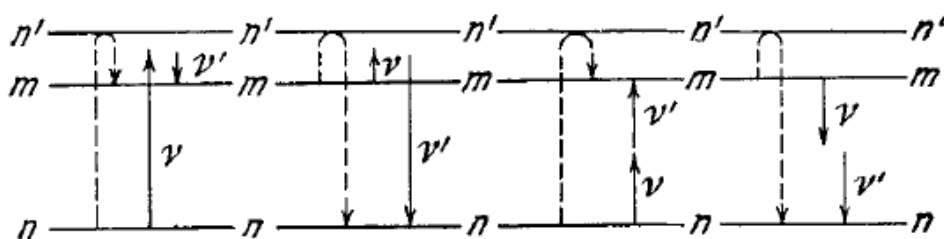


Figure 11: Initial description of multiphoton absorption by Maria Goepfert-Mayer. From left to right: Stokes-Raman effect, Anti-Stokes-Raman effect, double absorption effect, double emission effect. Dotted lines describe the energy level of the atom, lines in up direction indicate absorbed photons, lines in down direction indicate emitted photons. (Göppert-Mayer, 1931)

For two-photon absorption to take place, the sum of the energies of the absorbed photons must be the energy difference between the two energy states:

$$\Delta E = E_1 + E_2 = h\nu_1 + h\nu_2$$

However, such a process is very unlikely, as a very high temporal and spatial photon density is required. This could only be technically realized through the development of lasers emitting temporally and spatially coherent photons of long-wavelengths, which is particularly advantageous when working with in vivo samples. The penetration depth using the principle of 1-photon excitation is limited, inter alia caused by light scattering in the brain which requires a pinhole to avoid detection of scattered light that does not derive from the focal point (Helmchen and Denk, 2005, Svoboda et al., 1997). Furthermore, the deposited energy in the brain by photons of this wavelength can lead

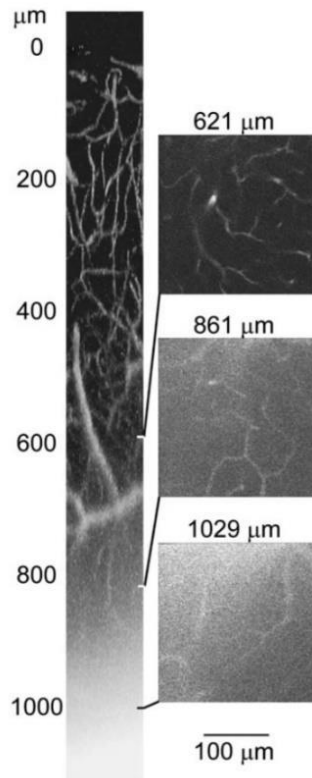


Figure 12: Cerebral blood vessels (in vivo) imaged using a two-photon fluorescence microscope. The coordinate at 0 μm represents the brain surface. Left: XZ projection, Right: Selected examples of the corresponding XY projections. The influence of the excitation photons, which lie outside the focal point and contribute to background fluorescence, becomes clear ($> 500 \mu\text{m}$ penetration depth) (Theer et al., 2003).

to phototoxicity and bleaching of the indicator (Song et al., 1995). The development of microscopes using the principles of two-photon excitation combined with raster scanning approaches (Denk et al., 1990) overcame these limitations and therefore revolutionized functional neural circuit imaging (Stosiek et al., 2003). However, two-photon imaging reaches its limit in terms of penetration depth when out-of-focus intensity reaches intensity values of the imaged plane (Fig. 12) around 500 μm (Wang et al., 2020). Furthermore, pinhole solutions became dispensable since all emitted photons necessarily originate from the fluorophores excited at the focal point. The emitted fluorescence light is collected by the objective and is deflected to a photo-multiplier tube (PMT). In front of the PMT, a spectral bandpass filter ensures that only light in the bandwidth of the fluorophore's emission band is detected (Fig. 13 A).

When recording a specimen employing two-photon microscopy, the laser is deflected by a galvo-resonant mirror system to the specimen (Fig. 13 A, B), in a raster scanning principle, covering the field of view (FOV). The dimensions of the FOV depend on the chosen objective and its numerical aperture (NA). The duration of the laser focusing a pixel is defined as the pixel dwell time. For fluorescence excitation, a pixel dwell time of 1 μs is commonly applied, resulting in frame rates of 30 Hz for galvo-resonant systems. Note, that this temporal resolution is critical for the subsequent identification of AP-related calcium transients based on their temporal dynamics.

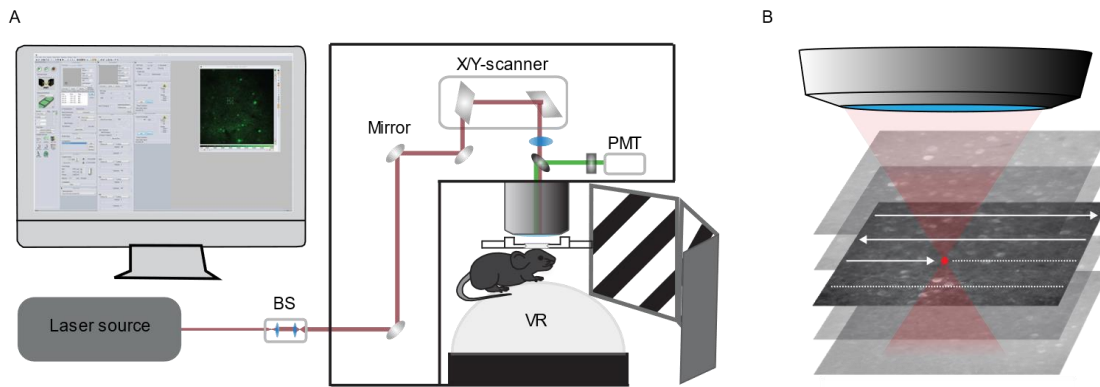


Figure 13: Illustration of a two-photon microscope and the raster-scanning principle. (A) A femtosecond-pulsed laser is guided to a beamshaper (BS) to optimize the illumination pattern and deflected by mirrors until it reaches the x/y-scanner, which is either a galvo-galvo mirror or a galvo-resonant mirror system. After the light passed the x/y-scanner, it is further guided through a lens and the dichroic mirror, comprising of spectral properties to let light of a wavelength in the range of the laser pass through, while photons of a wavelength as the fluorescence light are deflected. The laser light then is hitting the back aperture of the objective and is focused in the sample, exciting the fluorophores. The emitted fluorescence photons are collected by the objective and get deflected by the dichroic mirror towards the PMT where the photons are transformed into electrical signals. A spectral filter in front of the PMT guarantees only light of a certain wavelength can be detected. Especially for measurements in the awake animal, a spherical treadmill in combination with a virtual reality platform (VR) is essential to enable the animal to move freely while being fixated by a headholder below the objective. **(B)** The x/y-scanner causes the focal point of the laser to scan the sample lane by lane, starting from the top left corner until it reaches the lower right corner. Figure by Hendrik Backhaus, partially published in (Backhaus et al., 2023)

1.7.3 Principles of fluorescence: three-photon excitation

The principle of three-photon absorption fluorescence was first described in 1964 by Singh and Bradley (Singh and Bradley, 1964), who estimated the three-photon absorption cross section of naphthalene crystals, while the first application was in 1996 by Hell et al. who provided proof of concept using raster scanning microscopy under a three-photon regime (Hell et al., 1996).

The underlying effect that enables the absorption of 3 photons is similar to that of two-photon absorption, although there are small differences, e.g. the reduced cross section in three-photon absorption processes: while the cross section under a two-photon regime is about $10^{-49} \text{ cm}^4\text{s}/\text{photon}$, it is reduced to $10^{-83} \text{ cm}^6(\text{s}/\text{photon})^2$ in three-photon absorption (Cheng et al., 2014). To overcome the reduced cross section, the use of high-power lasers is required to deliver the necessary photon density (Toda et al., 2017). However, the advantage of three-photon fluorescence microscopy lies in the

greater penetration depths into the tissue, which allows regions below 500 μm in the cortex, such as layer V of V1 in mice, or the hippocampus to be examined. As mentioned in the previous chapter, two-photon fluorescence microscopy does not require a pinhole to block out-of-focus signals during measurements. However, the excitation power increases exponentially with image depth, so that the background intensity converges to the signal intensity, which not only reduces contrast but also creates an additional noise component that overlays the actual calcium transient signal. As a result, no evaluable signal is generated above a certain imaging depth (Wang et al., 2020) as the two-photon signal-to-background ratio (SBR) reaches a value of 1 at 4.7 attenuation lengths while the labeling density of the stained region is around 2% (Kobat et al., 2011, Theer et al., 2003, Theer and Denk, 2006). Consequently, functional two-photon imaging while employing GECIs faces technical challenges when imaging deep brain regions, which is usually overcome by removing superficial layers of the cortex or the insertion of penetrating optical elements like GRIN lenses (Attardo et al., 2015, Dombbeck et al., 2010, Low et al., 2014, Pilz et al., 2016). The use of three-photon regimes offers the possibility of avoiding these limitations, partly because of the lower tissue attenuation due to longer excitation wavelengths and the background suppression provided by three-photon excitation (Ouzounov et al., 2017).

Technical realizations of a three-photon microscope are similar to two-photon microscopes: a pulsed laser source is guided via a mirror system and focused by an objective onto the specimen, which is scanned by a raster scanning principle. The emitted fluorescence light is collected by the objective and guided to a PMT, covered with a bandpass filter to block wavelengths that are not associated to the signal of interest. The downside of the principle is, that commercially available three-photon laser sources comprise of a limited repetition rate and the required light intensity for reliable fluorophore excitation. For example, a widely used light source for two-photon excitation is a Chameleon Vision II Ti:Sa laser (Coherent Systems, CA, USA), which has a

repetition rate of up to 80 MHz at a maximum power output of 3 W, while in comparison a Carbide I-OPA system (LightConversion, Luthania) only reaches a repetition rate of 2 MHz. To reach the required pixel dwell time of 1 μ s for GCaMP, a galvo-resonant mirror system operates at a velocity which is too high for the mentioned repetition rate. Therefore, three-photon microscopy systems require the use of galvo-galvo mirror systems, resulting in a drastically reduced framerate which can only be compensated by either reducing the field of view or sacrificing image quality by lowering the matrix of pixels to 256x256 or lower that represent the field of view.

2. Material & Methods

2.1 Chronic Social Defeat and Social Interaction Test

All experiments were carried out along institutional animal welfare guidelines and were approved by the Landesuntersuchungsamt Koblenz, State of Rhineland-Palatinate, Germany.

Male C57/BL6 mice were used for experiments. Mice were group housed until the beginning of the Chronic Social Defeat paradigm. Afterwards, animals were single-housed. During the whole experiment, mice had access to food and water ad libitum.

Mice were subjected to a CSD paradigm according to established protocols (Golden et al., 2011, Krishnan et al., 2007). Mice were introduced into a home cage of an older, larger, and retired male CD1 breeder. During a physical exposure phase of 2 min, the CD1 mouse was allowed to attack the BL6 experimental mouse. For the consecutive sensory exposure phase, a mesh wall was introduced in the middle of the cage between the two mice allowing sensory but not physical contact for 24 h. The procedure was reiterated for 10 days and experimental mice were encountering different CD1 aggressors daily. On the last day of the CSD, all mice were housed individually in new cages and left to rest until the social interaction test took place one week later. The CD1 aggressors were trained for 3 days before beginning CSD to standardize attack's latency. The group of non-stressed mice were handled throughout 10 days and being placed for 1.5 min in an empty cage before being returned to their individual cages separated in half by identical mesh walls.

The SI-test was performed 7 days later (Krishnan et al., 2007, Golden et al., 2011). A mesh enclosure was presented at the center of an arena and the interaction zone was defined as 1 cm. Mice were introduced twice into the arena for 2.5 min, first with an empty mesh enclosure, followed by re-introduction with a novel CD1 mouse under the enclosure. The SI score was calculated by forming the quotient of the dwell time of the BL6 mouse within the interaction zone while a CD1 animal is in the mesh vs. an empty mesh.

2.2 Preparation

Mice were placed on a stereotactic frame (David Kopf Instruments, CA, USA) and were anesthetized with isoflurane/oxygen (2% vol/vol) by inhalation while placed on a heat plate (ATC 2000, World Precision Instruments, FL, USA) to maintain body temperature at 37°C. The skull was exposed and thoroughly cleaned from any remaining tissue. A craniotomy of 2 mm diameter was conducted at the coordinates of the primary visual cortex V1 (posterior –3 mm and lateral –2.5 mm to Bregma) using a dental drill (Ultimate XL-F, NSK, Trier, Germany, and VS1/4HP/005, Meisinger, Neuss, Germany) under a dissecting microscope (Leica M80 stereo microscope, Leica, Wetzlar, Germany). For expression of the genetically encoded calcium indicator GCaMP6f via viral gene delivery, a total volume of approximately 1.0 μ l of AAV1.CamKII.GCaMP6f.WPRE.SV40 solution was manually pressure injected with a 30° angle in 3 depths (150, 200 and 250 μ m) into V1. The craniotomy was sealed with a transparent cover slip (3 mm diameter, 0.1 mm thickness) and glued to the skull using super glue (Vetbond, 3M, MN, USA). A ring-shaped headholder with an outer diameter of 14 mm and an inner diameter of 7 mm was implanted onto the skull using UV-glue (Polytec UV-Glue 2195, Polytec PT GmbH, Karlsbad, Germany) that the notch is facing to the rear of the animal. After the procedure, mice were allowed to recover for 3 weeks prior to habituation. A detailed description of surgical methods is available at (Guimaraes Backhaus et al., 2021).

2.3 Habituation

Mice were habituated over 5 consecutive days to avoid stress exposure during imaging. On day one, mice were handled for at least 15 min to get familiar with the experimenter. On day 2 and 3, mice were constrained after at least 15 min of handling by manually holding the headholder. On day 4, mice were constrained upon handling using the retaining device that is mounted below the microscope during imaging sessions. Mice

were undergoing a mock experiment on day 5 by constraining them with the headholder and mounting them onto the spheric treadmill (JetBall-TFT, PhenoSys, Berlin, Germany) under the microscope. A 15 min recording session was simulated by activating the microscope but keeping all shutters closed to avoid photobleaching.

2.4 In vivo awake two-photon imaging

Mice were head fixated and mounted on a spheric treadmill, surrounded by a 270° screen system for presenting visual stimuli.

In vivo recordings were conducted using a custom-built two-photon microscope equipped with a resonance scanner (TrimScope II, LaVision Biotec, Bielefeld, Germany) and indicator excitation was achieved by a femtosecond pulsed Ti:Sapphire laser (Chameleon II, Coherent Systems, CA, USA). A 40x water immersion objective (0.8 NA; NIRAPO, Nikon, Tokyo, Japan) was used for imaging, resolving a field of view (FOV) of 277 x 277 μm represented in a matrix of intensity values with 512x512 pixel. Image acquisition was controlled by ImSpector Pro software (LaVision Biotec, Bielefeld, Germany) at a frame rate of 30.8 Hz. Relevant information from all subsystems were collected by a multichannel-data-acquisition interface (CED Power3, Cambridge Electronics, Great Britain) and exported subsequently to each imaging session using the software package Spike2 (Cambridge Electronics, Great Britain).

Initially spontaneous activity of a neuronal microcircuit for 15 min in layer II/III of V1 was recorded, followed by 12.5 min of visually evoked activity by employing a visual stimulation paradigm. The paradigm consisted of initially 5 sec of grey screen, followed by the presentation of 8 randomized static- and drifting grating directions lasting 5 sec each. The paradigm was repeated 10 times, every time with a novel randomization.

2.5 In vivo anesthetized two- and three-photon imaging

Two-photon imaging was conducted using the system as described in chapter 2.4, employing resonance scanning with a Ti:Sapphire laser operating at 920 nm wavelength as light source (Coherent). A 20x DIC VIS-IR water immersion objective (NA = 1.0) was used for imaging at a frame rate of 30.8 Hz resulting in a field of view of 458 x 458 μm^2 .

three-photon imaging was carried out with a novel light source consisting of a femtosecond laser system (CRONUS-3P, Light Conversion, Vilnius, Lithuania) equipped with an optical parametric amplifier (OPA) tunable between 1250 nm – 1800 nm wavelength at a repetition rate of 2 MHz. For imaging, a wavelength of 1300 nm was chosen, resulting in an output power of approximately 160 mW. The framerate was 5.46 Hz for a field of view of 159 x 54.5 μm^2 .

For both, three-photon and two-photon imaging, animals were slightly anesthetized with Isoflurane at a dose of 0.6 – 1.0 % and body temperature was maintained at 37°C. Image acquisition was controlled by ImSpector Pro software (LaVision Biotec).

2.6 Imaging data analysis

All data sets were motion corrected to address x-y-movement artefacts using the moco (Dubbs et al., 2016) plugin in FIJI ImageJ (Schindelin et al., 2012). As reference image, an average intensity projection was calculated using the z-project function of ImageJ.

A custom written MATLAB (The MathWorks, Natick, MA, USA) script was used for segmentation of all visible neuronal somata within the FOV. The algorithm created an average intensity projection of all single images of the timeseries and neurons were marked with a polygon shaped outline and defined as ROIs. All intensity values of all pixels within each ROI for every image of the series were subsequently averaged, resulting in an intensity trace per ROI. A 10 s long period of quiescence free of calcium

transients or signal fluctuations was defined as baseline F_0 for each ROI separately. The relative change of fluorescence $\Delta F/F$ was calculated for each sample point F with $\Delta F/F = \frac{F-F_0}{F_0}$ (Hendel et al., 2008).

In the next step the intensity traces were exported to a custom-written IGOR Pro (Wavemetrics Inc., OR, USA) procedure to detect putatively AP-related calcium transients. First, intensity traces were smoothed by a Gaussian Kernel 20-30 times, high-pass filtered with a pass band at $0.12/F_s$ where F_s is the sampling frequency, and inspected for the presence of calcium transients. Intensity traces that did not exhibit transients or falsely identified structures were excluded from further analysis in this step. Second, a threshold-based algorithm automatically detected signal peaks exceeding $2.5 - 3$ SD above the mean. Furthermore, the first and second derivatives were calculated, which had to be 0 and negative, respectively, to meet the criteria of an AP-related calcium transient. The typical decay of the calcium deflection was modeled by fitting an exponential curve using the CurveFit tool of IGOR Pro between the peak and the tail. If necessary, peak locations were corrected manually. Lastly, the onset of a given calcium transient was defined as the first datapoint prior the identified peak that dropped below 0.5 SD, the offset when the fitted exponential curve reached 0.5 SD of the baseline. Intensity traces were binarized by representing periods of quiescence as 0 and the sample points of a transient from on- to offset as 1.

The Circular Variance (CV) was calculated as the variance of the cell's response to all orientations:

$$CV = 1 - \left| \frac{\sum_k r_k e^{i2\theta_k}}{\sum_k r_k} \right|$$

Where r_k is the cells response to a given orientation, θ_k is the angle of the grating in radians (Ringach et al., 2002).

To test for synchronicity, activity intervals for each neuron were refined by defining the onset and offset of each identified peak as the first frame to the left and right of the peak frame, respectively, that had a $\Delta F/F$ intensity < 0.5 times peak intensity. Activity intervals were defined as all data points between onset and offset. Peaks occurring during an identified activity interval were not considered in a subsequent estimation of onset/offset but were instead considered part of the existing activity interval. The computation of $\Delta F/F$ traces in this step was adapted from the Allen Brain SDK 2.14 as a windowed median filter detrending, employing a long filter of 5401 frames and a short filter of 101 frames (Allen Institute for Brain Science, 2022, Software Development Kit [2.14]. Available from <https://allensdk.readthedocs.io/en/latest/>).

The binarized activity matrix of all ROIs was used to create pairwise correlations between each pair of ROIs to visualize the connectivity between neurons within timeframes in which at least one ROI showed activity. In the resulting connectivity map neurons were depicted as nodes based on their x and y positions and were assigned a color value that corresponded to their activity frequency. Edges between nodes were represented as lines whose linewidth were defined by the achieved correlation value.

2.7 Statistical tests

Recordings with no cell activity were excluded from the analysis. Data was tested for normal and non-normal distributions using the MATLAB function for one-sampled t-tests. Statistical tests for equal distributions were performed by employing the built in MATLAB function for two-sided Kolmogorow-Smirnow tests. For analysis of variance, Levene's test for equality of variance was done using SPSS. The significance level was set at $p < 0.05$ for all statistical tests and exact p-values were noted. Box-and-whisker plots indicate the median value (center line), the 25–75th percentiles (box) and the 10–90th percentiles (whiskers). All errors were stated as mean \pm standard error of the mean (SEM).

3. Results

3.1 A Roadmap for processing functional calcium imaging data

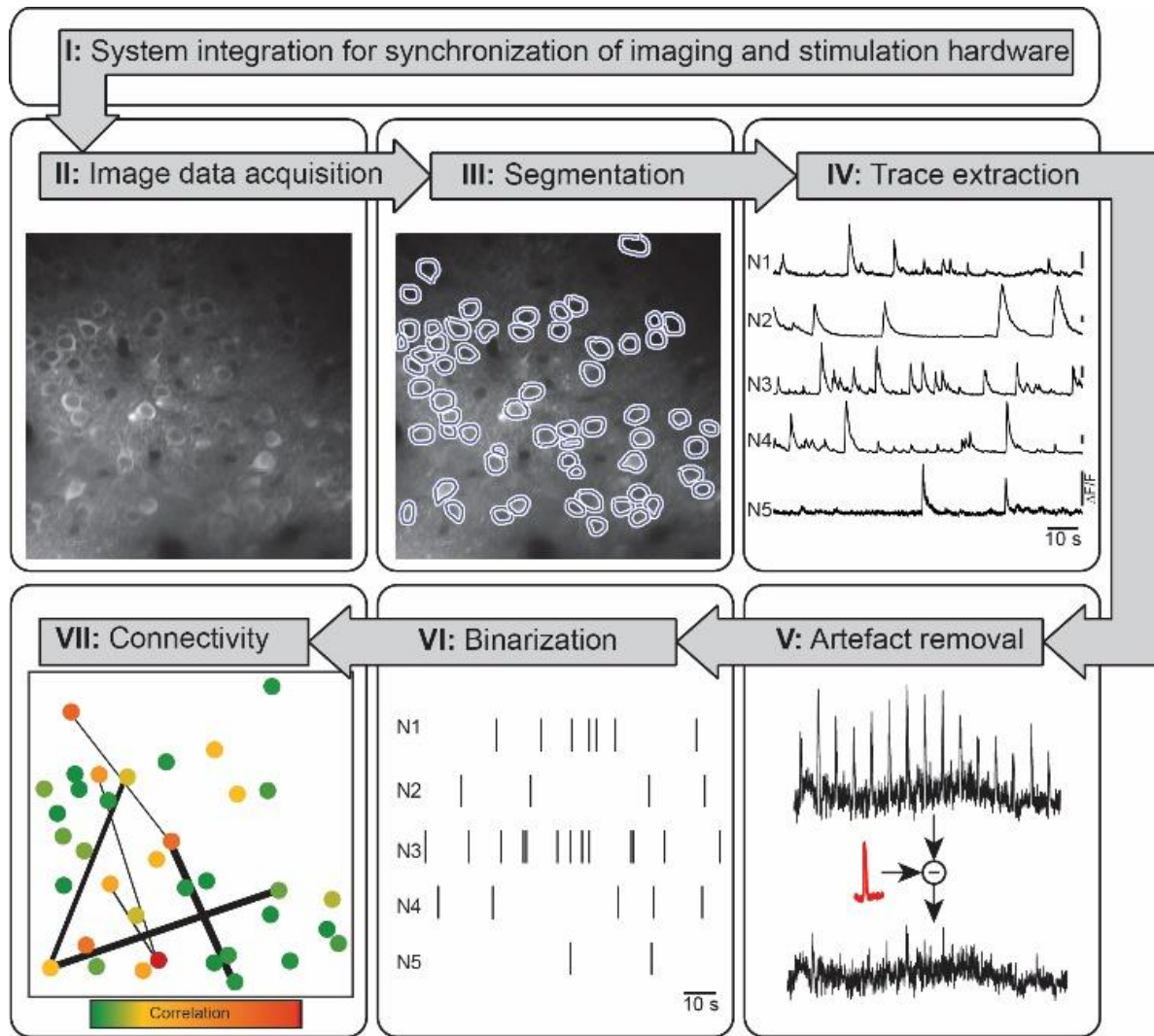


Figure 14: Workflow of a pipeline for an event related analysis of all-optical data. Raw data is segmented into ROIs and intensity traces are extracted. A binarization of transients is carried out and a temporal and spatial classification of the recorded microcircuit is applied. (Figure by Hendrik Backhaus, published in (Backhaus et al., 2023))

Regardless of the chosen technical implementation of a functional optical imaging system, the goal of any pipeline for subsequent data processing is to extract a subset of features from the raw data, either based on a priori hypotheses or by data-driven, unsupervised methods. The pipeline presented here is intended to be based on an event-related analysis: the mapping of a functional circuit of a neuronal ensemble ultimately serves only as a tool to extract the underlying action potential train of each individual neuron. Accordingly, a step-by-step guide must be established to extract putative AP-related calcium transients from the raw images. Furthermore, tuning the

microscopy system towards an all-optical approach, enabling the experimenter to manipulate the recorded microcircuit employing optogenetic tools, poses the challenge to reduce or at best avoiding photostimulation artefacts and requires a custom-tailored approach. In addition to the technical implementation of the data collection system, the necessary steps include motion correction of raw images, the segmentation of neuronal somata within the field of view, trace extraction of each labeled somata, potential artifact corrections, binarization to reduce the multitude of information and a connectivity analysis to draw conclusions about the functionality of the microcircuit (Fig 14).

Once this optically derived matrix of AP-related events is generated, e.g., by converting an extracted intensity trace into a binarized sequence of zeros and ones, already well-established correlation or interaction concepts can be applied to these dimensionality-reduced datasets.

3.1.1 System integration

Before commencing an experiment, the synchronization of all required subsystems must be ensured: all relevant trigger and stimulation pulses must be exported to an interface for multi-data acquisition. These signals include the frame trigger of the microscope, the logic level that controls the light source for opsin excitation, and biomonitoring signals such as respiratory rate and body temperature, as well as systems for recording the animal's movements, the administration of rewards such as sucrose water or punishments such as airpuffs. The system used in this work consists of a CED Power 1401-3 with a Spike2-expansion box (Cambridge Electronics, UK), a multi-data acquisition interface consisting of 24 ADC input channels, 6 ADC output channels, as well as 24 digital input channels and 16 output channels. The sampling rate of the channels is 2 kHz. The signals are imported, synchronized and digitized here. After digitization, the signals are displayed centrally by control software and a master file is created for each experiment. Reading out the master files enables a post

hoc exact assignment of each raw image to a specific point in time and, for example, the status of the stimulation regime.

3.1.2 Image data acquisition

Regardless of whether a measurement was carried out in the awake or anesthetized animal, the data sets created should be subjected to motion correction. Movement artifacts can have a variety of causes: for example, the heartbeat leads to a pulsation of the brain tissue (Paukert and Bergles, 2012) but breathing also leads to displacements in the field of view (Presson et al., 2011). Motion artifacts are particularly pronounced when the measurement is carried out in an awake animal, as locomotion on a trackball or treadmill often leads to changes in the field of view. Motion artifacts can be divided into two categories: Displacements caused by movements in the x-y plane and those occurring in the z plane. Correction of changes in the x-y plane is possible post hoc by algorithms based on the hidden Markov model (Dombeck et al., 2007) or the discrete Fourier transform (Kaifosh et al., 2014), provided that the field of view is big enough. It is important to note that the potential for correction of x-y motion is the main reason why random-access scanning is not always advisable. Conversely, handling motion in the z-plane is more complicated. Since resonance imaging in one plane has been used predominantly in the field of optical imaging, if a neuron's soma is moved out of the current x-y imaging plane, the lost information cannot be recovered. A possible solution to this dilemma is to capture a 3D volume. However, this inevitably leads to reduced temporal resolution for each recorded neuron. Particularly when using common resonance systems with a frame rate of 30 Hz, it is not advisable to acquire 3D volumes, as temporal resolution is critical for later identification of putatively action potential-related calcium transients.

This case highlights the need for analytical requirements that must underlie the preceding technical implementation steps: every effort should be made to minimize

movements by developing mechanical stability - this point cannot be overemphasized. To ensure utmost stability, a headholder needs to cover both hemispheres of the skull and a maximum adhesive surface is required. The headholder in this thesis is adapted from Hefendehl et al. (Hefendehl et al., 2012). It is a flat cylinder made of titanium, the inner edge of which is tapered in order to maximize the adhesive surface and to bring the objective as close as possible to the optical window.

3.1.3 Segmentation

The use of raster scan methods to excite fluorophores requires a post hoc representation of the time course of the fluorescence changes. This is done by displaying the individual focus points in a matrix of pixels. Strictly speaking, the size of this matrix can be freely chosen, although within the community a representation of the FOV in a matrix of 512x512 pixels has been established. The recorded raw images comprise of various biological compartments like neuronal somata, axons, dendrites, blood vessels, and a multitude of non-neuronal cells such as astrocytes. The vast majority of these components do not contribute to the signal of interest and therefore it is advisable to segment only the components that contribute to the signal of interest. The goal of optical imaging of neuronal microcircuits employing calcium indicators is to identify neuronal suprathreshold activity which is reflected by a change of fluorescence in neuronal somata. Consequently, each neuronal soma needs to be labeled and segmented as a Region of Interest (ROI) and thereby being defined as a functional unit within the microcircuit. Furthermore, demarcating neuronal somata allows for merging several pixels within each ROI, increasing the number of pixels that contribute to the signal course of each functional unit versus its background.

In recent years a rapid growth in applications that assist researchers in ROI segmentation has been taking place. Especially the rise of mathematical models utilizing deep learning algorithms have significantly simplified the time-intensive process of manually identifying neurons within recorded images (Soltanian-Zadeh et

al., 2019). In particular, minimizing human bias through a tool that is subject to systematic errors, which in turn can be characterized, has led to better comparability between different measurements. A multitude of deep learning-based techniques have been established which analyze the average of all images or methods which also take temporal information of neuronal activity into account by utilizing subsets of images to segment active ROIs (Soltanian-Zadeh et al., 2019, Klibisz et al., 2017).

The approach reported by Soltanian-Zadeh's and colleagues is based on a neural network and uses a subset of images as a predictor to generate 2-dimensional probability maps for active neurons. A threshold is subsequently applied to exclude low-probability regions from each map and high-probability regions are extracted, depicting possible somata locations (Soltanian-Zadeh et al., 2019). In the last step, all identified soma positions from each probability map in the sequence are combined to yield a final output of active soma areas.

A major problem in functional calcium imaging is the variability of data quality: as soon as a data set has a low signal-to-noise ratio, deep learning algorithms reach their limits. This is why manual segmentation by labeling neuronal somata through polygonal marking is still a commonly used approach. Therefore, when analyzing datasets exhibiting a weak GCaMP expression, a refinement of ROIs containing neuronal somata might be useful when targeting changes in calcium concentrations. A useful tool to achieve this is the FISSA toolbox: here, a given ROI is expanded in cardinal and diagonal directions beyond the soma region, subsequently splitting them into multiple neuropil regions surrounding the initial ROI. The neuropil subregion's size is equivalent to the size of the initial ROI. In theory, a given ROI's intensity trace comprises of a mixture of different underlying signal components, where one signal component represents the actual somatic signal of interest. A non-negative matrix factorization or an independent component analysis is carried out and a blind source separation is employed. This results in the identification of the underlying signal components that

contribute to the time course of the initial ROI. Under the assumption that each component is present in the central ROI and expecting that the somatic signal is the predominant signal component, the most potent signal is defined as the somatic signal (Keemink et al., 2018). Datasets comprising of a particular low SNR can be denoised with this procedure, simplifying the consecutive analysis steps.

3.1.4 Trace extraction

After all neuronal somata within the FOV are identified and marked as a ROI, the signal course over time is extracted for each ROI. The temporal resolution is determined by the employed frame rate throughout data collection. First, signal intensities of all pixels within a given ROI are averaged for each frame, resulting in an intensity trace for each ROI. Second, as the absolute level of intensity is depending on several criterions, e.g. GECI expression levels, autofluorescence, stray light that enters the objective, which can fluctuate even in different ROIs within the same measurement, the relative change of fluorescence needs to be calculated. Changes in dynamics, depending on their temporal characteristics, are likely to be associated with changes in intracellular calcium levels, termed calcium transients.

Furthermore, when extracting the signal time course, bleaching artefacts need to be addressed which cause a drift in baseline levels, especially at the beginning of measurements. There is a multitude of approaches available and a universally agreed-upon method does not exist. However, only linear operations can be employed to guarantee the preservation of calcium transients. A simple yet straight forward method is to define a sufficiently long period of quiescence within the time course of a ROI where no calcium transients are observable and to label this interval as baseline F_0 . This is done for each ROI separately (Ellwardt et al., 2018, Arnoux et al., 2018). Subsequently, the relative change in fluorescence is computed by relating the intensity

of each time point (F) to the baseline fluorescence, following the formula $\Delta F = \frac{F-F_0}{F_0}$ (Hendel et al., 2008).

3.1.5 Artefact removal

Prior to binarizing the obtained intensity traces, it is necessary to identify and potentially correct any photostimulation artifacts that might be masking the signal. Defining characteristic properties of these artifacts can facilitate their reliable identification and subsequent adjustment.

To discern between an artifact and a physiological response, an essential distinction lies in the inherent variability of physiological signals. Artefacts, with few exceptions, tend to exhibit consistency. Overlaying and averaging individual responses thus offer valuable insights into the likelihood of a physiological origin. This is achieved by assessing the temporal section of a trace following photostimulation using an $n*m$ matrix M , where n represents stimulus intervals and m equals total frames per stimulus/ n . Figure 15 B portrays an overlay of intensity traces from all photostimulation periods in Figure 15 A (shown as grey lines).

Photostimulation artifacts typically showcase distinct characteristics: Firstly, they demonstrate both a rapid onset and a sharp offset. While physiological calcium transients might also display a sharp onset due to calcium's affinity to the indicator (represented by a small dissociation constant K_d) and the steep calcium influx gradient, they exhibit a gradual decay, a consequence of the indicator's high affinity to calcium. The off kinetics does not accurately mirror the actual time course of somatic calcium concentration decrease. Secondly, if the intensity deflection duration matches the light administration duration, a physiological origin is highly implausible. As shown in Figure 15 B, intensity traces during photostimulation exhibit both these features.

Additionally, depending on the imaging setup used, the latency between the stimulation pulse onset and the putative response plays a critical role: A latency < 3 ms cannot be

deemed a physiological response, considering the time required for action potential initiation and calcium influx into the cytosol. It is important to note that this criterion applies only if the sampling rate of the GCaMP emission channel is high enough to resolve durations less than 3 ms.

Lastly, a physiological response might exhibit adaptation and might not occur with every stimulus, possibly due to changes in local inhibition (Stroh et al., 2013). Hence, while a signal deflection could indeed arise from a physiological response if it occurs with every stimulus, if the response's amplitude drastically changes or if it's intermittently absent, it is more likely to be of physiological origin. To test this, modulating the light intensity of the optogenetic stimulus could be informative: If reducing stimulation leads to the sudden disappearance of a transient, an AP-related origin is probable. However, a technical artifact would simply scale with light intensity, though nonlinear correlations can also occur. Certainly, conducting a control experiment involving indicator-only expressing cells is essential in any scenario.

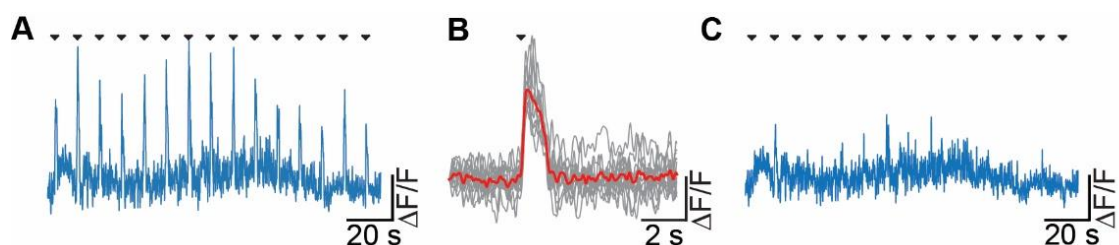


Figure 15: Evaluation of photostimulation artefacts. (A) Artefacts caused by photostimulation do not represent a physiological signal. Onsets of photostimulation are indicated by black triangles (B) By overlaying (grey) and averaging (red) periods of photostimulation, an estimation on the impact of the artefact can be made. Here, 100 sample points prior and 200 sample points after the photostimulation onset, indicated by the black triangle, are considered. The averaged signal waveform can be used in an algorithm to minimize the photostimulation artefact. (C) Subtracting the averaged waveform depicted in (B) at each stimulation onset can reduce the intensity of the photostimulation artefact. Note that signal components containing the physiological signal of interest can be altered by the algorithm as well and, in the worst-case scenario, will be completely eliminated. (Figure by Hendrik Backhaus, published in (Backhaus et al., 2023)).

Correcting photostimulation artifacts in the intensity trace is a meticulous task that requires careful execution. One possible strategy involves utilizing non-negative matrix factorization (Pnevmatikakis et al., 2016) to isolate the background noise present in a specific ROI containing the stimulation artifact. In the subsequent step, the isolated noise component is subtracted from the ROI's signal (Yang et al., 2018). For illustrative

purposes, an averaged intensity trace is extracted from all photostimulation time periods (Fig. 15 B). This value is then subtracted from the raw intensity trace (Fig. 15 A). This operation yields an intensity trace that is largely free from non-physiological signal sources (Fig. 15 C). It's important to exercise caution with the processed intensity trace, as fluctuations in the signal still persist, which might be misconstrued as functional calcium transients. Moreover, methods based on intricate mathematical models often appear as opaque solutions, posing difficulties for non-experts in understanding their underlying mechanisms. The importance of devising experimental setups that minimize the occurrence of stimulation artifacts during measurement and reducing the necessity for extensive post-processing of raw data is advisable whenever possible. The distinct temporal dynamics and latencies of the employed GECI, as discussed earlier, can serve as a validity check. Consequently, proceeding with an event-based identification of action potential-related calcium transients becomes essential.

3.1.6 Towards cross-talk-free experimental designs

a) Assessing the impact of continuous illumination for calcium imaging on opsin excitation

While the strong light intensities needed for an effective excitation of an opsin pose the aforementioned problems for simultaneous functional calcium imaging, it is also necessary to consider a putative impact on the constant excitation of the calcium indicator in terms of unwanted activation of opsins. Firstly, the activation of an opsin requires a distinct quantal energy, in case of the ChR2-based opsins or the cis-trans isomerization of retinal, this threshold ranges at 0.1 to 1 mW mm⁻². All optical one-photon experiments, even using the same wavelength for imaging and opsin activation, is therefore possible, as long as the excitation wavelengths intensity ranges below this threshold (Adelsberger et al., 2014, Stamatakis et al., 2018, Stroh et al., 2013).

However, for two-photon raster scanning conditions, the effective light intensity per pixel can well exceed this barrier. Fortunately, there is also a temporal barrier. It so seems, that any pixel dwell times below 3.2 μ s are not sufficient for opsin excitation (Packer et al., 2012). Pixel dwell times of regular resonant scanning ranges well below that number.

b) *Increasing the spectral separation between opsin and indicator to minimize optogenetic stimulation artefacts on the imaging data*

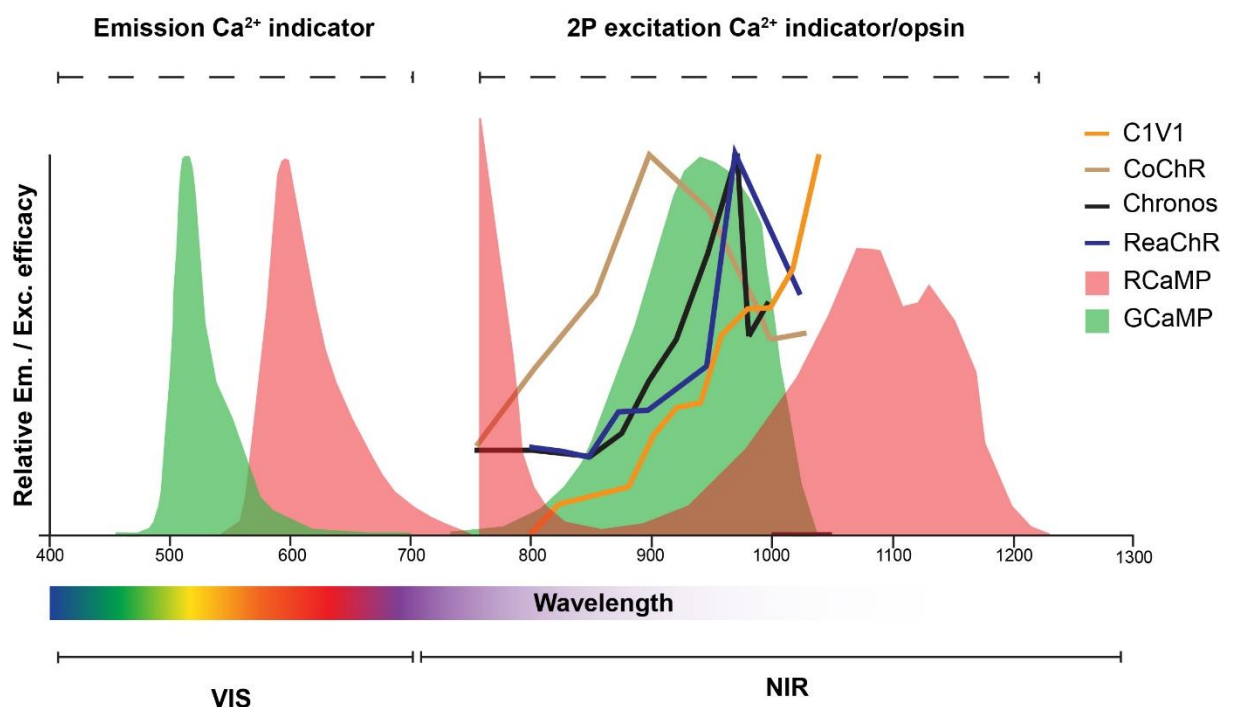


Figure 16: A selection of calcium indicator opsin pairs and their spectral properties under a two-photon regime. Cross-talk between indicator and opsin can be avoided by choosing a pair with non-overlapping excitation and emission wavelengths. For example, we used the combination of GCaMP6f, excited at 920 nm, and C1V1T/T was excited above 1100 nm to reach cross-talk free imaging. (Figure by Hendrik Backhaus and [redacted], published in (Backhaus et al., 2023))

Avoiding cross-talk in the GEI emission channel is an important criterion in the design of all-optical experiments. Both for one-photon and two-photon regimes, the excitation light can be rather easily prevented from entering the PMTs, e.g. by notch filters. But nonetheless, the strong light pulse might lead to a broadband increase in autofluorescence, also in the emission band of the fluorescence calcium indicator, leading to a decrease in signal-noise-ratio. While in principle, the utmost spectral

separation of opsin and indicator excitation wavelengths is advisable (Fig. 16), there might be good reasons to choose an opsin indicator pair with similar or even identical excitation wavelengths, if e.g. both indicator and opsin are best suited for the scientific question at hand. Post-hoc identification of photostimulation artefacts are manifold and should be conducted with utmost care. Common approaches compare the dynamics of the signal's intensity during photostimulation to the expected dynamics of calcium transients (Carrillo-Reid et al., 2016) to make an assumption of the presence of a physiological response. As a consequence, the specificity of the analysis towards the detection of action-potential related calcium transients is reduced. Other approaches sacrifice pixels that are considered to contain signal components that represent an artefact (Chen et al., 2019, Marshel et al., 2019) at the cost of a reduction of the field of view. Another option, if a spectral separation of excitation and emission wavelengths cannot be implemented, is to perform gating of light sources, inevitably leading to a loss of data (Mardinly et al., 2018). Yet, it is possible to avoid any stimulation artefact altogether, which has to be tailored for each opsin / GECI pair. For the pair GCaMP6 / C1V1, artefact free all optical physiology experiments are possible if using excitation wavelengths at or exceeding 1100 nm while simultaneously imaging GCaMP6-fluorescence at 920 nm (Fu et al., 2021).

3.1.7 Event-related binarization

Action potential-related calcium transients exhibit characteristic signal dynamics and waveforms. From a methodological standpoint, the rather predictable dynamics of somatic calcium influx and re-uptake, as well as the binding dynamics of the fluorescent calcium indicator (Mank et al., 2008), are intertwined. Consequently, each binarization approach must be meticulously tailored to the specific calcium indicator employed. The resulting calcium transients tied to action potentials can be characterized based on parameters such as rise time, decay, and duration. Alternatively, an idealized transient

waveform can be employed for deconvolution methods (Friedrich et al., 2017, Kerr et al., 2005, Pachitariu et al., 2017).

An important aspect in the process of binarizing functional calcium transients is the avoidance of false positively identified events. Therefore, the chosen algorithm needs to be capable not only to identify the presence of functional calcium transients, termed sensitivity, but also be utmost specific in the detection and avoid to identify events that are not underlying any neuronal activity. The accuracy of the chosen method should be tested in datasets where the ground truth of ongoing neuronal activity is known, e.g. by a combining measurement of neuronal activity employing juxtacellular recordings and two-photon microscopy. Only then a conclusion can be drawn how accurate the binarization represents the actual neuronal network activity.

A relatively straightforward yet highly effective method, known for its low false positive rate (Arnoux et al., 2018, Ellwardt et al., 2018, Fu et al., 2021), involves a threshold-based algorithm. In this approach, the standard deviation of the noise band within the trace is first determined, ideally in a section of the trace devoid of the signal of interest. In cases of all-optical experiments, time periods outside of stimulation events and featuring minimal spontaneous activity should be selected. When the signal surpasses this threshold, and if additional criteria like minimal duration are fulfilled, a potential event is identified. Furthermore, given that the decay of an action potential-related calcium transient generally follows an exponential pattern — true for commonly used indicators like GCaMP6 and OGB-1 — a trace regression employing an exponential function can be executed. The goodness of fit for this regression provides further evidence of the physiological nature of the identified transient. By identifying the onset, peak, and offset for each detected transient, a fluorescence signal can be represented as a binarized event array. It is worth noting that deconvolution-based methods also generate such binarized arrays. Subsequent analyses are performed on these condensed datasets.

3.2 Accuracy assessment: Verifying putatively Action Potential-related calcium transient representation in an analysis pipeline

3.2.1 Probing the algorithm for accuracy of sensitivity and specificity

To test for the specificity and sensitivity of the detection algorithm, here, simultaneous juxtacellular electrophysiological recordings and two-photon calcium imaging in the visual cortex of the lightly anesthetized mouse was carried out (Fig. 17 A). The bimodal recordings comprise of a stable calcium trace with large-scale deflections which was synchronized with juxtacellular recordings in voltage clamp mode (Fig. 17 B), exhibiting typical sparse spontaneous AP firing (Rocheffort et al., 2009). The peak detection criteria was adjusted to avoid the detection of false positives, to ensure that calcium peaks were not detected in the absence of temporally locked APs. Sensitivity and specificity plots for calcium transient detection were based on the chosen standard deviation threshold. Applying a threshold of 0.05 standard deviation resulted in a mean sensitivity of $80 \pm 9\%$, reaching a specificity of $30 \pm 13\%$. An increase of the threshold to 0.2, 0.5 SD, and 1 SD is reducing the sensitivity to $75 \pm 10\%$, $75 \pm 14\%$, and $73 \pm 15\%$ respectively. The corresponding specificity for an SD threshold of 0.2 and 0.5 increases to $40 \pm 19\%$ and $66 \pm 21\%$, respectively; a threshold of 1 SD reaches 100% specificity ($n = 7$ neurons, 3 mice, Fig. 17 C). The Sensitivity/Specificity plot utilizing the OASIS deconvolution toolbox was generated by employing a variation of the limit of the peak detection of the estimated noise band. A to 100 % limit results in a mean sensitivity of $91 \% \pm 12 \%$ at a specificity of $15 \% \pm 9 \%$. Increasing limits to 300, 500, 700 and 1000 % of the noise band reduces the sensitivity to $84 \% \pm 13 \%$, $72 \% \pm 14 \%$, $63 \% \pm 18 \%$, and $53 \% \pm 21 \%$ while the specificity increases to $30 \% \pm 9 \%$, $48 \% \pm 16 \%$, $54 \% \pm 18 \%$, and $67 \% \pm 25 \%$ (Fig. 17 D).

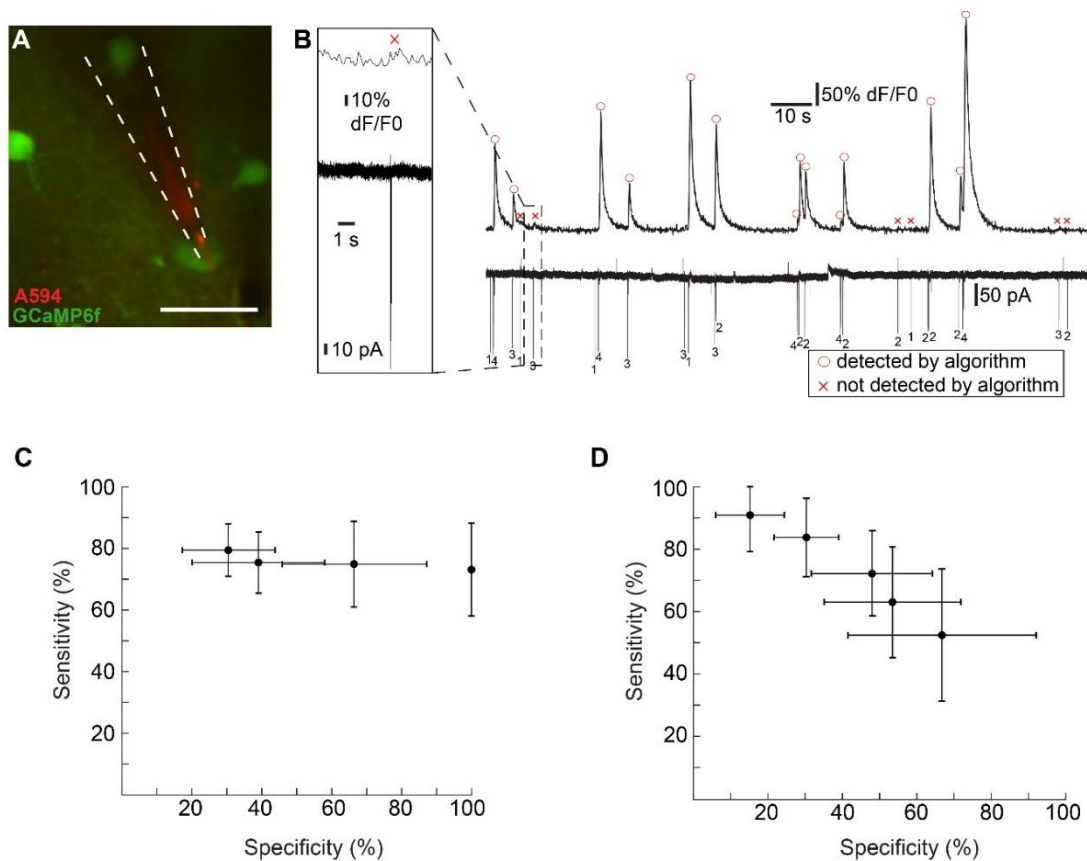


Figure 17: Comparison of a threshold-based algorithm with a deconvolution approach in terms of sensitivity and specificity in the detection of putatively AP-related calcium transients. (A) Simultaneous two-photon imaging and juxtacellular recordings of GCaMP6f-expressing neuron (green). Patch pipette filled with AlexaFluo594 (red), scale bar: 20 μ m. Experiment conducted by [REDACTED]. **(B)** Spontaneous activity of a GCaMP6f-expressing neuron. Calcium trace acquired with 2-P imaging (upper) and current trace (lower) obtained by juxtacellular recording of the same neuron. AP-associated calcium transients as detected by the algorithm are marked by a red circle. APs not accompanied by detected calcium transients are marked by a red cross in the calcium trace. Numbers of APs are indicated below the trace. Experiment conducted by [REDACTED]. **(C)** Sensitivity and specificity for calcium transient detection based on the chosen standard deviation threshold. Applying a threshold of 0.05 standard deviation (SD) results in a mean sensitivity of $80 \pm 9\%$, reaching a specificity of $30 \pm 13\%$. An increase of the threshold to 0.2, 0.5 SD, and 1 SD is reducing the sensitivity to $75 \pm 10\%$, $75 \pm 14\%$, and $73 \pm 15\%$ respectively. The corresponding specificity for an SD threshold of 0.2 and 0.5 increases to $40 \pm 19\%$ and $66 \pm 21\%$, respectively; a threshold of 1 SD reaches 100% specificity ($n = 7$ neurons, 3 mice). **(D)** Sensitivity / Specificity plot employing OASIS deconvolution toolbox. Setting the limit of the peak detection to 100 % of the estimated noise band results in a mean sensitivity of $91 \% \pm 12 \%$ at a specificity of $15 \% \pm 9 \%$. Increasing limits to 300, 500, 700 and 1000 % of the noise band reduces the sensitivity to $84 \% \pm 13 \%$, $72 \% \pm 14 \%$, $63 \% \pm 18 \%$, and $53 \% \pm 21 \%$ while the specificity increases to $30 \% \pm 9 \%$, $48 \% \pm 16 \%$, $54 \% \pm 18 \%$, and $67 \% \pm 25 \%$. (Figure by Hendrik Backhaus and [REDACTED], published in (Fu et al., 2021)).

3.2.2 Characterization of neuronal single cell activity during slow waves

Excursus: Am I awake, am I asleep or neither?

Periods of rhythmically occurring slow wave activity (< 1 Hz) during physiologically induced slow wave sleep (SWS, refers to a sleep stage with the typical slow delta oscillations), as well as induced by administration of anesthetics, are known across species (Destexhe et al., 2007, Buzsaki et al., 2013) and are among the most popular activity patterns during sleep in the human brain (Achermann and Borbely, 1997, Massimini et al., 2004). This activity pattern is characterized by the occurrence of active states (up states or slow wave events (SWE)), in which cells are depolarized and fire synchronously, alternating with inactive resting periods (down states), during which hardly any neuronal activity takes place and membrane potentials tend to be hyperpolarized. At least during SWS, this oscillatory activity has been associated with the repetition of activity patterns that occurred in connection with task learning or processing of waking experiences (Ribeiro et al., 2004) and thus probably plays a crucial role in memory consolidation and synaptic plasticity. The underlying mechanism may be the slow wave itself (Euston and Steenland, 2014), as it has been shown that Calcium activity following sensory stimulation that occurs during an up state controls synaptic excitation (Chen et al., 2013b). The importance of slow waves in relation to learning ability and memory consolidation in the human brain has already been confirmed (Marshall et al., 2006). In rats (Mölle et al., 2006) and humans (Staresina et al., 2015), rapid field potential fluctuations, so-called sharp wave ripples, and sleep spindles were observed in the hippocampus due to slow waves. This supports the hypothesis that the excitation associated with slow waves has a synchronizing function in corticohippocampal coupling. The long-range coherence of slow waves forms the temporal framework for linking spatially separated neurons into functional units (Gray and Singer, 1989) and could thus indirectly modulate spatially localized, faster rhythms such as beta and gamma oscillations (Compte et al., 2008).

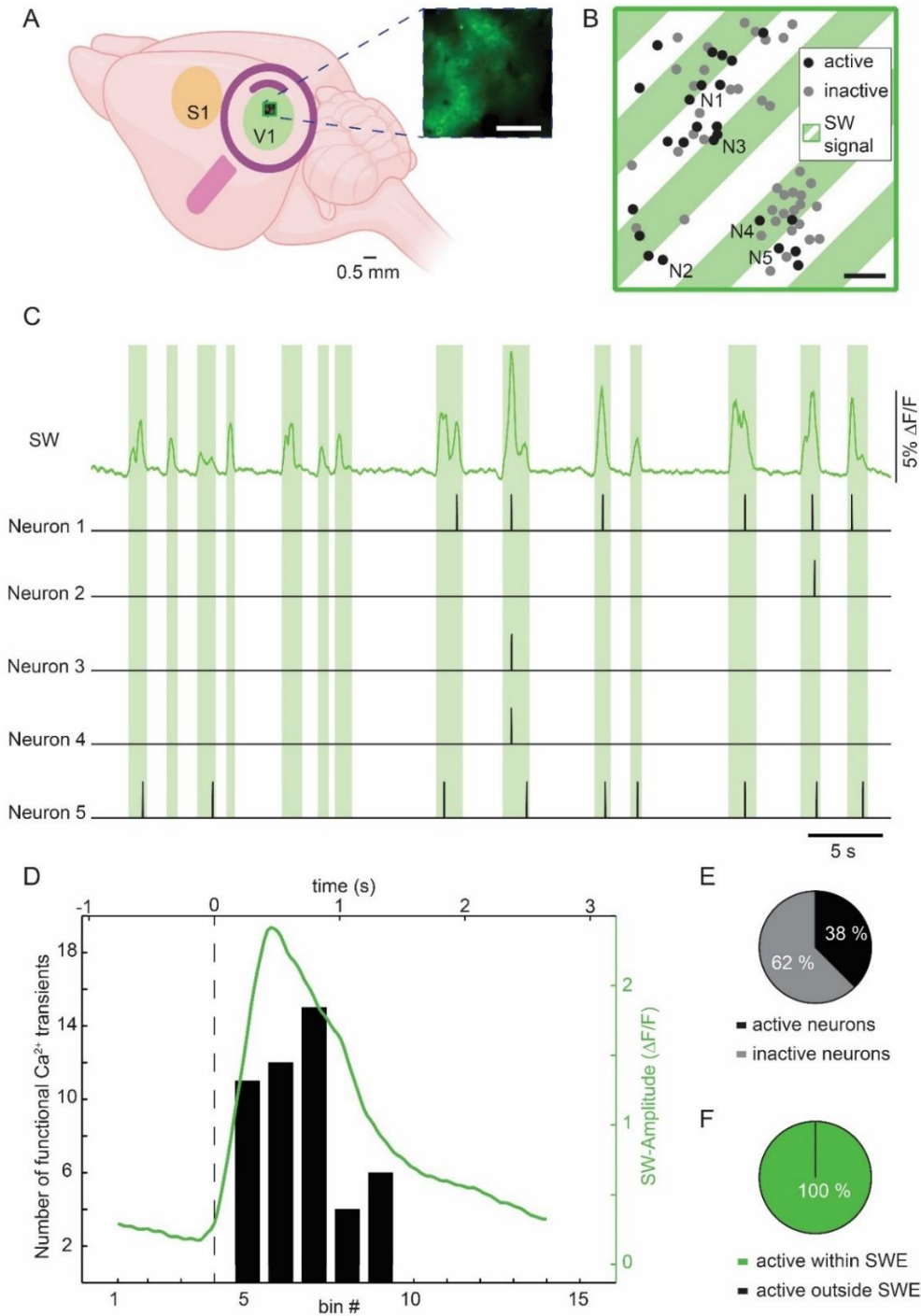


Figure 18: Functional two-photon calcium imaging reveals neuronal activity during slow wave events. (A) Schematic representation of the location of the region of interest for data acquisition employing functional two-photon calcium imaging in layer II/III of the visual cortex in mice. Scale bar represents 50 μm . (B) Segmentation of the field of view for signal extraction. Black dots represent active neurons and gray dots inactive neurons. Slow wave events are obtained by averaging the signal from the entire field of view while excluding signal contributions of ROIs representing neuronal somata, depicted as green frame. Scale bar is 50 μm . (C) Overlay of the slow wave signal (green line) with binarized intensity traces of individual neurons (black lines). The identified slow wave events are highlighted as green boxes and were superimposed over the signal curves. (D) Histogram of all detected functional calcium transients during slow wave events. The slow wave depicted (green line) is the averaged time course of all identified slow wave events. The dashed line represents the onset of the slow wave events. (E) Out of 64 identified neurons, at least one functional calcium transient was detected in 38% of the neuronal population within the field of view, which occurred in 100% during the presence of a slow wave event (F). (Figure by Hendrik Backhaus, figure 18 A modified by [redacted]).

To investigate the relation of single neuron activity to population SWEs in neuronal networks, two-photon calcium imaging in visual cortex layers II/III of head fixed mice was performed (Fig. 18 A). To obtain a slow wave dominated brain state, animals were anesthetized with isoflurane. Integrating all neuronal activity over the entire FOV, typical SWEs followed by network quiescence were observed, indicative of slow wave activity (Fu et al., 2021; Schwalm et al., 2022) (Fig. 18 B, C). Within the FOV, only 38 % of neurons exhibited spontaneous calcium transients under these conditions (Fig. 18 E). The onset and offset of all FOV-wide SWEs were identified This SWE population then was overlaid with the binarized single cell activity (Fig. 18 C).

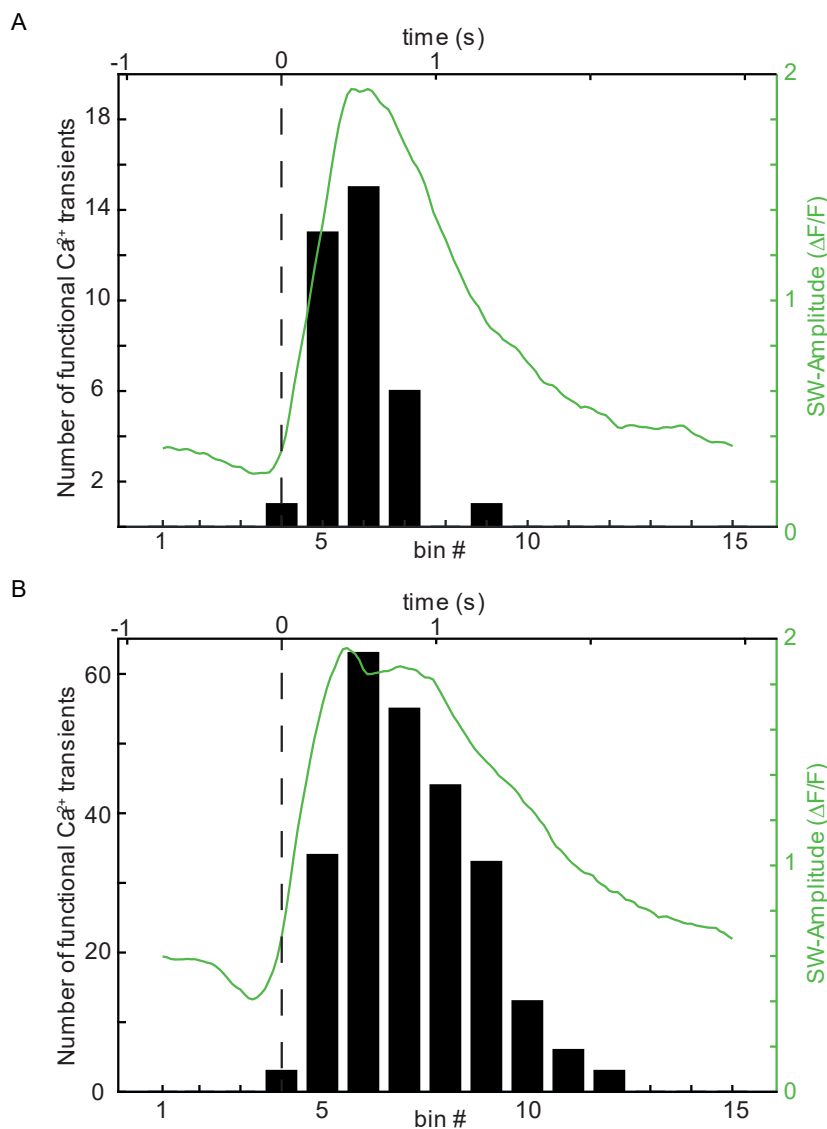


Figure 19: The relationship of single-cell activity with slow wave events persists across different animals. (A, B) Histogram of all detected functional calcium transients during slow wave events within animal 2 and 3. The slow wave is depicted as green line and the dashed line represents the onset of the slow wave events. The vast majority of neuronal activity (100% in animal 2 and 98,05% in animal 3) occurs during slow wave events. (Figure by Hendrik Backhaus).

The same correlations between neuronal activity and the presence or absence of SWEs were also observed in two other measurements. Here, too, neuronal single-cell activity could be detected exclusively during the occurrence of an SWE (Fig. 19). The measurements also showed that only a small number of neurons within the recorded network showed activity. Only in one measurement was activity also measured outside of an SWE. However, this only represents a relative rate of less than 2% in relation to all detected single cell activities (Table 2).

Animal	Number of Neurons	Active	Inactive	% active within SWE	% active outside SWE
1	64	37,50%	62,50%	100%	0%
2	84	16,67%	83,33%	100%	0%
3	53	18,87%	81,13%	98,05%	1,95%

Table 1: Result overview of the correlation between single cell activity and SWEs. Only a subfraction of the neurons shows activity, but mainly during the presence of an SWE.

The calcium transients of neuronal somata reflect action-potential correlated activity (Fu et al 2021). Notably, single neuron activity occurred exclusively within the SWE envelope. The relative number of calcium transients on the single neuron level corresponded well with the temporal characteristics of the circuit-wide SWE. This indicates that the dynamics of population SWEs and single neuron activity are related, with the single cell activity likely being the main source of the population SWE providing a window of opportunity for suprathreshold activity.

3.3 Stress resilience is reflected in cortical microcircuit architecture

3.3.1 Combining the behavioral paradigms of chronic social defeat and social interaction with awake two-photon neuronal microcircuit recordings in the visual cortex

To simulate severe stress exposure, male BL6 mice were subjected to a chronic social defeat (CSD) paradigm. This involved exposing the experimental mice to different aggressors each day over a span of 10 consecutive days. On a daily basis, the experimental mouse was introduced into the retired CD1 breeder's home cage (Fig 20 A-I), which resulted in the aggressor attacking the intruder (Fig 20 A-II). After a 2-minute physical exposure phase, the animals were separated by a mesh that allowed sensory perception but prevented physical interaction (Fig 20 A-III). The experimental mouse then stayed in the aggressor's cage for the subsequent 24 hours. Following the CSD period, a social interaction (SI) test was conducted (Fig 20 B). In this test, the experimental mice were placed in an unfamiliar cage, with an initially empty mesh placed in one corner. The time spent in close proximity to the mesh was measured. The test was repeated with a retired CD1 breeder introduced into the mesh. The SI score, calculated as a measure of stress resilience, indicates whether the mouse spent more time near the separated aggressor. A higher SI score signifies increased stress resilience, suggesting that the mouse can differentiate between contexts (Krishnan et al., 2007, Lyons et al., 2023). This indicates that the aggressor is not seen as a threat, allowing the mouse to engage in social interaction.

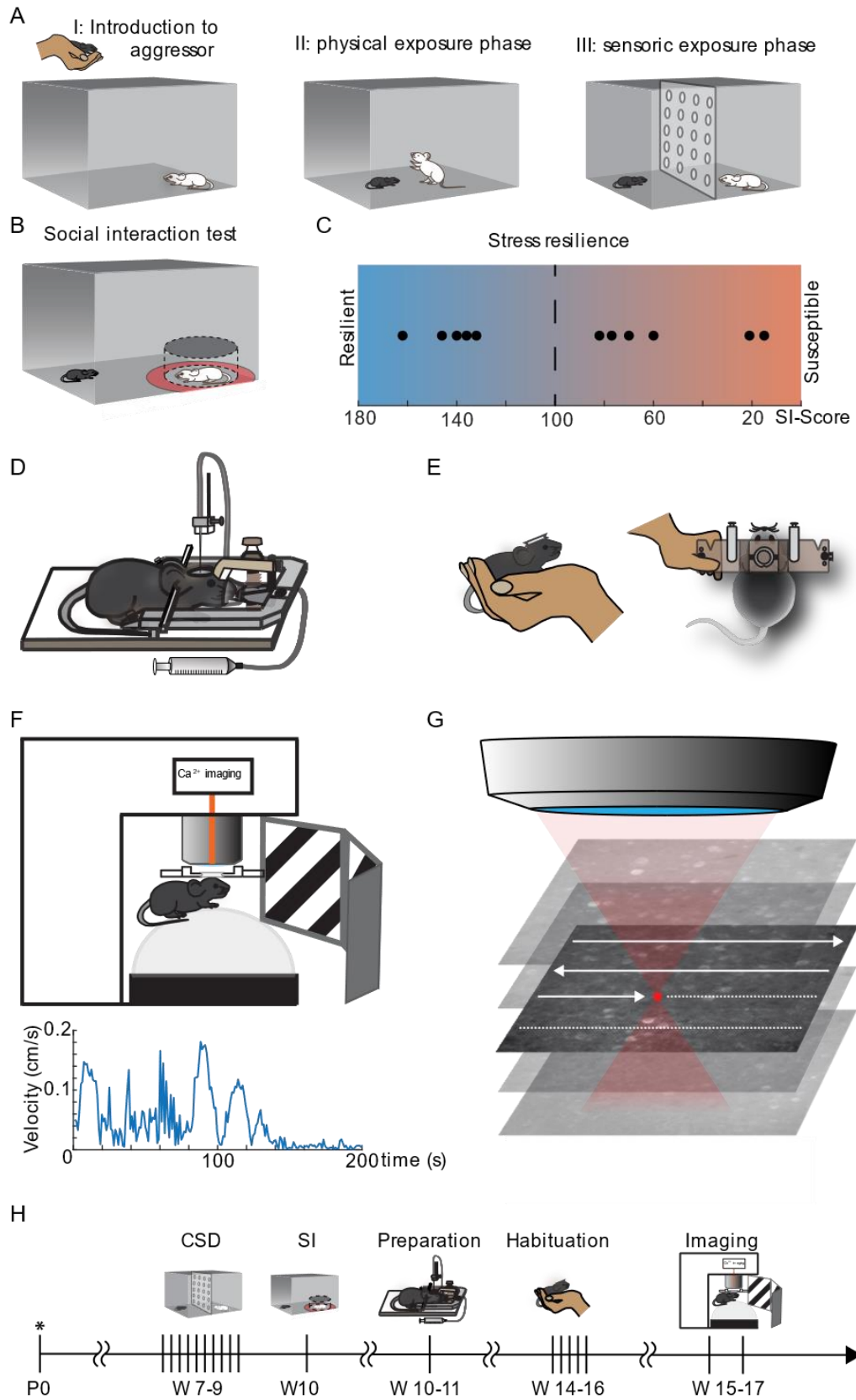


Figure 20: Experimental design of intertwining the chronic social defeat and social interaction paradigms with awake two-photon calcium imaging. (A) Chronic social defeat paradigm in naïve male black6 mice. (A-I) The experimental animal is introduced to an unfamiliar cage containing a retired CD1

breeder, i.e. a physically much stronger mouse. (A-II) Mice have physical contact for 2 min and (A-III) are separated for the following 24 h by a mesh. This procedure is repeated over 10 consecutive days, each day with a novel CD1 male. (B) Social interaction test: The SI score is calculated on the basis of the time an experimental mouse spends in the vicinity of the meshed containment, either in presence or absence of an aggressor mouse. A mouse spending more time in the vicinity of the meshed containment with the aggressor mouse present is considered to be stress resilient (C). Experimental animals are anesthetized and fixed into a stereotaxic frame. An AAV solution encoding for the calcium indicator GCaMP6f is injected into layer II/III of primary visual cortex. (D) Animals are habituated prior the experiments over 5 days to acquaint them with both the experimenter and the head fixation during imaging (E). Awake mice are placed on a spheric polystyrene treadmill during two-photon imaging. A head fixation under the microscope objective ensures stable recordings of neuronal microcircuit activity (F). Fast full field raster scanning in a depth of 150 – 350 μm below pia mater is employed (G). Gantt chart of the implemented paradigm and timepoints (H). The CSD and SI-test were performed by [REDACTED] (Figure by Hendrik Backhaus).

The SI scores of the 11 animals in the study varied between 15 and 162 (Fig 20 C). SI scores were also determined for a control group that did not undergo prior CSD (Table 3).

Animal	SI-Score
R1	162
R2	147
R3	140
R4	136
R5	132
S6	82
S5	78
S4	70
S3	61
S2	22
S1	15
NS1	199
NS2	130
NS3	178

Table 3: Summary of Social Interaction scores of all animals included in this study. R1 – R5: Animals stratified as resilient. S1 – S6: susceptible and NS1 – NS3: non-stressed.

It is important to emphasize that the surgical procedures needed for longitudinal two-photon calcium imaging were carried out after the CSD/SI stages. This was done to prevent any impact on social behavior or interaction from the surgery or the headholder (Fig 20 D). The focus of the study was on recording local cortical microcircuit activity in the primary visual cortex (V1), specifically using the genetically encoded calcium indicator GCaMP6f in excitatory neurons. The animals were given 4 weeks to recover

post-surgery to ensure stable and strong GCaMP6f expression (Guimaraes Backhaus et al., 2021).

Animals were systematically habituated to head fixation and displayed no signs of discomfort during the imaging experiments (Fig 20 E). Functional fast full-field two-photon calcium imaging was performed on awake animals using a spherical polystyrene treadmill to monitor locomotion (Fig 20 F). The setup included a 270° monitor ring for visual stimulation. Fluctuations in intracellular calcium were detected and used as a proxy to identify potentially action-potential related calcium transients in layer II/III of V1 (Fu et al., 2021, Backhaus et al., 2023) (Fig 20 G, H).

3.3.2 Susceptible mice exhibit higher spontaneous activity levels in neuronal microcircuits of the primary visual cortex

In every animal encompassed by this study, the functional patterns of local networks were successfully identified within layers II/III of V1 (Fig 21 A-D). There were no observable differences in terms of cellular density among the animals, and no indications of heightened cellular disintegration were present. The average cell density was 61 ± 11 neurons in the group of resilient animals and 64 ± 5 neurons for susceptible littermates. The excitatory neurons exhibited sparse spontaneous calcium transients, meeting the criteria for putatively action-potential-related events (Guimaraes Backhaus et al., 2021). The average activity rate on a per-neuron basis was quantified, all recorded somata pooled together. Based on this assessment, the animals were categorized into the aforementioned stress-resilient and stress-susceptible groups, considering $n = 237$ somata (R) and $n = 277$ somata (S) respectively, revealing a significant positive shift in cortical microcircuit activity when applying a 2-sided Kolmogorow-Smirnow-Test ($p = 0.0478$, Fig 20 E, F). These findings suggest a correlation between social interaction parameters and spontaneous activity rates within the primary visual cortex.

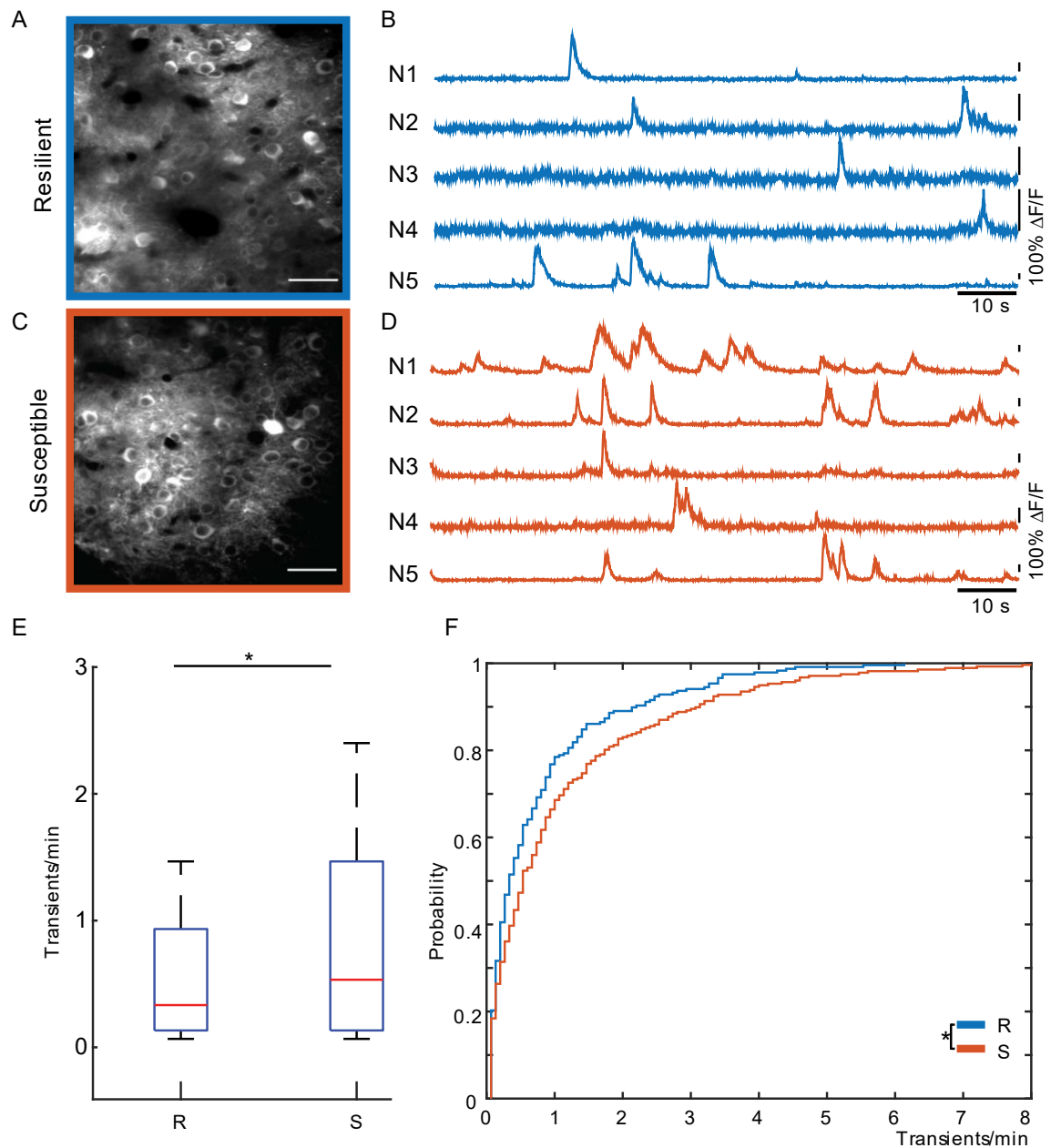


Figure 21: Local network activity in V1 reflects social stress vulnerability. Micrographs of microcircuits in layer II/III of the primary visual cortex, recorded by two-photon microscopy, of a resilient (A) and susceptible (C) animal (Scale bars are 50 μm), and the corresponding intensity traces of somata within the microcircuit (B, D). The average cell density was 61 ± 11 neurons in the group of resilient animals and 64 ± 5 neurons for susceptible littermates. Boxplot of the activity frequency of all recorded somata pooled together in resilient and susceptible groups, considering $n = 237$ somata (R) and $n = 277$ somata (S) respectively (E). A significant difference in the cumulative distribution (F) of activity frequencies is observed (2-sided Kolmogorov-Smirnov-Test, $p = 0.0478$). (Figure by Hendrik Backhaus).

3.3.3 Non-stressed animals exhibit activity dynamics close to the dynamics of susceptible animals

To determine whether the network dynamics in non-stressed animals resemble those of either resilient or susceptible animals, or if they signify a distinct third network state, mice that had not undergone the CSD paradigm were subjected to the SI test. Apart from this alteration, the non-stressed mice underwent the same experimental procedures as their stressed counterparts. The recorded microcircuits (Fig 22 A) displayed a neuronal density strikingly akin to that of the resilient and susceptible groups with an average cell density of 66 ± 7 neurons. As seen in both other conditions, the typical sparse activity of potentially action-potential-related calcium transients was observed (Fig 22 B). The activity frequencies of neurons within microcircuits of non-stressed mice to the outcomes of the treated groups were compared subsequently. Interestingly, the non-stressed group exhibited similarities more aligned with the susceptible group: pooling together all neurons within the non-stressed group led to a consideration of $n = 171$ somata, and employing a 2-sided Kolmogorow-Smirnow-Test revealed a significant difference when compared to the susceptible group. In contrast, the resilient group displayed activity dynamics notably diverging from both the non-stressed ($p = 0.0004$) and susceptible groups (Fig 22 C, D).

The question arose, if these newly identified network properties emerged following stress exposure, or a stratification that was already present in the pre-stressed population was observed? While pre-stressed measurements were not conducted, so as not to impact the CSD/SI paradigm by the presence of the head holder and cranial window, the activity signatures of both the resilient and susceptible groups were pooled. Even when comparing these two stressed groups to the non-stressed controls employing a 2-sided Kolmogorow-Smirnow-Test, a significant difference remains evident ($p = 0.0067$) — both in terms of mean activity state and activity distribution (Fig 22 E, F).

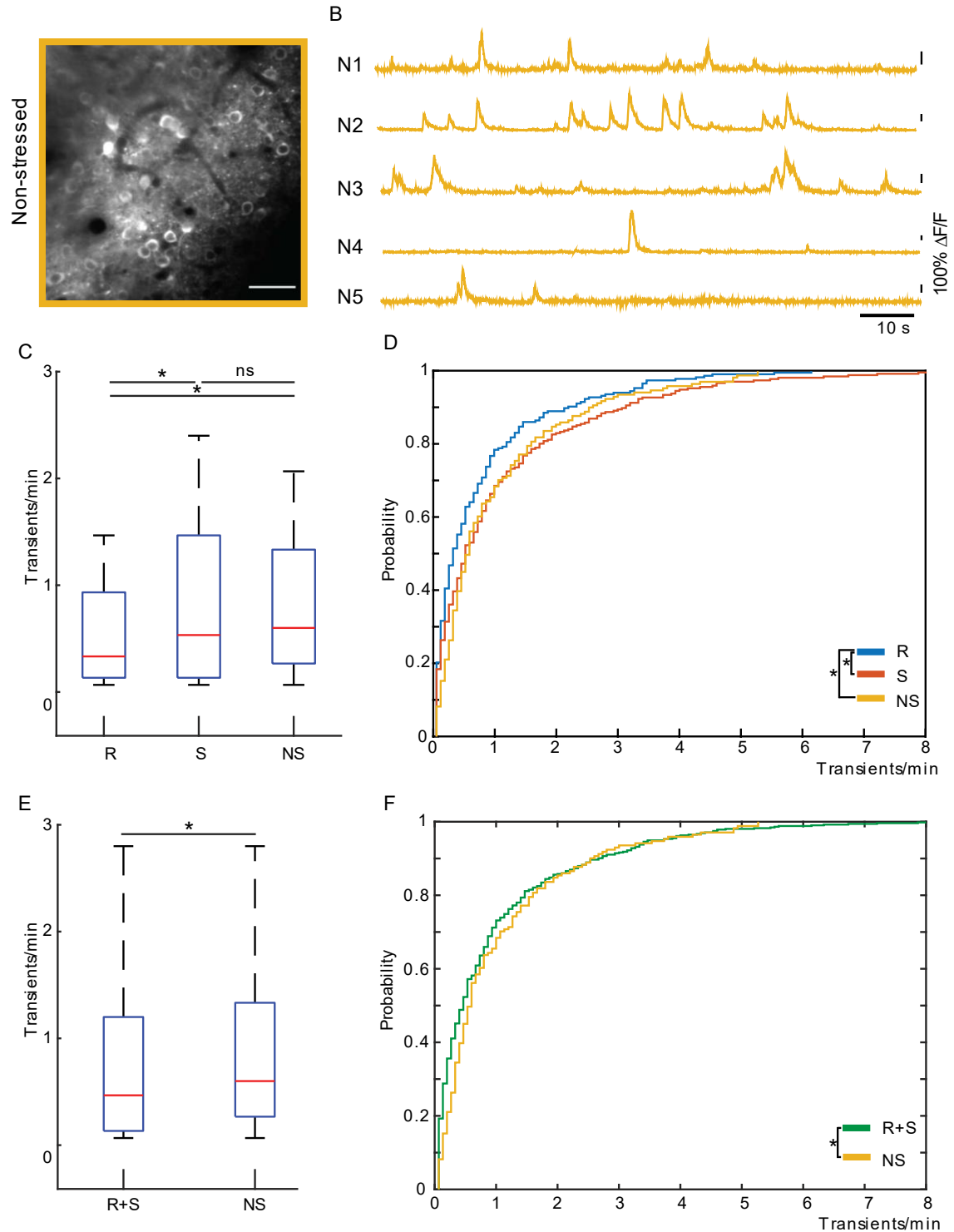


Figure 22: Non-stressed animals show similar activity levels as susceptible animals. Recorded micrograph of a non-stressed animal (Scale bar is 50 μm) (A) and the extracted intensity traces of areas in the field of view containing neuronal somata (B) do not show any morphological difference to the two stressed groups. The average cell density was 66 ± 7 neurons. Boxplots (C) and cumulative distributions (D) of activity frequencies of all somata pooled in a non-stressed group considering $n = 171$ somata show no difference towards the group of susceptible somata but significantly differ to the resilient group (2-sided Kolmogorow-Smirnow-Test, $p = 0.0004$, $n = 171$ somata). Boxplots (E) and cumulative distributions (F) of activity frequencies of all somata of the resilient and susceptible group show a significant difference to the non-stressed group (2-sided Kolmogorow-Smirnow-Test, $p = 0.0067$). (Figure by Hendrik Backhaus).

3.3.4 Resilient microcircuits surpass susceptible and non-stressed microcircuits in the accuracy of the representation of visual afferents

It was further investigated whether the distinct signature of network activity observed in resilient mice is adaptively or maladaptively related to the representation of visual afferents.

To achieve this, both static- and drifting-grating stimulation paradigms were utilized, while simultaneously assessing single cell activity in layer II/III of V1 (Fig 23 A). In light of the findings previously presented, the question emerges whether a modulatory effect following chronic stress exposure leads to a modification of activity patterns in resilient mice. However, to ascertain whether this effect is adaptive or maladaptive, relying solely on stimulus-free network behavior does not yield a conclusive answer.

A noteworthy increase in the proportion of neurons within resilient microcircuits that exhibited finely-tuned responses during drifting grating stimulations, in comparison to susceptible and non-stressed microcircuits, was discovered. In contrast, susceptible and non-stressed microcircuits contained a similar number of identified neurons that displayed an expanded orientation selectivity tuning (Fig 23 H, I).

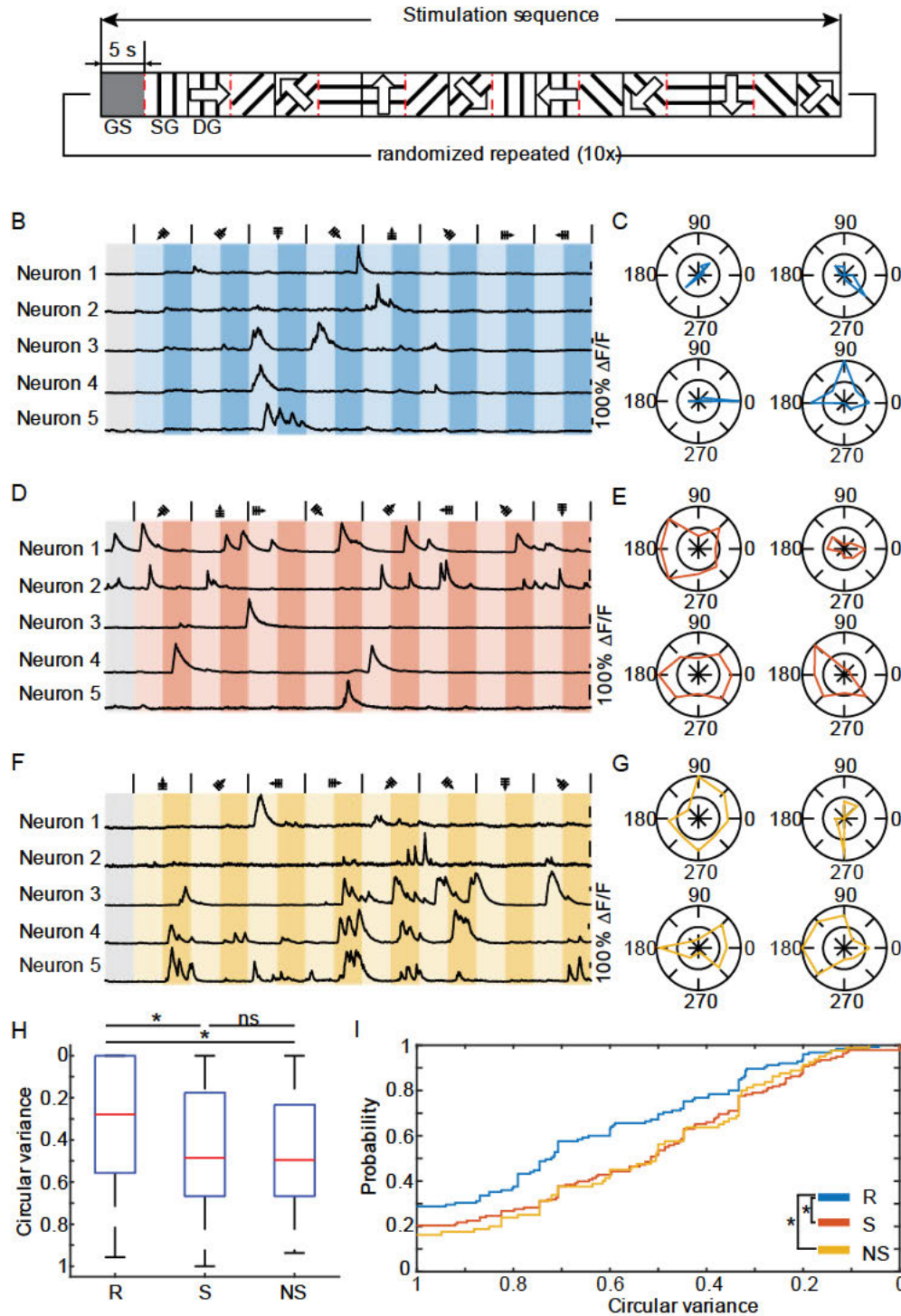


Figure 23: Resilient animals outperform susceptible and non-stressed mice in processing visual afferents. A paradigm of static and drifting grating presentations is used for visual stimulation (A). The stimulation sequence is initialized by a 5 second gray screen presentation, followed by a randomized sequence of 8 grating directions (0, 45, 90, 135, 180, 225, 270 and 315 degree), first displaying a static and then a drifting grating representation, each lasting 5 seconds. The sequence is presented 10 times, each time with a new randomization. Representative intensity traces recorded during visual stimulation of one sequence for a resilient (B), susceptible (D) and non-stressed (F) animal and their corresponding polar plots of neurons response functions (C, E, G). The circular variance of each neuron is calculated and all neurons are pooled into the corresponding 3 groups. Resilient neurons comprise of a significantly higher proportion of well-tuned responses compared to susceptible ($p = 0.0064$) and non-stressed neurons ($p = 0.0001$). No significant difference between susceptible and non-stressed neurons can be detected (2-sided Kolmogorow-Smirnow-Test) (H, I). (Figure by Hendrik Backhaus).

3.3.5 Functional network topology of resilient networks is characterized by efficient small-world architecture

Conducting imaging-based functional recordings, such as two-photon calcium imaging, allows for the examination of network topologies (Rosales Jubal et al., 2021). Functional connectivity between neurons were investigated while simultaneously capturing their individual activity states (Fig 24). In the resilient group, the network displays a pattern of high overall connectivity, characterized by a few densely interconnected hubs. This architectural configuration is typically associated with an efficient network topology in terms of information transfer and processing (Buzsaki and Mizuseki, 2014). On the contrary, susceptible networks exhibit uniform connectivity with diminished connection strengths, along with a significantly different connectivity matrix. This observation may be initially surprising, considering the heightened overall activity state of susceptible networks (Cohen and Kohn, 2011). However, notably, the highly active neurons within these networks appear to have weaker connections. Consequently, the elevated activity of these neurons appears to be counterproductive to the overall efficiency of network function, implying a maladaptive state. The non-stressed control group mirrors the topological organization seen in resilient networks. Employing 2-sided Kolmogorow-Smirnow tests revealed that all conditions underly significantly different statistical distributions. What is more, also in terms of comparison of variances, all conditions differed significantly with exception of the comparison between visually evoked activity between susceptible and non-stressed animals (Table 4).

	Spontaneous activity		Visually evoked activity	
	2- sided KS -Test	Levene's Test	2- sided KS -Test	Levene's Test
R vs. S	5,3611e-24	< 0,001	2.2682e-12	0,037
R vs. NS	4,6864e-41	< 0,001	2.6519e-8	<0,001
S vs. NS	1,2773e-50	0,008	5,8908e-24	0,157

Table 4: Overview of the results of the statistical tests. Kolmogorow-Smirnow tests and differences in variance using Levene's test were performed.

Lastly, network topologies between ongoing and sensory-evoked activity were compared. Strikingly, a close resemblance is observed between these two states. High-efficiency network topologies span both ongoing and task-evoked conditions, offering additional support for the role of ongoing activity in the replay of past sensory experiences (Grun et al., 2022, Luczak et al., 2013, Sugden et al., 2020, Stringer et al., 2019). For an overview of all connectivity maps of stress-resilient, stress-susceptible and non-stressed animals, see Supplement Figures 2 -4.

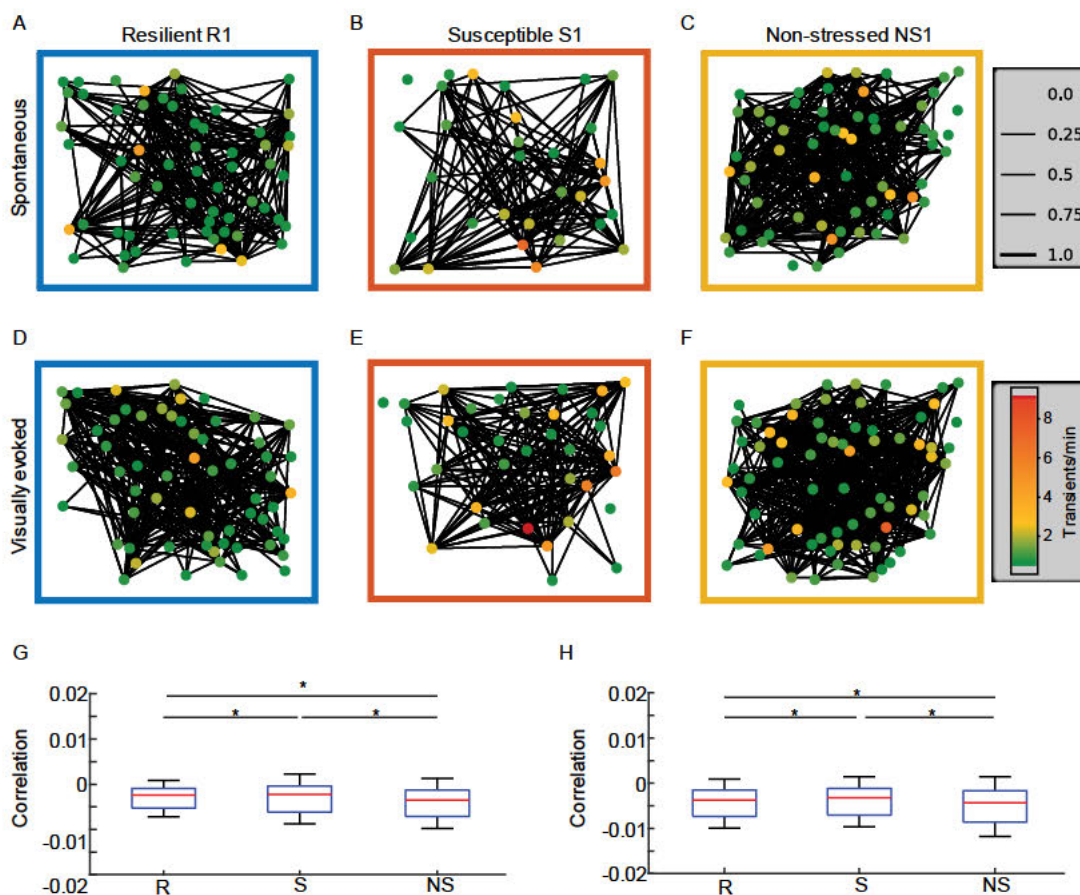


Figure 24: Resilient and non-stressed networks exhibit network topologies efficient for information processing. Connectivity maps of the microcircuit during task free, spontaneous activity of a resilient (A), susceptible (B) and non-stressed (C) animal. A significant difference in distributions of correlation coefficients within neuronal networks of all animals, pooled into the stratified groups of resilient, susceptible and non-stressed are observed (R vs. S: $p = 5,36e-24$, R vs. NS: $p = 4,69e-41$ and S vs. NS: $p = 1,28e-50$, 2-sided Kolmogorow-Smirnow-Test). The unique neuronal correlation distributions are preserved during visual stimulation (R vs. S: $p = 2,27e-12$, R vs. NS: $p = 2,65e-8$, S vs. NS: $p = 5,89e-24$) (D, E, F) Code developed by Nicolas Ruffini. Dots represent the location of somata within the microcircuits and the color reflects the activity state. Lines between dots indicate the strength of correlation for each neuron with each other neuron. Boxplot of all correlation coefficients while ongoing spontaneous activity is assessed (G) and during visual stimulation employing static and drifting grating paradigm (H). (Figure by Hendrik Backhaus).

3.3.6 The stability of systemic resilience mechanisms - a permanent state?

Subsequent measurements of the same microcircuit were conducted one week later in both a resilient and a susceptible mouse. The activity levels of all neurons within an individual that could be co-localized were compared across both measurement time points. Although single neurons demonstrated shifts in their activity rates, the overall activity signature of the microcircuit remained unchanged, regardless of the behavioral consequences of chronic stress exposure (Fig 25). This indicates that the functional architecture remains at least meta-stable.

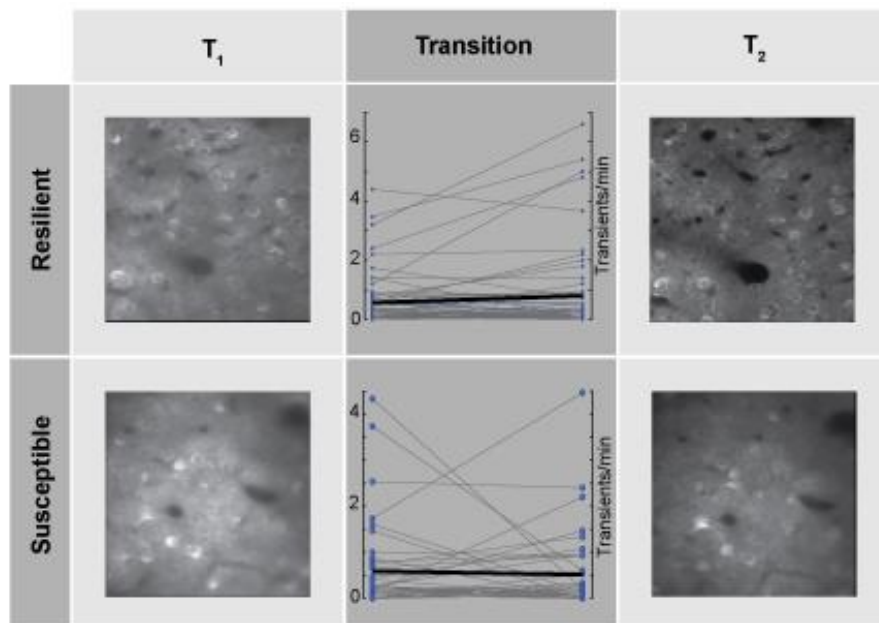


Figure 25: Assessment of the long-term stability of the local network activity. A two-photon micrograph of a resilient and a susceptible animal, each measured at a one-week interval (T₁, T₂). The transition of the activity levels for all neurons that could be identified at both time points indicate shifts in firing frequencies of a subfraction of neurons. The cumulative distributions of all pooled neurons of the respective animal show no significant difference between the two imaging timepoints. (Figure by Hendrik Backhaus).

3.4 How deep can we go? A qualitative comparison of imaging depths in two-photon and three-photon functional calcium imaging

The limitation of two-photon microscopy becomes particularly clear when neuronal networks below cortex layer II/III are to be measured. Although a theoretical penetration depth of up to 500 μm is possible using a two-photon regime (see Introduction Chapter 1.7.2), a maximum imaging depth of up to layer II/III has become established. In the following, the first results of a new system equipped with a light source for three-photon excitation are presented.

3.4.1 Three-photon microscopy enables imaging of neuronal network activity in layer 5 of the cortex

In superficial cortex, ranging at 150 μm below pia mater, two-photon and three-photon

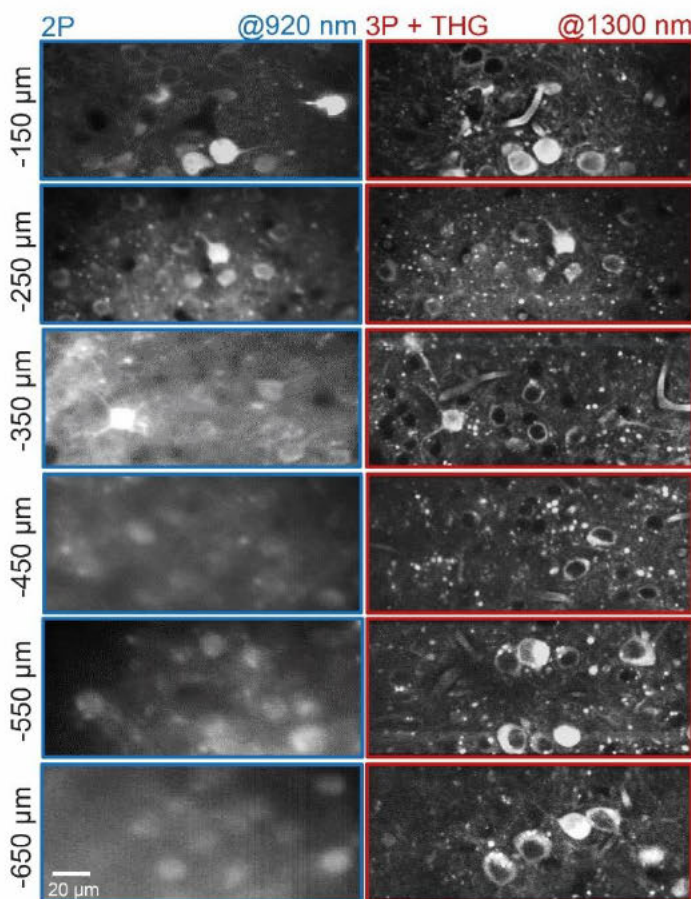


Figure 26: Comparison of imaging qualities in dependence of imaging depth between a two-photon and a three-photon excitation regime. Contrast does not decline with depth under three-photon regime. Example two-photon and three-photon images from 150, 250, 350, 450, 550 and 650 μm below the pial surface of visual cortex. Images collected by [redacted]. Scale bar represents 20 μm .

results were similar in terms of contrast and image quality and neuronal somata were co-localized in both imaging setups (Fig. 26). While the contrast already deteriorates from a penetration depth of 250 μm when using two-photon microscopy, the measurement of the same neurons shows a constant contrast when using the three-photon microscopy system. As expected, the contrast deterioration continues with increasing penetration depth under a

two-photon regime, while measurements using three-photon microscopy show a constant contrast, which allows a clearly differentiable resolution of the neuronal somata to the neuropil even at penetration depths of up to 650 μm . Colocalization of the neuronal somata between two-photon and three-photon microscopy measurements from a penetration depth of 350 μm proves to be challenging, as the contrast reduction when using the two-photon microscopy system already makes it difficult to differentiate between neuronal somata and neuropils. From a penetration depth of 450 μm , colocalization can no longer be performed accurately, which is why the FOVs shown should serve as a qualitative comparison.

3.4.2 The imaging quality using three-photon excitation is comparable to two-photon excitation

The qualitative representation of putatively action potential related functional calcium transients was investigated by measuring a neuronal network at a depth of 250 μm below pia mater in both setups (Fig. 27 A). Both excitation methods enabled the recording of an ensemble of neurons that, labeled with ROIs as functional units, exhibited signal components within the intensity traces expected from putative AP-related calcium transients (Fig. 27 B, C). The density of resolved neuronal somata did not differ between the two excitation methods (three-photon excitation: 878.31 ± 231.79 ; two-photon excitation: 998.1808 ± 20.3591). Neuronal somata in both imaging modalities exhibited the typical signal characteristics that are to be expected when functional calcium transients occur. The frequency of activity did not differ between the two methods (three-photon excitation: 1.43 ± 0.20 ; two-photon excitation: 1.46 ± 0.12), nor was there any difference in the relative number of active neurons (three-photon excitation: 34.02 ± 17.86 ; two-photon excitation: 41.95 ± 5.47).

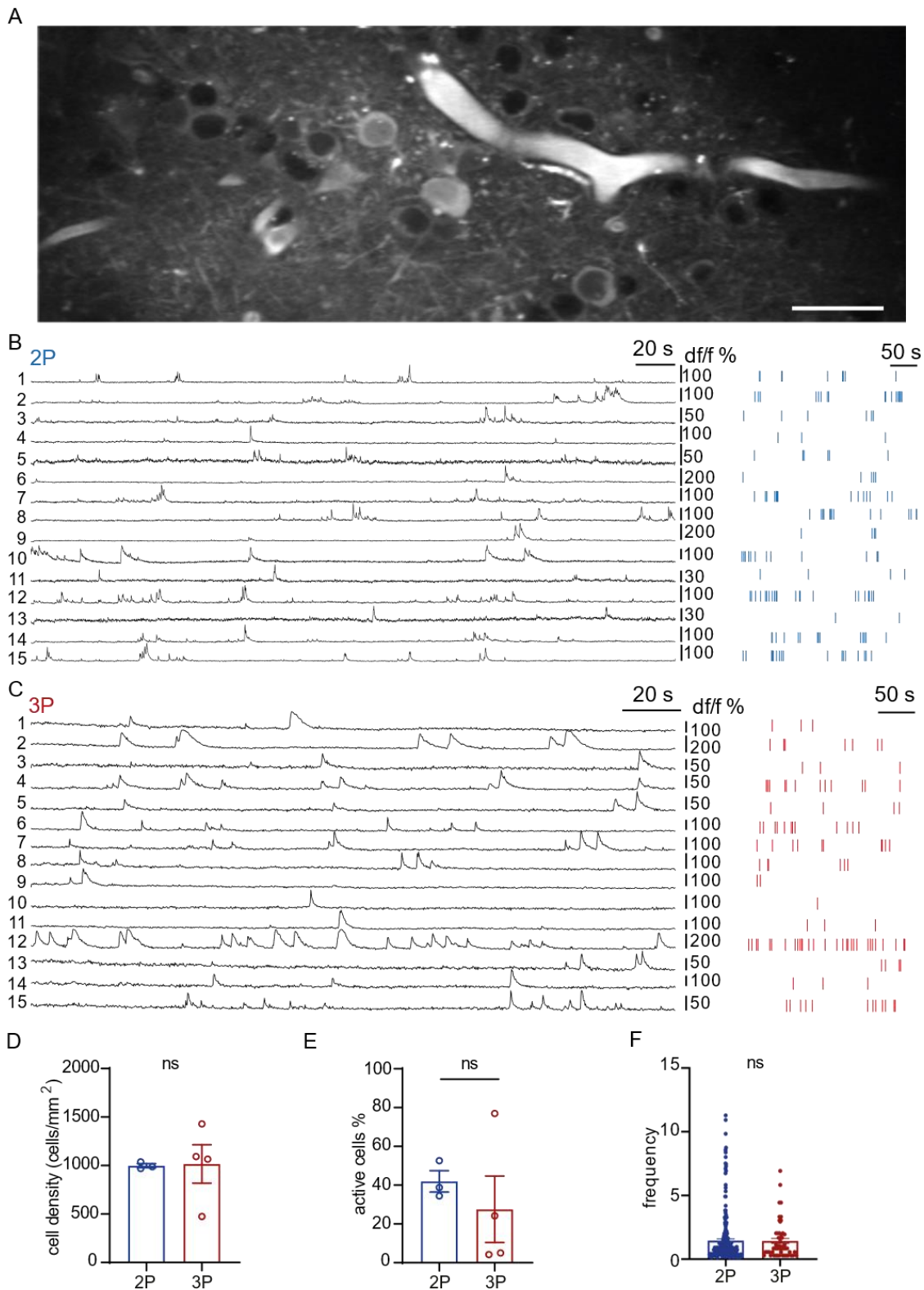


Figure 27: Three-photon imaging is comparable to two-photon imaging in terms of assessment of single cell activity. (A) Micrograph of the recorded neuronal ensemble. Scale bar represents 15 μm . Intensity traces of recorded neurons (left) employing two-photon imaging (B) and three-photon imaging (C) and the corresponding binarized activity trains (right). (D) No difference in cell density of recorded microcircuits is observable. The recorded microcircuits show no difference in the amount of active cells (E) and their activity frequency (F). Error bars indicate standard error of the mean. Figure and analysis by [redacted] (A – C) and [redacted] (D – F).

4. Discussion

4.1 The success of neurophysiological experiments using optical methods relies on an appropriate analysis pipeline

The field of all-optical physiology in neuroscience, which involves concurrent recording and manipulation of individual components within a microcircuit, offers exciting new possibilities (Marshall et al., 2019). Particularly in preclinical rodent models of neurological disorders, these groundbreaking experiments can shed light on how the (dys)function of individual neurons and neuronal ensembles impacts network performance and behavior. Nonetheless, the full potential of all-optical physiology remains largely untapped. There are various reasons for this. Firstly, an ideal opsin for effectively inducing action potentials to mimic physiological inputs' temporal dynamics is still not available, despite significant progress. While efficient two-photon excitation has made substantial strides, efficient two-photon-based inhibition, particularly, is in its early stages (Bovetti et al., 2017). However, the opsin and stimulation methods are only parts of the whole process. This requires to move beyond synthetic, non-physiological stimulation patterns that often trigger unnatural responses due to network hypersynchronization caused by simultaneous activation of multiple neurons. To achieve this, not only neuronal activity needs to be recorded but also activity patterns need to be analyzed in real-time. This will allow to replay and meaningfully modify the endogenous ensemble activity, completing the loop.

In this thesis, crucial aspects of system integration and the fundamental concept of analyzing all-optical functional data were presented. In conclusion, the entire workflow—from capturing raw images to identifying and binarizing events and designing stimulation patterns—needs to shift towards real-time closed-loop execution (Jin et al., 2018). This necessitates fast dedicated hardware. Every component of the system—microscope, optogenetic pattern generator, signal acquisition, and signal computation—must operate in real time. While this is attainable for the microscope, optogenetic pattern generator, and signal acquisition components, achieving it for

event-based signal processing and analysis in real time remains a challenge. Realizing real-time capability for this critical analysis step requires close collaboration between neuroscientists, mathematicians, and (bio)informaticians. Initially, the neurophysiological events of interest need to be meticulously identified and described. For instance, in previous studies on local population state transitions, these events had to be distinguished from a vast array of neurophysiological signal components and characterized in terms of their spatiotemporal dynamics and variability. Subsequently, mathematicians can leverage statistical methods or novel unsupervised machine learning algorithms. The advent of artificial intelligence holds the potential to accelerate analysis routines, traditionally taking weeks or months, to mere seconds or milliseconds (Soltanian-Zadeh et al., 2019, Pnevmatikakis, 2019, Richards et al., 2019).

Collectively, the rapidly advancing field of all-optical physiology for neuronal microcircuits can only flourish within a multidisciplinary framework, reliant on the optimization and integration of each component.

4.2 Single cell activity during SWEs can be grasped by two-photon microscopy

Understanding how information is represented and processed in the mammalian neocortex requires measurements from single-cell dynamics of local microcircuits up to macroscopic whole-brain readouts, enabling to identify spatiotemporal activity patterns in local to global networks of neurons across scales.

During isoflurane induced slow wave activity, calcium transients in layer II/III were rarely observed, even though the slow wave rhythm was detectable in the neuropil, likely reflecting activity from deeper layers. But, if the neurons are active, they are exclusively active in active periods, i.e., the population slow wave event SWE. These results were in line with previous findings of the neuropil being able to serve as an “optical

encephalogram”, representing bulk calcium signals in axonal structures, thus providing a measure of input from deeper cortical layers (Kerr et al., 2005), as SWE originate mainly from layer V (Sanchez-Vives and McCormick, 2000).

4.3 Resilient phenotypes are reflected in their network activity within the visual cortex

In the course of this thesis, an experimental design that integrates awake optical microcircuit imaging with a behavioral paradigm to stratify social stress resilience was introduced, focusing on the effects and outcomes of social stress on visual networks. This exploration unveiled a distinct network phenotype spanning both spontaneous, ongoing activity and stimulus-evoked responses. Clear differentiation emerged between resilient and susceptible animals across nearly all network metrics. Notably, resilient animals exhibited heightened accuracy in representing visual afferents compared to non-stressed animals.

A robust network signature underlies any phenotypic representation, delineating a unique network state (Niell and Stryker, 2010, Speed et al., 2020, Yuste, 2015, Pagan et al., 2016, Henschke et al., 2020, Vaidya and Gordon, 2013, Misic and Sporns, 2016). Depending on the temporal scale and definition of behavioral motives, these distinct states can be subdivided into substates that contribute to specific phenotypic outcomes. For instance, a generalizable network state of motor response could harbor embedded smaller motives. Assigning a singular network state to a particular phenotypic outcome, especially one as broadly termed as social stress resilience, is intricate. Yet, smaller aspects in well-defined brain regions can be observed. Efforts to analyze network dynamics have been undertaken in prefrontal areas involved in decision-making and emotional regulation, such as the HPA axis (Colyn et al., 2019, Xu and Sudhof, 2013, Lopresto et al., 2016, Myers et al., 2014, Banerjee et al., 2017, Abe et al., 2019).

The prevailing notion of brain networks operating in isolation, each performing specified tasks, necessitates revision. Instead, understanding the brain as a tightly interwoven, interconnected network should be embraced (Zatka-Haas et al., 2021, Singer, 2009, Buzsaki and Voroslakos, 2023). Growing evidence suggests that sensory cortical areas are not solely influenced by the behavioral state of the organism (Niell and Stryker, 2010), but they also relay sensory information to other sensory cortices and prefrontal areas beyond the classical visual information processing streams, such as the rostral and ventral streams.

The conventional bottom-up (Britten et al., 1996) and top-down (Nienborg and Cumming, 2009) hypotheses explaining sensory stimulus processing and subsequent decision-making have attributed distinct tasks to specific brain regions. However, in recent years, the concept of singular sensory cortical areas, like the visual cortex, having only one dedicated task has been challenged. Although the primary role of the visual cortex is undeniably processing visual stimuli, evidence suggests an intricate exchange of information between various cortico-cortical and sub-cortical regions before and during action execution in response to external stimuli, with cortical regions also contributing to decision-making, albeit to a lesser extent (Zatka-Haas et al., 2021).

In the context of social stress resilience, sensory cortical areas play a vital role, especially concerning several aspects of resilience. One crucial aspect is sensory discrimination. Animals, including humans, with better sensory context identification and discrimination may be more adept at distinguishing contexts associated with prior social stressors from non-threatening environments. Visual parameter spaces, which encompass the visual environment, are crucial in this regard. Visual afferents are initially represented in the primary visual cortex along the visual pathway. Within this cortex, particularly layers II/III are highly interconnected, responsible for representing, computing, and disseminating the visual parameter space. The accuracy of this parameter space's encoding can be assessed by determining the precision of tuning

for specific movements, such as orientation tuning. This parameter is highly sensitive to early neurodegenerative impacts and forms the basis for our inquiry. This thesis examined whether socially resilient animals might possess a heightened ability to map the visual parameter space. Remarkably, the results demonstrate that resilient animals achieve a more precise representation of the external visual world. This enhanced representation subsequently informs higher-order circuits, which in turn differentially affect the phenotypic response. Particularly within the realm of stress resilience, enhanced discrimination ability could constitute a resilience mechanism (Tran et al., 2016, Sep et al., 2019, Banerjee et al., 2017, Krueger and Sangha, 2021, Lopresto et al., 2016).

While it cannot be definitively determined whether this performance-enhancing network state is due to the social stressor or was already present prior to stress exposure, the identification of an altered network state in both resilient and susceptible animals suggests network plasticity. Resilient animals exhibit a network that is more capable of accurately perceiving the visual world, a pivotal resilience mechanism.

The reflection of social stress resilience within primary sensory cortices carries implications not only for the understanding of social stress resilience as a brain-wide adaptive outcome, but also for informing intervention strategies. A network representation of social stress resilience, applicable across species, can overcome translational challenges. Concepts like training or enhancing sensory discrimination, which render networks more resilient, could prove to be cross-species strategies.

4.4 What comes first? The chicken or the egg?

Despite the differences found between susceptible and resilient animals on group level, the larger inter-individual variability within the groups currently prevents single-subject prediction based on the network activity alone. This variability underscores the complexity of stress resilience and suggests that individual differences may play a significant role in shaping neuronal responses to stress (for an overview of spontaneous network activity per animal, see Supplement Figure 1).

Understanding the factors contributing to this variability could provide valuable insights into the mechanisms underlying stress resilience and vulnerability, potentially paving the way for more targeted interventions or treatments aimed at promoting resilience in the face of stress.

It's important to acknowledge that the small sample size employed in this study may present limitations in robustly assessing the outcomes. Given the proposed variations in resilience mechanisms among individuals, the modest sample size may not adequately capture the full spectrum of responses. To mitigate this limitation and enhance the reliability of the findings, future studies could benefit from significantly increasing the sample size (n) to encompass a broader range of individuals. By doing so, the statistical power of the analyses can be improved and a more comprehensive understanding of the neuronal mechanisms underlying stress resilience can be achieved.

Additionally, it's worth noting that the experimental design utilized a relatively unspecific and context-free stimulus, employing static and drifting grating stimuli. While this approach is valuable for assessing fundamental baseline functionality, it may not fully capture the dynamics of neuronal networks under conditions of stress or adversity. To address this limitation and better simulate real-world stressors, I propose an experimental paradigm where visual grating stimulation is paired with an olfactory

stimulus. For instance, introducing urine extracts from a CD1 male during the experiment could serve as a relevant stressor. By incorporating such a stimulus, it can be investigated how neuronal networks respond in the presence of a stress-inducing cue, providing valuable insights into the adaptive mechanisms underlying stress resilience.

4.5 Examining cortical micronetworks by three-photon microscopy – a game changer?

The advent of functional three-photon microscopy for calcium imaging represents a significant advance in the study of neuronal activity deep within the brain. With its extraordinary depth of penetration, three-photon imaging surpasses the limits of its predecessor, allowing researchers to visualize neuronal dynamics in previously inaccessible regions such as the hippocampus (Horton et al., 2013, Wang et al., 2018, Streich et al., 2021, Ouzounov et al., 2017). When investigating neuronal networks *in vivo*, two-photon microscopy is mainly applied in the neocortex, as the penetration depth is limited to around 500 μm . Beyond 500 μm , the out of focus intensity increases and results in a blurry image, impeding the identification of neuronal somata as regions of interest or, in the worst case, making it impossible. When neuronal microcircuits in deeper brain regions shall be examined, such as the hippocampus, researchers overcome the imaging depth limitations by removing parts of the neocortex and either implant a canula, glass plug or GRIN lens (Velasco and Levene, 2014, Jung and Schnitzer, 2003, Levene et al., 2004, Barretto et al., 2011) to enable data collection employing a two-photon approach. However, these methods result in an invasive preparation procedure, ultimately destroying the natural internal environment of a functioning brain. The reduction of out of focus excitation as well as the reduced scattering of longer wavelengths enables the method of three-photon excitation to open

up new insights into the intricacies of neural circuits and their functions, and could unravel secrets previously beyond our reach.

However, despite its groundbreaking capabilities, three-photon imaging is not without its drawbacks, especially when compared to established two-photon imaging. One notable limitation is the reduced field of view offered by three-photon microscopy. This smaller spatial coverage leads to a reduced ability to resolve neuronal somata within the imaging field. As a result, the assessment of neuronal networks becomes a real challenge as only a fraction of the neuronal population is captured in each image, limiting the ability to comprehensively analyze network dynamics and interactions. Several research groups addressed this limitation and developed solutions to increase the resolved field of view by employing adaptive optics (AO), which is used to measure and correct the distortion of an excitation wavefront that is scattered in tissue (Rodriguez et al., 2021, Streich et al., 2021, Qin et al., 2022, Sinefeld et al., 2022). This two-step approach firstly requires a determination of the wavefront, where either direct or indirect methods can be applied. Afterwards, a phase modulation device such as a spatial light modulator (SLM) or deformable mirror (DM) can be used to correct the specimen-induced aberrations. As an example for an indirect method, Streich et al presented a three-photon microscope equipped with a continuous membrane DM and a modal based AO optimization with automatic shift correction. Furthermore, the system comprises of a field-programmable gate array (FPGA) which synchronizes the scanning mirrors with an echo-cardiogram (ECG), enabling the observation of the cardiac cycle in real time and pausing the scanning during peaks of the ECG. Thus, motion artifacts caused by the heartbeat can be minimized and the acquisition of stable temporal images is improved. The axial resolution reached by the system is stated with 3.1 μm in the cortex at a depth of 653 μm and 7.9 μm axial resolution when imaging the hippocampus at a depth of 1054 μm . Similar approaches were developed by the groups of Chris Xu (Sinefeld et al., 2022) and Na Ji (Rodriguez et al., 2021) reaching similar

results. However, to acquire a frame with this method typically requires 20 – 30 s which is a far too slow frame rate for functional calcium imaging applications. This leads to a further circumstance that currently limits further expansion of the use of three-photon microscopy, especially for functional imaging: while three-photon imaging is excellent for examining deep brain structures, its temporal resolution lags behind that of two-photon imaging. With a frame rate of 5 Hz, three-photon microscopy is inferior compared to the fast temporal sampling possible with two-photon techniques, which typically achieve frame rates of 30 Hz. This discrepancy in temporal resolution is a significant limitation, especially when capturing fast neuronal events such as single action potentials. Despite advances in calcium indicators aimed at improving temporal kinetics and signal fidelity, the inherent limitations of a 5 Hz frame rate led to uncertainties in the accurate resolution of these transient events. To overcome this issue, Li et al introduced an adaptive excitation source (AES) and used it for high-speed neuroimaging in the awake mouse. Initially, a structural image of the region of interest is acquired by employing a uniform pulse train, resolving high-resolution image where all pixels are equally excited by the laser source. The high-resolution image is used to label all neuronal somata as regions of interest which are converted to a digital binary sequence in the next step. The matrix, where a neuronal soma is labeled as 1 and all remaining structures as 0, such as blood vessels or neuropil, is used by an arbitrary waveform generator to drive a fiber-integrated electro-optic modulator (EOM), encoding the ROI position into a laser pulse pattern. By ensuring an accurate synchronization of the scanners and the laser source, an increase of the imaging speed is possible while omitting the collection of information considered unnecessary. It has been shown, that a three-photon microscope equipped with an AES system can achieve a representation of a 620 x 620 μm^2 FOV at a resolution of 512 x 512 pixels with a temporal resolution of 30 Hz, recorded 750 μm below dura mater. Even if the performance is on a par with that of a two-photon microscope, there are inevitable disadvantages of this method: As

already elaborated in a previous chapter of this thesis, a random-access measurement, which is required by the system, represents a considerable disadvantage in the subsequent analysis of the recorded data sets, as the initial motion correction of the data is rendered more difficult.

To improve the frame rate without omitting parts of the FOV, temporal focusing (TF) can render a promising solution (Toda et al., 2017, Escobet-Montalban et al., 2018): a diffusive or dispersive optical element is positioned in a plane conjugate to the objective focal plane, resulting in a dispersion and reduction of absorption in out-of-focus planes. The emitted fluorescence by the excited FOV, comprising the neuronal somata of interest, is collected by an epi-detection and a camera. Thereby, the temporal resolution of excitation is improved and higher imaging frame rates can be applied, but at the cost of a reduction of imaging depth. Toda et al showed a successful sectioning capability and improved TF from 2.1 to 1.6 μm . However, this method is also incomparable with the performance of currently available two photon microscopes (Toda et al., 2017).

To ultimately lift the performance of three photon microscopes to a comparable level of two photon microscopes, the undeniable bottleneck is the repetition rate of commercially available lasers while ensuring temporal and spatial emission of light pulses and their user-friendly application in a neuroscience-based laboratory. A wide variety of lasers used in two photon microscopy comprises of repetition rates of up to 80 MHz at a pulse width of 140 fs while covering a wide range of applicable wavelengths (Chameleon Ultra II, Coherent). On the other hand, commercially available light sources capable of three photon excitation reach repetition rates of up to 4 MHz at a pulse width of < 50 fs but at a fixed wavelength (Monaco 1300, Coherent) or, as an example of a tunable light source, reach repetition rates of 2 MHz at a pulse width of 100 – 300 fs with a possible tuning bandwidth between 1050 – 2500 nm (Carbide, LightConversion). The low repetition rate requires the use of galvanic mirrors for raster scanning, drastically limiting the achieved frame rate. Only the development of laser sources

emitting light pulses in the wavelengths required for three photon excitation with a repetition rate comparable to lasers used in two photon microscopy can lead to the application of fast resonant mirrors for imaging, enabling for image acquisitions similar to established two photon microscopes while exploiting the benefits of deeper tissue penetration.

Additionally, it is noteworthy to mention that advancements in imaging technology by other research groups have yielded systems capable of achieving even larger field of views and higher frame rates. Some systems developed by these groups boast field of views of up to 350 μm^2 while maintaining frame rates of 8 Hz (Takasaki et al., 2020). This represents a significant improvement over the current limitations of three-photon imaging, offering a wider spatial coverage and slightly improved temporal resolution. Such developments highlight the ongoing efforts within the scientific community to push the boundaries of imaging capabilities, paving the way for more comprehensive and detailed investigations into neural activity and circuit dynamics.

In essence, while three-photon functional calcium imaging microscopy offers exceptional depth penetration and the potential to uncover hidden neural dynamics, it must contend with trade-offs in spatial coverage and temporal resolution compared to its two-photon counterpart. As research continues to push the boundaries of calcium imaging technology and signal processing techniques, addressing these limitations will be crucial in unlocking the full potential of three-photon imaging for unraveling the complexities of the brain's inner workings.

“So once you do know what the question actually is, you'll know what the answer means.”

— Douglas Adams.

6. References

- ABE, R., OKADA, S., NAKAYAMA, R., IKEGAYA, Y. & SASAKI, T. 2019. Social defeat stress causes selective attenuation of neuronal activity in the ventromedial prefrontal cortex. *Sci Rep*, 9, 9447.
- ACHERMANN, P. & BORBELY, A. A. 1997. Low-frequency (< 1 Hz) oscillations in the human sleep electroencephalogram. *Neuroscience*, 81, 213-22.
- ACKMAN, J. B., BURBRIDGE, T. J. & CRAIR, M. C. 2012. Retinal waves coordinate patterned activity throughout the developing visual system. *Nature*, 490, 219-25.
- ADELSBERGER, H., GRIENBERGER, C., STROH, A. & KONNERTH, A. 2014. In Vivo Calcium Recordings and Channelrhodopsin-2 Activation through an Optical Fiber. *Cold Spring Harb Protoc*, 2014, pdb prot084145.
- AHMADLOU, M. & HEIMEL, J. A. 2015. Preference for concentric orientations in the mouse superior colliculus. *Nat Commun*, 6, 6773.
- AL-JUBOORI, S. I., DONDZILLO, A., STUBBLEFIELD, E. A., FELSEN, G., LEI, T. C. & KLUG, A. 2013. Light scattering properties vary across different regions of the adult mouse brain. *PLoS One*, 8, e67626.
- APPLEBURY, M. L., ANTOCH, M. P., BAXTER, L. C., CHUN, L. L., FALK, J. D., FARHANGFAR, F., KAGE, K., KRZYSTOLIK, M. G., LYASS, L. A. & ROBBINS, J. T. 2000. The murine cone photoreceptor: a single cone type expresses both S and M opsins with retinal spatial patterning. *Neuron*, 27, 513-23.
- ARAVANIS, A. M., WANG, L. P., ZHANG, F., MELTZER, L. A., MOGRI, M. Z., SCHNEIDER, M. B. & DEISSEROTH, K. 2007. An optical neural interface: in vivo control of rodent motor cortex with integrated fiberoptic and optogenetic technology. *J. Neural Eng*, 4, S143-S156.
- ARNOUX, I., WILLAM, M., GRIESCHE, N., KRUMMEICH, J., WATARI, H., OFFERMANN, N., WEBER, S., NARAYAN DEY, P., CHEN, C., MONTEIRO, O., BUETTNER, S., MEYER, K., BANO, D., RADYUSHKIN, K., LANGSTON, R., LAMBERT, J. J., WANKER, E., METHNER, A., KRAUSS, S., SCHWEIGER, S. & STROH, A. 2018. Metformin reverses early cortical network dysfunction and behavior changes in Huntington's disease. *Elife*, 7.
- ATANAS, A. A., KIM, J., WANG, Z., BUENO, E., BECKER, M., KANG, D., PARK, J., KRAMER, T. S., WAN, F. K., BASKOYLU, S., DAG, U., KALOGEROPOULOU, E., GOMES, M. A., ESTREM, C., COHEN, N., MANSINGHKA, V. K. & FLAVELL, S. W. 2023. Brain-wide representations of behavior spanning multiple timescales and states in *C. elegans*. *Cell*, 186, 4134-4151 e31.
- ATTARDO, A., FITZGERALD, J. E. & SCHNITZER, M. J. 2015. Impermanence of dendritic spines in live adult CA1 hippocampus. *Nature*, 523, 592-6.
- AYASH, S., SCHMITT, U. & MULLER, M. B. 2020. Chronic social defeat-induced social avoidance as a proxy of stress resilience in mice involves conditioned learning. *J Psychiatr Res*, 120, 64-71.
- AZZINNARI, D., SIGRIST, H., STAEHLI, S., PALME, R., HILDEBRANDT, T., LEPARC, G., HENGERER, B., SEIFRITZ, E. & PRYCE, C. R. 2014. Mouse social stress induces increased fear

- conditioning, helplessness and fatigue to physical challenge together with markers of altered immune and dopamine function. *Neuropharmacology*, 85, 328-41.
- BACKHAUS, H., RUFFINI, N., WIERCZEIKO, A. & STROH, A. 2023. An All-Optical Physiology Pipeline Toward Highly Specific and Artifact-Free Circuit Mapping. *All-Optical Methods to Study Neuronal Function*.
- BADEN, T., BERENS, P., BETHGE, M. & EULER, T. 2013. Spikes in mammalian bipolar cells support temporal layering of the inner retina. *Curr Biol*, 23, 48-52.
- BADEN, T., BERENS, P., FRANKE, K., ROMAN ROSON, M., BETHGE, M. & EULER, T. 2016. The functional diversity of retinal ganglion cells in the mouse. *Nature*, 529, 345-50.
- BANERJEE, S. B., MORRISON, F. G. & RESSLER, K. J. 2017. Genetic approaches for the study of PTSD: Advances and challenges. *Neurosci Lett*, 649, 139-146.
- BARRETTO, R. P., KO, T. H., JUNG, J. C., WANG, T. J., CAPPAS, G., WATERS, A. C., ZIV, Y., ATTARDO, A., RECHT, L. & SCHNITZER, M. J. 2011. Time-lapse imaging of disease progression in deep brain areas using fluorescence microendoscopy. *Nat Med*, 17, 223-8.
- BAYM, G. 2018. *Lectures on Quantum Mechanics*.
- BERRIDGE, M. J. 1998. Neuronal calcium signaling. *Neuron*, 21, 13-26.
- BERRIDGE, M. J., BOOTMAN, M. D. & RODERICK, H. L. 2003. Calcium signalling: dynamics, homeostasis and remodelling. *Nat Rev Mol Cell Biol*, 4, 517-29.
- BERTON, O., MCCLUNG, C. A., DILEONE, R. J., KRISHNAN, V., RENTHAL, W., RUSSO, S. J., GRAHAM, D., TSANKOVA, N. M., BOLANOS, C. A., RIOS, M., MONTEGGIA, L. M., SELF, D. W. & NESTLER, E. J. 2006. Essential role of BDNF in the mesolimbic dopamine pathway in social defeat stress. *Science*, 311, 864-8.
- BINDER, E. B., BRADLEY, R. G., LIU, W., EPSTEIN, M. P., DEVEAU, T. C., MERCER, K. B., TANG, Y., GILLESPIE, C. F., HEIM, C. M., NEMEROFF, C. B., SCHWARTZ, A. C., CUBELLS, J. F. & RESSLER, K. J. 2008. Association of FKBP5 polymorphisms and childhood abuse with risk of posttraumatic stress disorder symptoms in adults. *JAMA*, 299, 1291-305.
- BOIROUX, D., OKE, Y., MIWAKEICHI, F. & OKU, Y. 2014. Pixel timing correction in time-lapsed calcium imaging using point scanning microscopy. *J Neurosci Methods*, 237, 60-8.
- BONANNO, G. A., ROMERO, S. A. & KLEIN, S. I. 2015. The Temporal Elements of Psychological Resilience: An Integrative Framework for the Study of Individuals, Families, and Communities. *Psychological Inquiry*, 26, 139-169.
- BOVETTI, S., MORETTI, C., ZUCCA, S., DAL MASCHIO, M., BONIFAZI, P. & FELLIN, T. 2017. Simultaneous high-speed imaging and optogenetic inhibition in the intact mouse brain. *Sci Rep*, 7, 40041.
- BOYDEN, E. S., ZHANG, F., BAMBERG, E., NAGEL, G. & DEISSEROTH, K. 2005. Millisecond-timescale, genetically targeted optical control of neural activity. *Nat. Neurosci.*, 8, 1263-1268.
- BREAKSPEAR, M. 2017. Dynamic models of large-scale brain activity. *Nat Neurosci*, 20, 340-352.
- BRIGGMAN, K. L., HELMSTAEDTER, M. & DENK, W. 2011. Wiring specificity in the direction-selectivity circuit of the retina. *Nature*, 471, 183-8.

- BRITTEN, K. H., NEWSOME, W. T., SHADLEN, M. N., CELEBRINI, S. & MOVSHON, J. A. 1996. A relationship between behavioral choice and the visual responses of neurons in macaque MT. *Vis Neurosci*, 13, 87-100.
- BUZSAKI, G., LOGOTHETIS, N. & SINGER, W. 2013. Scaling brain size, keeping timing: evolutionary preservation of brain rhythms. *Neuron*, 80, 751-64.
- BUZSAKI, G. & MIZUSEKI, K. 2014. The log-dynamic brain: how skewed distributions affect network operations. *Nat Rev Neurosci*, 15, 264-78.
- BUZSAKI, G. & VOROSLAKOS, M. 2023. Brain rhythms have come of age. *Neuron*, 111, 922-926.
- CARDIN, J. A., CARLEN, M., MELETIS, K., KNOBLICH, U., ZHANG, F., DEISSEROTH, K., TSAI, L. H. & MOORE, C. I. 2010. Targeted optogenetic stimulation and recording of neurons in vivo using cell-type-specific expression of Channelrhodopsin-2. *Nat. Protoc.*, 5, 247-254.
- CARRILLO-REID, L., YANG, W., BANDO, Y., PETERKA, D. S. & YUSTE, R. 2016. Imprinting and recalling cortical ensembles. *Science*, 353, 691-4.
- CAVINESS, V. S., JR. 1975. Architectonic map of neocortex of the normal mouse. *J Comp Neurol*, 164, 247-63.
- CHEN, I. W., RONZITTI, E., LEE, B. R., DAIGLE, T. L., DALKARA, D., ZENG, H., EMILIANI, V. & PAPAGIAKOUMOU, E. 2019. In Vivo Submillisecond Two-Photon Optogenetics with Temporally Focused Patterned Light. *J Neurosci*, 39, 3484-3497.
- CHEN, T. W., LI, N., DAIE, K. & SVOBODA, K. 2017. A Map of Anticipatory Activity in Mouse Motor Cortex. *Neuron*, 94, 866-879 e4.
- CHEN, T. W., WARDILL, T. J., SUN, Y., PULVER, S. R., RENNINGER, S. L., BAOHAN, A., SCHREITER, E. R., KERR, R. A., ORGER, M. B., JAYARAMAN, V., LOOGER, L. L., SVOBODA, K. & KIM, D. S. 2013a. Ultrasensitive fluorescent proteins for imaging neuronal activity. *Nature*, 499, 295-300.
- CHEN, X., LEISCHNER, U., VARGA, Z., JIA, H., DECA, D., ROCHEFORT, N. L. & KONNERTH, A. 2012. LOTOS-based two-photon calcium imaging of dendritic spines in vivo. *Nat Protoc*, 7, 1818-29.
- CHEN, X., ROCHEFORT, N. L., SAKMANN, B. & KONNERTH, A. 2013b. Reactivation of the same synapses during spontaneous up states and sensory stimuli. *Cell Rep*, 4, 31-9.
- CHENG, L. C., HORTON, N. G., WANG, K., CHEN, S. J. & XU, C. 2014. Measurements of multiphoton action cross sections for multiphoton microscopy. *Biomed Opt Express*, 5, 3427-33.
- CHOW, B. Y., HAN, X., DOBRY, A. S., QIAN, X., CHUONG, A. S., LI, M., HENNINGER, M. A., BELFORT, G. M., LIN, Y., MONAHAN, P. E. & BOYDEN, E. S. 2010. High-performance genetically targetable optical neural silencing by light-driven proton pumps. *Nature*, 463, 98-102.
- COHEN, M. R. & KOHN, A. 2011. Measuring and interpreting neuronal correlations. *Nat Neurosci*, 14, 811-9.
- COLYN, L., VENZALA, E., MARCO, S., PEREZ-OTANO, I. & TORDERA, R. M. 2019. Chronic social defeat stress induces sustained synaptic structural changes in the prefrontal cortex and amygdala. *Behav Brain Res*, 373, 112079.

- COMPTE, A., REIG, R., DESCALZO, V. F., HARVEY, M. A., PUCCINI, G. D. & SANCHEZ-VIVES, M. V. 2008. Spontaneous high-frequency (10-80 Hz) oscillations during up states in the cerebral cortex in vitro. *J. Neurosci.*, 28, 13828-13844.
- CROCHET, S. & PETERSEN, C. C. 2006. Correlating whisker behavior with membrane potential in barrel cortex of awake mice. *Nat Neurosci*, 9, 608-10.
- DE BONO, M. & MARICQ, A. V. 2005. Neuronal substrates of complex behaviors in *C. elegans*. *Annu Rev Neurosci*, 28, 451-501.
- DECO, G. & JIRSA, V. K. 2012. Ongoing cortical activity at rest: criticality, multistability, and ghost attractors. *J Neurosci*, 32, 3366-75.
- DEISSEROTH, K. 2015. Optogenetics: 10 years of microbial opsins in neuroscience. *Nat Neurosci*, 18, 1213-25.
- DENK, W., STRICKLER, J. H. & WEBB, W. W. 1990. Two-photon laser scanning fluorescence microscopy. *Science*, 248, 73-6.
- DESTEXHE, A., HUGHES, S. W., RUDOLPH, M. & CRUNELLI, V. 2007. Are corticothalamic 'up' states fragments of wakefulness? *Trends Neurosci*, 30, 334-42.
- DHANDE, O. S., ESTEVEZ, M. E., QUATTROCHI, L. E., EL-DANAF, R. N., NGUYEN, P. L., BERSON, D. M. & HUBERMAN, A. D. 2013. Genetic dissection of retinal inputs to brainstem nuclei controlling image stabilization. *J Neurosci*, 33, 17797-813.
- DOMBECK, D. A., HARVEY, C. D., TIAN, L., LOOGER, L. L. & TANK, D. W. 2010. Functional imaging of hippocampal place cells at cellular resolution during virtual navigation. *Nat. Neurosci.*, 13, 1433-1440.
- DOMBECK, D. A., KHABBAZ, A. N., COLLMAN, F., ADELMAN, T. L. & TANK, D. W. 2007. Imaging large-scale neural activity with cellular resolution in awake, mobile mice. *Neuron*, 56, 43-57.
- DOMINGUEZ-FERNANDEZ, C., EGIGUREN-ORTIZ, J., RAZQUIN, J., GOMEZ-GALAN, M., DE LAS HERAS-GARCIA, L., PAREDES-RODRIGUEZ, E., ASTIGARRAGA, E., MIGUELEZ, C. & BARREDA-GOMEZ, G. 2023. Review of Technological Challenges in Personalised Medicine and Early Diagnosis of Neurodegenerative Disorders. *Int J Mol Sci*, 24.
- DOMSCHKE, K., DANNLOWSKI, U., HOHOFF, C., OHRMANN, P., BAUER, J., KUGEL, H., ZWANZGER, P., HEINDEL, W., DECKERT, J., AROLT, V., SUSLOW, T. & BAUNE, B. T. 2010. Neuropeptide Y (NPY) gene: Impact on emotional processing and treatment response in anxious depression. *Eur Neuropsychopharmacol*, 20, 301-9.
- DOROSZKIEWICZ, J., GROBLEWSKA, M. & MROCZKO, B. 2022. Molecular Biomarkers and Their Implications for the Early Diagnosis of Selected Neurodegenerative Diseases. *Int J Mol Sci*, 23.
- DUBBS, A., GUEVARA, J. & YUSTE, R. 2016. moco: Fast Motion Correction for Calcium Imaging. *Front Neuroinform*, 10, 6.
- DUCHEN, M. R. 1999. Contributions of mitochondria to animal physiology: from homeostatic sensor to calcium signalling and cell death. *J Physiol*, 516 (Pt 1), 1-17.
- ELLWARDT, E., PRAMANIK, G., LUCHTMAN, D., NOVKOVIC, T., JUBAL, E. R., VOGT, J., ARNOUX, I., VOGELAAR, C. F., MANDAL, S., SCHMALZ, M., BARGER, Z., RUIZ DE AZUA, I., KUHLMANN, T., LUTZ, B., MITTMANN, T., BITTNER, S., ZIPP, F. & STROH, A. 2018.

- Maladaptive cortical hyperactivity upon recovery from experimental autoimmune encephalomyelitis. *Nat Neurosci*, 21, 1392-1403.
- ESCOBET-MONTALBAN, A., GASPAROLI, F. M., NYLK, J., LIU, P., YANG, Z. & DHOLAKIA, K. 2018. Three-photon light-sheet fluorescence microscopy. *Opt Lett*, 43, 5484-5487.
- ESPINOSA, J. S. & STRYKER, M. P. 2012. Development and plasticity of the primary visual cortex. *Neuron*, 75, 230-49.
- EUSTON, D. R. & STEENLAND, H. W. 2014. Neuroscience. Memories--getting wired during sleep. *Science*, 344, 1087-8.
- FEINBERG, E. H. & MEISTER, M. 2015. Orientation columns in the mouse superior colliculus. *Nature*, 519, 229-32.
- FINKELSTEIN, A., FONTOLAN, L., ECONOMO, M. N., LI, N., ROMANI, S. & SVOBODA, K. 2021. Attractor dynamics gate cortical information flow during decision-making. *Nat Neurosci*, 24, 843-850.
- FISHER, Y. E., SILIES, M. & CLANDININ, T. R. 2015. Orientation Selectivity Sharpens Motion Detection in *Drosophila*. *Neuron*, 88, 390-402.
- FONG, M. F., MITCHELL, D. E., DUFFY, K. R. & BEAR, M. F. 2016. Rapid recovery from the effects of early monocular deprivation is enabled by temporary inactivation of the retinas. *Proc Natl Acad Sci U S A*, 113, 14139-14144.
- FRANCIS, N. A., WINKOWSKI, D. E., SHEIKHATTAR, A., ARMENGOL, K., BABADI, B. & KANOLD, P. O. 2018. Small Networks Encode Decision-Making in Primary Auditory Cortex. *Neuron*, 97, 885-897 e6.
- FREYER, F., ROBERTS, J. A., RITTER, P. & BREAKSPEAR, M. 2012. A canonical model of multistability and scale-invariance in biological systems. *PLoS Comput Biol*, 8, e1002634.
- FRIEDMAN, J., HASTIE, T. & TIBSHIRANI, R. 2008. Sparse inverse covariance estimation with the graphical lasso. *Biostatistics*, 9, 432-41.
- FRIEDRICH, J., ZHOU, P. & PANINSKI, L. 2017. Fast online deconvolution of calcium imaging data. *PLoS Comput Biol*, 13, e1005423.
- FU, T., ARNOUX, I., DÖRING, J., BACKHAUS, H., WATARI, H., STASEVICIUS, I., FAN, W. & STROH, A. 2021. Exploring two-photon optogenetics beyond 1100 nm for specific and effective all-optical physiology. *iScience*.
- FU, Y. & YAU, K. W. 2007. Phototransduction in mouse rods and cones. *Pflugers Arch*, 454, 805-19.
- FUCILE, S. 2004. Ca²⁺ permeability of nicotinic acetylcholine receptors. *Cell Calcium*, 35, 1-8.
- GARRETT, M. E., NAUHAUS, I., MARSH, J. H. & CALLAWAY, E. M. 2014. Topography and areal organization of mouse visual cortex. *J Neurosci*, 34, 12587-600.
- GHANBARI, L., CARTER, R. E., RYNES, M. L., DOMINGUEZ, J., CHEN, G., NAIK, A., HU, J., SAGAR, M. A. K., HALTOM, L., MOSSAZGHI, N., GRAY, M. M., WEST, S. L., ELICEIRI, K. W., EBNER, T. J. & KODANDARAMAIAH, S. B. 2019a. Cortex-wide neural interfacing via transparent polymer skulls. *Nat Commun*, 10, 1500.

- GHANBARI, L., RYNES, M. L., HU, J., SCHULMAN, D. S., JOHNSON, G. W., LAROQUE, M., SHULL, G. M. & KODANDARAMAIAH, S. B. 2019b. Craniobot: A computer numerical controlled robot for cranial microsurgeries. *Sci Rep*, 9, 1023.
- GIRE, D. H., WHITESELL, J. D., DOUCETTE, W. & RESTREPO, D. 2013. Information for decision-making and stimulus identification is multiplexed in sensory cortex. *Nat Neurosci*, 16, 991-3.
- GLICKFELD, L. L., HISTED, M. H. & MAUNSELL, J. H. 2013. Mouse primary visual cortex is used to detect both orientation and contrast changes. *J Neurosci*, 33, 19416-22.
- GLICKFELD, L. L., REID, R. C. & ANDERMANN, M. L. 2014. A mouse model of higher visual cortical function. *Curr Opin Neurobiol*, 24, 28-33.
- GLOBAL BURDEN OF DISEASE STUDY, C. 2015. Global, regional, and national incidence, prevalence, and years lived with disability for 301 acute and chronic diseases and injuries in 188 countries, 1990-2013: a systematic analysis for the Global Burden of Disease Study 2013. *Lancet*, 386, 743-800.
- GOLDEN, S. A., COVINGTON, H. E., 3RD, BERTON, O. & RUSSO, S. J. 2011. A standardized protocol for repeated social defeat stress in mice. *Nat Protoc*, 6, 1183-91.
- GÖPPERT-MAYER, M. 1931. Über Elementarakte mit zwei Quantensprüngen. *Annalen der Physik*, 401, 273-294.
- GOTTSCHALK, A. 2020. Optogenetic analyses of neuronal networks that generate behavior in *Caenorhabditis elegans*. *Neuroforum*, 26, 227-237.
- GRANDJEAN, J., AZZINNARI, D., SEUWEN, A., SIGRIST, H., SEIFRITZ, E., PRYCE, C. R. & RUDIN, M. 2016. Chronic psychosocial stress in mice leads to changes in brain functional connectivity and metabolite levels comparable to human depression. *Neuroimage*, 142, 544-552.
- GRAY, C. M. & SINGER, W. 1989. Stimulus-specific neuronal oscillations in orientation columns of cat visual cortex. *Proceedings of the National Academy of Sciences*, 86, 1698-1702.
- GREWE, B. F. & HELMCHEN, F. 2009. Optical probing of neuronal ensemble activity. *Curr Opin Neurobiol*, 19, 520-529.
- GRIENBERGER, C., GIOVANNUCCI, A., ZEIGER, W. & PORTERA-CAILLIAU, C. 2022. Two-photon calcium imaging of neuronal activity. *Nat Rev Methods Primers*, 2.
- GRIENBERGER, C. & KONNERTH, A. 2012. Imaging calcium in neurons. *Neuron*, 73, 862-885.
- GRUN, S., LI, J., MCNAUGHTON, B., PETERSEN, C., MCCORMICK, D., ROBSON, D., BUZSAKI, G., HARRIS, K., SEJNOWSKI, T., MRSIC-FLOGEL, T., LINDEN, H. & ROLAND, P. E. 2022. Emerging principles of spacetime in brains: Meeting report on spatial neurodynamics. *Neuron*, 110, 1894-1898.
- GUIMARAES BACKHAUS, R., FU, T., BACKHAUS, H. & STROH, A. 2021. Pipeline for 2-photon all-optical physiology in mouse: From viral titration and optical window implantation to binarization of calcium transients. *STAR Protoc*, 2, 101010.
- HAN, X. & BOYDEN, E. S. 2007. Multiple-color optical activation, silencing, and desynchronization of neural activity, with single-spike temporal resolution. *PLoS One*, 2, e299.

- HAN, X., CHOW, B. Y., ZHOU, H., KLAPOETKE, N. C., CHUONG, A., RAJIMEHR, R., YANG, A., BARATTA, M. V., WINKLE, J., DESIMONE, R. & BOYDEN, E. S. 2011. A high-light sensitivity optical neural silencer: development and application to optogenetic control of non-human primate cortex. *Front Syst Neurosci*, 5, 18.
- HATTAR, S., LUCAS, R. J., MROSOVSKY, N., THOMPSON, S., DOUGLAS, R. H., HANKINS, M. W., LEM, J., BIEL, M., HOFMANN, F., FOSTER, R. G. & YAU, K. W. 2003. Melanopsin and rod-cone photoreceptive systems account for all major accessory visual functions in mice. *Nature*, 424, 76-81.
- HEFENDEHL, J. K., MILFORD, D., EICKE, D., WEGENAST-BRAUN, B. M., CALHOUN, M. E., GRATHWOHL, S. A., JUCKER, M. & LIEBIG, C. 2012. Repeatable target localization for long-term in vivo imaging of mice with 2-photon microscopy. *J Neurosci Methods*, 205, 357-63.
- HELL, S. W., BAHLMANN, K., SCHRADER, M., SOINI, A., MALAK, H. M., GRYZCZYNSKI, I. & LAKOWICZ, J. R. 1996. Three-photon excitation in fluorescence microscopy. *J Biomed Opt*, 1, 71-4.
- HELMCHEN, F. & DENK, W. 2005. Deep tissue two-photon microscopy. *Nat Methods*, 2, 932-40.
- HELSON, P., LUNDQVIST, D., SVENNINGSSON, P., VINDING, M. C. & KUMAR, A. 2023. Cortex-wide topography of 1/f-exponent in Parkinson's disease. *NPJ Parkinsons Dis*, 9, 109.
- HENDEL, T., MANK, M., SCHNELL, B., GRIESBECK, O., BORST, A. & REIFF, D. F. 2008. Fluorescence changes of genetic calcium indicators and OGB-1 correlated with neural activity and calcium in vivo and in vitro. *J Neurosci*, 28, 7399-411.
- HENSCH, T. K. & QUINLAN, E. M. 2018. Critical periods in amblyopia. *Vis Neurosci*, 35, E014.
- HENSCHKE, J. U., DYLDA, E., KATSANEVAKI, D., DUPUY, N., CURRIE, S. P., AMVROSIADIS, T., PAKAN, J. M. P. & ROCHEFORT, N. L. 2020. Reward Association Enhances Stimulus-Specific Representations in Primary Visual Cortex. *Curr Biol*, 30, 1866-1880 e5.
- HERMAN, J. P. & CULLINAN, W. E. 1997. Neurocircuitry of stress: central control of the hypothalamo-pituitary-adrenocortical axis. *Trends Neurosci*, 20, 78-84.
- HIGLEY, M. J. & SABATINI, B. L. 2008. Calcium signaling in dendrites and spines: practical and functional considerations. *Neuron*, 59, 902-13.
- HODGKIN, A. L. & HUXLEY, A. F. 1939. Action Potentials Recorded from Inside a Nerve Fibre. *Nature*, 144, 710-711.
- HOOKS, B. M. & CHEN, C. 2020. Circuitry Underlying Experience-Dependent Plasticity in the Mouse Visual System. *Neuron*, 106, 21-36.
- HORTON, N. G., WANG, K., KOBAT, D., CLARK, C. G., WISE, F. W., SCHAFFER, C. B. & XU, C. 2013. In vivo three-photon microscopy of subcortical structures within an intact mouse brain. *Nat Photonics*, 7, 205-9.
- HUBER, D., GUTNISKY, D. A., PERON, S., O'CONNOR, D. H., WIEGERT, J. S., TIAN, L., OERTNER, T. G., LOOGER, L. L. & SVOBODA, K. 2012. Multiple dynamic representations in the motor cortex during sensorimotor learning. *Nature*, 484, 473-478.

- HUBERMAN, A. D., WEI, W., ELSTROTT, J., STAFFORD, B. K., FELLER, M. B. & BARRES, B. A. 2009. Genetic identification of an On-Off direction-selective retinal ganglion cell subtype reveals a layer-specific subcortical map of posterior motion. *Neuron*, 62, 327-34.
- JIN, D., BOIADJIEVA, B., BACKHAUS, H., FAUSS, M., FU, T., STROH, A., KLEIN, A. & ZOUBIR, A. M. 2018. Analysis of Activity States of Local Neuronal Microcircuits in Mouse Brain. *2018 26th European Signal Processing Conference (EUSIPCO)*.
- JUNG, J. C. & SCHNITZER, M. J. 2003. Multiphoton endoscopy. *Opt Lett*, 28, 902-4.
- KAIFOSH, P., ZAREMBA, J. D., DANIELSON, N. B. & LOSONCZY, A. 2014. SIMA: Python software for analysis of dynamic fluorescence imaging data. *Front Neuroinform*, 8, 80.
- KAISER, R. H., CHASE, H. W., PHILLIPS, M. L., DECKERSBACH, T., PARSEY, R. V., FAVA, M., MCGRATH, P. J., WEISSMAN, M., OQUENDO, M. A., MCINNIS, M. G., CARMODY, T., COOPER, C. M., TRIVEDI, M. H. & PIZZAGALLI, D. A. 2022. Dynamic Resting-State Network Biomarkers of Antidepressant Treatment Response. *Biol Psychiatry*, 92, 533-542.
- KALISCH, R., BAKER, D. G., BASTEN, U., BOKS, M. P., BONANNO, G. A., BRUMMELMAN, E., CHMITORZ, A., FERNANDEZ, G., FIEBACH, C. J., GALATZER-LEVY, I., GEUZE, E., GROPPA, S., HELMREICH, I., HENDLER, T., HERMANS, E. J., JOVANOVIĆ, T., KUBIAK, T., LIEB, K., LUTZ, B., MULLER, M. B., MURRAY, R. J., NIEVERGELT, C. M., REIF, A., ROELOFS, K., RUTTEN, B. P. F., SANDER, D., SCHICK, A., TUSCHER, O., DIEST, I. V., HARMELEN, A. V., VEER, I. M., VERMETTEN, E., VINKERS, C. H., WAGER, T. D., WALTER, H., WESSA, M., WIBRAL, M. & KLEIM, B. 2017. The resilience framework as a strategy to combat stress-related disorders. *Nat Hum Behav*, 1, 784-790.
- KALISCH, R., CRAMER, A. O. J., BINDER, H., FRITZ, J., LEERTOUWER, I., LUNANSKY, G., MEYER, B., TIMMER, J., VEER, I. M. & VAN HARMELEN, A. L. 2019. Deconstructing and Reconstructing Resilience: A Dynamic Network Approach. *Perspect Psychol Sci*, 14, 765-777.
- KANDEL, E. 2013. *Principles of Neural Science*, McGraw Hill Professional.
- KEEMINK, S. W., LOWE, S. C., PAKAN, J. M. P., DYLD, E., VAN ROSSUM, M. C. W. & ROCHEFORT, N. L. 2018. FISSA: A neuropil decontamination toolbox for calcium imaging signals. *Sci Rep*, 8, 3493.
- KELBER, A. 2018. Vision: Rods See in Bright Light. *Curr Biol*, 28, R364-R366.
- KERR, J. N., GREENBERG, D. & HELMCHEN, F. 2005. Imaging input and output of neocortical networks in vivo. *Proc.Natl.Acad.Sci.U.S.A*, 102, 14063-14068.
- KETKAR, M. D., GUR, B., MOLINA-OBANDO, S., IOANNIDOU, M., MARTELLI, C. & SILIES, M. 2022. First-order visual interneurons distribute distinct contrast and luminance information across ON and OFF pathways to achieve stable behavior. *Elife*, 11.
- KIM, D. H., KIM, J., MARQUES, J. C., GRAMA, A., HILDEBRAND, D. G. C., GU, W., LI, J. M. & ROBSON, D. N. 2017. Pan-neuronal calcium imaging with cellular resolution in freely swimming zebrafish. *Nat Methods*, 14, 1107-1114.
- KLIBISZ, A., ROSE, D., EICHOLTZ, M., BLUNDON, J. & ZAKHARENKO, S. 2017. Fast, Simple Calcium Imaging Segmentation with Fully Convolutional Networks. *Deep Learning in Medical Image Analysis and Multimodal Learning for Clinical Decision Support*.

- KO, H., MRSIC-FLOGEL, T. D. & HOFER, S. B. 2014. Emergence of feature-specific connectivity in cortical microcircuits in the absence of visual experience. *J Neurosci*, 34, 9812-6.
- KOBAT, D., HORTON, N. G. & XU, C. 2011. In vivo two-photon microscopy to 1.6-mm depth in mouse cortex. *J Biomed Opt*, 16, 106014.
- KOENEN, K. C., RATANATHARATHORN, A., NG, L., MCLAUGHLIN, K. A., BROMET, E. J., STEIN, D. J., KARAM, E. G., MERON RUSCIO, A., BENJET, C., SCOTT, K., ATWOLI, L., PETUKHOVA, M., LIM, C. C. W., AGUILAR-GAXIOLA, S., AL-HAMZAWI, A., ALONSO, J., BUNTING, B., CIUTAN, M., DE GIROLAMO, G., DEGENHARDT, L., GUREJE, O., HARO, J. M., HUANG, Y., KAWAKAMI, N., LEE, S., NAVARRO-MATEU, F., PENNELL, B. E., PIAZZA, M., SAMPSON, N., TEN HAVE, M., TORRES, Y., VIANA, M. C., WILLIAMS, D., XAVIER, M. & KESSLER, R. C. 2017. Posttraumatic stress disorder in the World Mental Health Surveys. *Psychol Med*, 47, 2260-2274.
- KRISHNAN, V., HAN, M. H., GRAHAM, D. L., BERTON, O., RENTHAL, W., RUSSO, S. J., LAPLANT, Q., GRAHAM, A., LUTTER, M., LAGACE, D. C., GHOSE, S., REISTER, R., TANNOUS, P., GREEN, T. A., NEVE, R. L., CHAKRAVARTY, S., KUMAR, A., EISCH, A. J., SELF, D. W., LEE, F. S., TAMMINGA, C. A., COOPER, D. C., GERSHENFELD, H. K. & NESTLER, E. J. 2007. Molecular adaptations underlying susceptibility and resistance to social defeat in brain reward regions. *Cell*, 131, 391-404.
- KRISHNAN, V. & NESTLER, E. J. 2008. The molecular neurobiology of depression. *Nature*, 455, 894-902.
- KRISHNAN, V. & NESTLER, E. J. 2010. Linking molecules to mood: new insight into the biology of depression. *Am J Psychiatry*, 167, 1305-20.
- KRUEGER, J. N. & SANGHA, S. 2021. On the basis of sex: Differences in safety discrimination vs. conditioned inhibition. *Behav Brain Res*, 400, 113024.
- KUDRYAVTSEVA, N. N., BAKSHANOVSKAYA, I. V. & KORYAKINA, L. A. 1991. Social model of depression in mice of C57BL/6J strain. *Pharmacol Biochem Behav*, 38, 315-20.
- KUMAR, S., HULTMAN, R., HUGHES, D., MICHEL, N., KATZ, B. M. & DZIRASA, K. 2014. Prefrontal cortex reactivity underlies trait vulnerability to chronic social defeat stress. *Nat Commun*, 5, 4537.
- LAXPATI, N. G., MAHMOUDI, B., GUTEKUNST, C. A., NEWMAN, J. P., ZELLER-TOWNSON, R. & GROSS, R. E. 2014. Real-time in vivo optogenetic neuromodulation and multielectrode electrophysiologic recording with NeuroRighter. *Front Neuroeng*, 7, 40.
- LESCHIK, J., GENTILE, A., CICEK, C., PERON, S., TEVOSIAN, M., BEER, A., RADYUSHKIN, K., BLUDAU, A., EBNER, K., NEUMANN, I., SINGEWALD, N., BERNINGER, B., LESSMANN, V. & LUTZ, B. 2022. Brain-derived neurotrophic factor expression in serotonergic neurons improves stress resilience and promotes adult hippocampal neurogenesis. *Prog Neurobiol*, 217, 102333.
- LEVENE, M. J., DOMBECK, D. A., KASISCHKE, K. A., MOLLOY, R. P. & WEBB, W. W. 2004. In vivo multiphoton microscopy of deep brain tissue. *J Neurophysiol*, 91, 1908-12.
- LOPRESTO, D., SCHIPPER, P. & HOMBERG, J. R. 2016. Neural circuits and mechanisms involved in fear generalization: Implications for the pathophysiology and treatment of posttraumatic stress disorder. *Neurosci Biobehav Rev*, 60, 31-42.

- LOW, R. J., GU, Y. & TANK, D. W. 2014. Cellular resolution optical access to brain regions in fissures: imaging medial prefrontal cortex and grid cells in entorhinal cortex. *Proc Natl Acad Sci U S A*, 111, 18739-44.
- LUAN, S., WILLIAMS, I., NIKOLIC, K. & CONSTANDINO, T. G. 2014. Neuromodulation: present and emerging methods. *Front Neuroeng*, 7, 27.
- LUCZAK, A., BARTHO, P. & HARRIS, K. D. 2013. Gating of sensory input by spontaneous cortical activity. *J Neurosci*, 33, 1684-95.
- LYONS, D. M., AYASH, S., SCHATZBERG, A. F. & MULLER, M. B. 2023. Ecological validity of social defeat stressors in mouse models of vulnerability and resilience. *Neurosci Biobehav Rev*, 145, 105032.
- MALDONADO, P. E., CONCHA-MIRANDA, M. & SCHWALM, M. 2023. Autogenous cerebral processes: an invitation to look at the brain from inside out. *Front Neural Circuits*, 17, 1253609.
- MANK, M., SANTOS, A. F., DIRENBERGER, S., MRSIC-FLOGEL, T. D., HOFER, S. B., STEIN, V., HENDEL, T., REIFF, D. F., LEVELT, C., BORST, A., BONHOEFFER, T., HUBENER, M. & GRIESBECK, O. 2008. A genetically encoded calcium indicator for chronic in vivo two-photon imaging. *Nat. Methods*, 5, 805-811.
- MARDINLY, A. R., OLDENBURG, I. A., PEGARD, N. C., SRIDHARAN, S., LYALL, E. H., CHESNOV, K., BROHAWN, S. G., WALLER, L. & ADESNIK, H. 2018. Precise multimodal optical control of neural ensemble activity. *Nat Neurosci*, 21, 881-893.
- MARGOLIS, D. J., LUTCKE, H., SCHULZ, K., HAISS, F., WEBER, B., KUGLER, S., HASAN, M. T. & HELMCHEN, F. 2012. Reorganization of cortical population activity imaged throughout long-term sensory deprivation. *Nat Neurosci*, 15, 1539-46.
- MARSHALL, L., HELGADOTTIR, H., MOLLE, M. & BORN, J. 2006. Boosting slow oscillations during sleep potentiates memory. *Nature*, 444, 610-3.
- MARSHEL, J. H., GARRETT, M. E., NAUHAUS, I. & CALLAWAY, E. M. 2011. Functional specialization of seven mouse visual cortical areas. *Neuron*, 72, 1040-54.
- MARSHEL, J. H., KIM, Y. S., MACHADO, T. A., QUIRIN, S., BENSON, B., KADMON, J., RAJA, C., CHIBUKHCHYAN, A., RAMAKRISHNAN, C., INOUE, M., SHANE, J. C., MCKNIGHT, D. J., YOSHIZAWA, S., KATO, H. E., GANGULI, S. & DEISSEROTH, K. 2019. Cortical layer-specific critical dynamics triggering perception. *Science*, 365.
- MASSIMINI, M., HUBER, R., FERRARELLI, F., HILL, S. & TONONI, G. 2004. The sleep slow oscillation as a traveling wave. *J. Neurosci.*, 24, 6862-6870.
- MCTEAGUE, L. M., ROSENBERG, B. M., LOPEZ, J. W., CARREON, D. M., HUEMER, J., JIANG, Y., CHICK, C. F., EICKHOFF, S. B. & ETKIN, A. 2020. Identification of Common Neural Circuit Disruptions in Emotional Processing Across Psychiatric Disorders. *Am J Psychiatry*, 177, 411-421.
- MESCHEDE, D. 2015. *Gerthsen Physik*.
- MISIC, B. & SPORNS, O. 2016. From regions to connections and networks: new bridges between brain and behavior. *Curr Opin Neurobiol*, 40, 1-7.

- MÖLLE, M., YESHENKO, O., MARSHALL, L., SARA, S. J. & BORN, J. 2006. Hippocampal Sharp Wave-Ripples Linked to Slow Oscillations in Rat Slow-Wave Sleep. *Journal of Neurophysiology*, 96, 62-70.
- MORGAN, C. A., 3RD, RASMUSSEN, A. M., WANG, S., HOYT, G., HAUGER, R. L. & HAZLETT, G. 2002. Neuropeptide-Y, cortisol, and subjective distress in humans exposed to acute stress: replication and extension of previous report. *Biol Psychiatry*, 52, 136-42.
- MORGAN, C. A., 3RD, WANG, S., SOUTHWICK, S. M., RASMUSSEN, A., HAZLETT, G., HAUGER, R. L. & CHARNEY, D. S. 2000. Plasma neuropeptide-Y concentrations in humans exposed to military survival training. *Biol Psychiatry*, 47, 902-9.
- MUKHERJEE, S., HEATH, L., PREUSS, C., JAYADEV, S., GARDEN, G. A., GREENWOOD, A. K., SIEBERTS, S. K., DE JAGER, P. L., ERTEKIN-TANER, N., CARTER, G. W., MANGRAVITE, L. M. & LOGSDON, B. A. 2020. Molecular estimation of neurodegeneration pseudotime in older brains. *Nat Commun*, 11, 5781.
- MURROUGH, J. W. & CHARNEY, D. S. 2011. The serotonin transporter and emotionality: risk, resilience, and new therapeutic opportunities. *Biol Psychiatry*, 69, 510-2.
- MYERS, B., MCKLVEEN, J. M. & HERMAN, J. P. 2014. Glucocorticoid actions on synapses, circuits, and behavior: implications for the energetics of stress. *Front Neuroendocrinol*, 35, 180-196.
- NAGEL, G., OLLIG, D., FUHRMANN, M., KATERIYA, S., MUSTI, A. M., BAMBERG, E. & HEGEMANN, P. 2002. Channelrhodopsin-1: a light-gated proton channel in green algae. *Science*, 296, 2395-8.
- NAGEL, G., SZELLAS, T., HUHN, W., KATERIYA, S., ADEISHVILI, N., BERTHOLD, P., OLLIG, D., HEGEMANN, P. & BAMBERG, E. 2003. Channelrhodopsin-2, a directly light-gated cation-selective membrane channel. *Proc.Natl.Acad.Sci.U.S.A*, 100, 13940-13945.
- NAKAI, J., OHKURA, M. & IMOTO, K. 2001. A high signal-to-noise Ca(2+) probe composed of a single green fluorescent protein. *Nat Biotechnol*, 19, 137-41.
- NATH, A. & SCHWARTZ, G. W. 2016. Cardinal Orientation Selectivity Is Represented by Two Distinct Ganglion Cell Types in Mouse Retina. *J Neurosci*, 36, 3208-21.
- NESTLER, E. J. & HYMAN, S. E. 2010. Animal models of neuropsychiatric disorders. *Nat Neurosci*, 13, 1161-9.
- NIELL, C. M. & STRYKER, M. P. 2010. Modulation of visual responses by behavioral state in mouse visual cortex. *Neuron*, 65, 472-479.
- NIENBORG, H. & CUMMING, B. G. 2009. Decision-related activity in sensory neurons reflects more than a neuron's causal effect. *Nature*, 459, 89-92.
- NISWENDER, C. M. & CONN, P. J. 2010. Metabotropic glutamate receptors: physiology, pharmacology, and disease. *Annu Rev Pharmacol Toxicol*, 50, 295-322.
- NOSEDA, R. & BURSTEIN, R. 2011. Advances in understanding the mechanisms of migraine-type photophobia. *Curr Opin Neurol*, 24, 197-202.
- OUZOUNOV, D. G., WANG, T., WANG, M., FENG, D. D., HORTON, N. G., CRUZ-HERNANDEZ, J. C., CHENG, Y. T., REIMER, J., TOLIAS, A. S., NISHIMURA, N. & XU, C. 2017. In vivo three-photon imaging of activity of GCaMP6-labeled neurons deep in intact mouse brain. *Nat Methods*, 14, 388-390.

- PACHITARIU, M., STRINGER, C., DIOPPA, M., SCHRÖDER, S., ROSSI, L. F., DALGLEISH, H., CARANDINI, M. & HARRIS, K. D. 2017.
- PACKER, A. M., PETERKA, D. S., HIRTZ, J. J., PRAKASH, R., DEISSEROTH, K. & YUSTE, R. 2012. Two-photon optogenetics of dendritic spines and neural circuits. *Nat.Methods*, 9, 1202-1205.
- PAKAN, J. M., LOWE, S. C., DYLD, E., KEEMINK, S. W., CURRIE, S. P., COUTTS, C. A. & ROCHEFORT, N. L. 2016. Behavioral-state modulation of inhibition is context-dependent and cell type specific in mouse visual cortex. *Elife*, 5.
- PAPAGIAKOU MOU, E., ANSELM, F., BEGUE, A., DE SANS, V., GLUCKSTAD, J., ISACOFF, E. Y. & EMILIANI, V. 2010. Scanless two-photon excitation of channelrhodopsin-2. *Nat Methods*, 7, 848-54.
- PAREDES, R. M., ETZLER, J. C., WATTS, L. T., ZHENG, W. & LECHLEITER, J. D. 2008. Chemical calcium indicators. *Methods*, 46, 143-51.
- PAUKERT, M. & BERGLES, D. E. 2012. Reduction of motion artifacts during in vivo two-photon imaging of brain through heartbeat triggered scanning. *J Physiol*, 590, 2955-63.
- PETERS, A. J., CHEN, S. X. & KOMIYAMA, T. 2014. Emergence of reproducible spatiotemporal activity during motor learning. *Nature*, 510, 263-7.
- PETERSEN, C. C. & CROCHET, S. 2013. Synaptic computation and sensory processing in neocortical layer 2/3. *Neuron*, 78, 28-48.
- PILZ, G. A., CARTA, S., STAUBLE, A., AYAZ, A., JESSBERGER, S. & HELMCHEN, F. 2016. Functional Imaging of Dentate Granule Cells in the Adult Mouse Hippocampus. *J Neurosci*, 36, 7407-14.
- PNEVMATIKAKIS, E. A. 2019. Analysis pipelines for calcium imaging data. *Curr Opin Neurobiol*, 55, 15-21.
- PNEVMATIKAKIS, E. A., SOUDRY, D., GAO, Y., MACHADO, T. A., MEREL, J., PFAU, D., REARDON, T., MU, Y., LACEFIELD, C., YANG, W., AHRENS, M., BRUNO, R., JESSELL, T. M., PETERKA, D. S., YUSTE, R. & PANINSKI, L. 2016. Simultaneous Denoising, Deconvolution, and Demixing of Calcium Imaging Data. *Neuron*, 89, 285-99.
- POLANCZYK, G., CASPI, A., WILLIAMS, B., PRICE, T. S., DANESE, A., SUGDEN, K., UHER, R., POULTON, R. & MOFFITT, T. E. 2009. Protective effect of CRHR1 gene variants on the development of adult depression following childhood maltreatment: replication and extension. *Arch Gen Psychiatry*, 66, 978-85.
- PRESSON, R. G., JR., BROWN, M. B., FISHER, A. J., SANDOVAL, R. M., DUNN, K. W., LORENZ, K. S., DELP, E. J., SALAMA, P., MOLITORIS, B. A. & PETRACHE, I. 2011. Two-photon imaging within the murine thorax without respiratory and cardiac motion artifact. *Am J Pathol*, 179, 75-82.
- QIN, Z., SHE, Z., CHEN, C., WU, W., LAU, J. K. Y., IP, N. Y. & QU, J. Y. 2022. Deep tissue multi-photon imaging using adaptive optics with direct focus sensing and shaping. *Nat Biotechnol*, 40, 1663-1671.
- RAMSEY, I. S., DELLING, M. & CLAPHAM, D. E. 2006. An introduction to TRP channels. *Annu Rev Physiol*, 68, 619-47.

- RASMUSSEN, A. M., VYTHILINGAM, M. & MORGAN, C. A., 3RD 2003. The neuroendocrinology of posttraumatic stress disorder: new directions. *CNS Spectr*, 8, 651-6, 665-7.
- REDINBAUGH, M. J., PHILLIPS, J. M., KAMBI, N. A., MOHANTA, S., ANDRYK, S., DOOLEY, G. L., AFRASIABI, M., RAZ, A. & SAALMANN, Y. B. 2020. Thalamus Modulates Consciousness via Layer-Specific Control of Cortex. *Neuron*, 106, 66-75 e12.
- RESSLER, K. J., MERCER, K. B., BRADLEY, B., JOVANOVIĆ, T., MAHAN, A., KERLEY, K., NORRHOLM, S. D., KILARU, V., SMITH, A. K., MYERS, A. J., RAMIREZ, M., ENGEL, A., HAMMACK, S. E., TOUFEXIS, D., BRAAS, K. M., BINDER, E. B. & MAY, V. 2011. Post-traumatic stress disorder is associated with PACAP and the PAC1 receptor. *Nature*, 470, 492-7.
- RIBEIRO, S., GERVASONI, D., SOARES, E. S., ZHOU, Y., LIN, S. C., PANTOJA, J., LAVINE, M. & NICOLELIS, M. A. 2004. Long-lasting novelty-induced neuronal reverberation during slow-wave sleep in multiple forebrain areas. *PLoS Biol*, 2, E24.
- RICHARDS, B. A., LILLICRAP, T. P., BEAUDOIN, P., BENGIO, Y., BOGACZ, R., CHRISTENSEN, A., CLOPATH, C., COSTA, R. P., DE BERKER, A., GANGULI, S., GILLON, C. J., HAFNER, D., KEPECS, A., KRIEGESKORTE, N., LATHAM, P., LINDSAY, G. W., MILLER, K. D., NAUD, R., PACK, C. C., POIRAZI, P., ROELFSEMA, P., SACRAMENTO, J., SAXE, A., SCELLIER, B., SCHAPIRO, A. C., SENN, W., WAYNE, G., YAMINS, D., ZENKE, F., ZYLBERBERG, J., THERIEN, D. & KORDING, K. P. 2019. A deep learning framework for neuroscience. *Nat Neurosci*, 22, 1761-1770.
- RINGACH, D. L., SHAPLEY, R. M. & HAWKEN, M. J. 2002. Orientation selectivity in macaque V1: diversity and laminar dependence. *J Neurosci*, 22, 5639-51.
- ROCHEFORT, N. L., GARASCHUK, O., MILOS, R. I., NARUSHIMA, M., MARANDI, N., PICHLER, B., KOVALCHUK, Y. & KONNERTH, A. 2009. Sparsification of neuronal activity in the visual cortex at eye-opening. *Proc Natl Acad Sci U S A*, 106, 15049-54.
- RODRIGUEZ, C., CHEN, A., RIVERA, J. A., MOHR, M. A., LIANG, Y., NATAN, R. G., SUN, W., MILKIE, D. E., BIFANO, T. G., CHEN, X. & JI, N. 2021. An adaptive optics module for deep tissue multiphoton imaging in vivo. *Nat Methods*, 18, 1259-1264.
- RODRIGUEZ, C. & JI, N. 2021. One wavelength to excite them all: deep tissue imaging going multicolor. *Trends Neurosci*, 44, 689-691.
- ROSALES JUBAL, E., SCHWALM, M., DOS SANTOS GUILHERME, M., SCHUCK, F., REINHARDT, S., TOSE, A., BARGER, Z., ROESLER, M. K., RUFFINI, N., WIERCZEIKO, A., SCHMEISSER, M. J., SCHMITT, U., ENDRES, K. & STROH, A. 2021. Acitretin reverses early functional network degradation in a mouse model of familial Alzheimer's disease. *Sci Rep*, 11, 6649.
- ROSENBERG, P. B., NOWRANGI, M. A. & LYKETSOS, C. G. 2015. Neuropsychiatric symptoms in Alzheimer's disease: What might be associated brain circuits? *Mol Aspects Med*, 43-44, 25-37.
- ROTH, M. M., DAHMEN, J. C., MUIR, D. R., IMHOF, F., MARTINI, F. J. & HOFER, S. B. 2016. Thalamic nuclei convey diverse contextual information to layer 1 of visual cortex. *Nat Neurosci*, 19, 299-307.
- RYGULA, R., ABUMARIA, N., DOMENICI, E., HIEMKE, C. & FUCHS, E. 2006a. Effects of fluoxetine on behavioral deficits evoked by chronic social stress in rats. *Behav Brain Res*, 174, 188-92.

- RYGULA, R., ABUMARIA, N., FLUGGE, G., FUCHS, E., RUTHER, E. & HAVEMANN-REINECKE, U. 2005. Anhedonia and motivational deficits in rats: impact of chronic social stress. *Behav Brain Res*, 162, 127-34.
- RYGULA, R., ABUMARIA, N., FLÜGGE, G., HIEMKE, C., FUCHS, E., RÜTHER, E. & HAVEMANN-REINECKE, U. 2006b. Citalopram counteracts depressive-like symptoms evoked by chronic social stress in rats. *Behavioural Pharmacology*, 17, 19-29.
- SAFAI, A., VAKHARIA, N., PRASAD, S., SAINI, J., SHAH, A., LENKA, A., PAL, P. K. & INGALHALIKAR, M. 2021. Multimodal Brain Connectomics-Based Prediction of Parkinson's Disease Using Graph Attention Networks. *Front Neurosci*, 15, 741489.
- SANCHEZ-VIVES, M. V. & MCCORMICK, D. A. 2000. Cellular and network mechanisms of rhythmic recurrent activity in neocortex. *Nat. Neurosci.*, 3, 1027-1034.
- SANEI, S. & CHAMBERS, J. A. 2007. *EEG Signal Processing*.
- SATO, M. & STRYKER, M. P. 2010. Genomic imprinting of experience-dependent cortical plasticity by the ubiquitin ligase gene *Ube3a*. *Proc Natl Acad Sci U S A*, 107, 5611-6.
- SCHEFFER, M., BASCOMPTE, J., BROCK, W. A., BROVKIN, V., CARPENTER, S. R., DAKOS, V., HELD, H., VAN NES, E. H., RIETKERK, M. & SUGIHARA, G. 2009. Early-warning signals for critical transitions. *Nature*, 461, 53-9.
- SCHEFFER, M., CARPENTER, S. R., LENTON, T. M., BASCOMPTE, J., BROCK, W., DAKOS, V., VAN DE KOPPEL, J., VAN DE LEEMPUT, I. A., LEVIN, S. A., VAN NES, E. H., PASCUAL, M. & VANDERMEER, J. 2012. Anticipating critical transitions. *Science*, 338, 344-8.
- SCHINDELIN, J., ARGANDA-CARRERAS, I., FRISE, E., KAYNIG, V., LONGAIR, M., PIETZSCH, T., PREIBISCH, S., RUEDEN, C., SAALFELD, S., SCHMID, B., TINEVEZ, J. Y., WHITE, D. J., HARTENSTEIN, V., ELICEIRI, K., TOMANCAK, P. & CARDONA, A. 2012. Fiji: an open-source platform for biological-image analysis. *Nat Methods*, 9, 676-82.
- SCHMID, F., WACHSMUTH, L., ALBERS, F., SCHWALM, M., STROH, A. & FABER, C. 2017. True and apparent optogenetic BOLD fMRI signals. *Magn Reson Med*, 77, 126-136.
- SCHMID, F., WACHSMUTH, L., SCHWALM, M., PROUVOT, P. H., JUBAL, E. R., FOIS, C., PRAMANIK, G., ZIMMER, C., FABER, C. & STROH, A. 2016. Assessing sensory versus optogenetic network activation by combining (o)fMRI with optical Ca²⁺ recordings. *J Cereb Blood Flow Metab*, 36, 1885-1900.
- SCHMIDT, F. & SCHAIBLE, H. G. 2006. *Neuro- und Sinnesphysiologie*.
- SCHOBERT B, L. J. 1982. Halorhodopsin is a light-driven chloride pump. *J Biol Chem*, 257.
- SCHWALLER, B. 2010. Cytosolic Ca²⁺ buffers. *Cold Spring Harb Perspect Biol*, 2, a004051.
- SCHWALM, M., ROSALES JUBAL, E. & STROH, A. 2018. Towards Opto-Magnetic Physiology: Concepts and Pitfalls of ofMRI. *Optogenetics: A Roadmap*.
- SEABROOK, T. A., BURBRIDGE, T. J., CRAIR, M. C. & HUBERMAN, A. D. 2017. Architecture, Function, and Assembly of the Mouse Visual System. *Annu Rev Neurosci*, 40, 499-538.
- SEP, M. S. C., STEENMEIJER, A. & KENNIS, M. 2019. The relation between anxious personality traits and fear generalization in healthy subjects: A systematic review and meta-analysis. *Neurosci Biobehav Rev*, 107, 320-328.

- SINEFELD, D., XIA, F., WANG, M., WANG, T., WU, C., YANG, X., PAUDEL, H. P., OUZOUNOV, D. G., BIFANO, T. G. & XU, C. 2022. Three-Photon Adaptive Optics for Mouse Brain Imaging. *Front Neurosci*, 16, 880859.
- SINGER, W. 2009. The Brain, a Complex Self-organizing System. *European Review*, 17, 321-329.
- SINGER, W. 2013. Cortical dynamics revisited. *Trends Cogn Sci*, 17, 616-26.
- SINGH, S. & BRADLEY, L. T. 1964. Three-Photon Absorption in Napthalene Crystals by Laser Excitation. *Physical Review Letters*, 12, 612-614.
- SOHYA, K., KAMEYAMA, K., YANAGAWA, Y., OBATA, K. & TSUMOTO, T. 2007. GABAergic neurons are less selective to stimulus orientation than excitatory neurons in layer II/III of visual cortex, as revealed by in vivo functional Ca²⁺ imaging in transgenic mice. *J Neurosci*, 27, 2145-9.
- SOLTANIAN-ZADEH, S., SAHINGUR, K., BLAU, S., GONG, Y. & FARSIU, S. 2019. Fast and robust active neuron segmentation in two-photon calcium imaging using spatiotemporal deep learning. *Proc Natl Acad Sci U S A*, 116, 8554-8563.
- SONG, L., HENNINK, E. J., YOUNG, I. T. & TANKE, H. J. 1995. Photobleaching kinetics of fluorescein in quantitative fluorescence microscopy. *Biophys J*, 68, 2588-600.
- SPEED, A., DEL ROSARIO, J., MIKAIL, N. & HAIDER, B. 2020. Spatial attention enhances network, cellular and subthreshold responses in mouse visual cortex. *Nat Commun*, 11, 505.
- SRIDHARAN, S., GAJOWA, M. A., OGANDO, M. B., JAGADISAN, U. K., ABDELADIM, L., SADAHIRO, M., BOUNDS, H. A., HENDRICKS, W. D., TURNEY, T. S., TAYLER, I., GOPAKUMAR, K., OLDENBURG, I. A., BROHAWN, S. G. & ADESNIK, H. 2022. High-performance microbial opsins for spatially and temporally precise perturbations of large neuronal networks. *Neuron*, 110, 1139-1155 e6.
- STAMATAKIS, A. M., SCHACHTER, M. J., GULATI, S., ZITELLI, K. T., MALANOWSKI, S., TAJIK, A., FRITZ, C., TRULSON, M. & OTTE, S. L. 2018. Simultaneous Optogenetics and Cellular Resolution Calcium Imaging During Active Behavior Using a Miniaturized Microscope. *Front Neurosci*, 12, 496.
- STARESINA, B. P., BERGMANN, T. O., BONNEFOND, M., VAN DER MEIJ, R., JENSEN, O., DEUKER, L., ELGER, C. E., AXMACHER, N. & FELL, J. 2015. Hierarchical nesting of slow oscillations, spindles and ripples in the human hippocampus during sleep. *Nature Neuroscience*, 18, 1679-1686.
- STEIN, M. B., CAMPBELL-SILLS, L. & GELERNTER, J. 2009. Genetic variation in 5HTTLPR is associated with emotional resilience. *Am J Med Genet B Neuropsychiatr Genet*, 150B, 900-6.
- STIRMAN, J. N., SMITH, I. T., KUDENOV, M. W. & SMITH, S. L. 2016. Wide field-of-view, multi-region, two-photon imaging of neuronal activity in the mammalian brain. *Nat Biotechnol*, 34, 857-62.
- STISO, J., KHAMBHATI, A. N., MENARA, T., KAHN, A. E., STEIN, J. M., DAS, S. R., GORNIK, R., TRACY, J., LITT, B., DAVIS, K. A., PASQUALETTI, F., LUCAS, T. H. & BASSETT, D. S. 2019. White Matter Network Architecture Guides Direct Electrical Stimulation through Optimal State Transitions. *Cell Rep*, 28, 2554-2566 e7.
- STOSIEK, C., GARASCHUK, O., HOLTTHOFF, K. & KONNERTH, A. 2003. In vivo two-photon calcium imaging of neuronal networks. *Proc Natl Acad Sci U S A*, 100, 7319-24.

- STREICH, L., BOFFI, J. C., WANG, L., ALHALASEH, K., BARBIERI, M., REHM, R., DEIVASIGAMANI, S., GROSS, C. T., AGARWAL, A. & PREVEDEL, R. 2021. High-resolution structural and functional deep brain imaging using adaptive optics three-photon microscopy. *Nat Methods*, 18, 1253-1258.
- STRINGER, C., PACHITARIU, M., STEINMETZ, N., REDDY, C. B., CARANDINI, M. & HARRIS, K. D. 2019. Spontaneous behaviors drive multidimensional, brainwide activity. *Science*, 364, 255.
- STROH, A., ADELSBERGER, H., GROH, A., RUHLMANN, C., FISCHER, S., SCHIERLOH, A., DEISSEROTH, K. & KONNERTH, A. 2013. Making waves: initiation and propagation of corticothalamic Ca²⁺ waves in vivo. *Neuron*, 77, 1136-50.
- STROH, A., SCHWEIGER, S., RAMIREZ, J. M. & TUSCHER, O. 2024. The selfish network: how the brain preserves behavioral function through shifts in neuronal network state. *Trends Neurosci*.
- STROTZER, M. 2009. One century of brain mapping using Brodmann areas. *Klin Neuroradiol*, 19, 179-86.
- STYR, B., GONEN, N., ZARHIN, D., RUGGIERO, A., ATSMON, R., GAZIT, N., BRAUN, G., FRERE, S., VERTKIN, I., SHAPIRA, I., HAREL, M., HEIM, L. R., KATSENELSON, M., RECHNITZ, O., FADILA, S., DERDIKMAN, D., RUBINSTEIN, M., GEIGER, T., RUPPIN, E. & SLUTSKY, I. 2019. Mitochondrial Regulation of the Hippocampal Firing Rate Set Point and Seizure Susceptibility. *Neuron*, 102, 1009-1024 e8.
- SUGDEN, A. U., ZAREMBA, J. D., SUGDEN, L. A., MCGUIRE, K. L., LUTAS, A., RAMESH, R. N., ALTURKISTANI, O., LENSJO, K. K., BURGESS, C. R. & ANDERMANN, M. L. 2020. Cortical reactivations of recent sensory experiences predict bidirectional network changes during learning. *Nat Neurosci*, 23, 981-991.
- SUNG, Y. J., YANG, C., NORTON, J., JOHNSON, M., FAGAN, A., BATEMAN, R. J., PERRIN, R. J., MORRIS, J. C., FARLOW, M. R., CHHATWAL, J. P., SCHOFIELD, P. R., CHUI, H., WANG, F., NOVOTNY, B., ETELEEB, A., KARCH, C., SCHINDLER, S. E., RHINN, H., JOHNSON, E. C. B., OH, H. S., RUTLEDGE, J. E., DAMMER, E. B., SEYFRIED, N. T., WYSS-CORAY, T., HARARI, O. & CRUCHAGA, C. 2023. Proteomics of brain, CSF, and plasma identifies molecular signatures for distinguishing sporadic and genetic Alzheimer's disease. *Sci Transl Med*, 15, eabq5923.
- SVOBODA, K., DENK, W., KLEINFELD, D. & TANK, D. W. 1997. In vivo dendritic calcium dynamics in neocortical pyramidal neurons. *Nature*, 385, 161-5.
- SVOBODA, K. & YASUDA, R. 2006. Principles of two-photon excitation microscopy and its applications to neuroscience. *Neuron*, 50, 823-839.
- SZATKO, K. P., KORYMPIDOU, M. M., RAN, Y., BERENS, P., DALKARA, D., SCHUBERT, T., EULER, T. & FRANKE, K. 2020. Neural circuits in the mouse retina support color vision in the upper visual field. *Nat Commun*, 11, 3481.
- TAKASAKI, K., ABBASI-ASL, R. & WATERS, J. 2020. Superficial Bound of the Depth Limit of Two-Photon Imaging in Mouse Brain. *eNeuro*, 7.
- THEER, P. & DENK, W. 2006. On the fundamental imaging-depth limit in two-photon microscopy. *J Opt Soc Am A Opt Image Sci Vis*, 23, 3139-49.

- THEER, P., HASAN, M. T. & DENK, W. 2003. Two-photon imaging to a depth of 1000 microm in living brains by use of a Ti:Al₂O₃ regenerative amplifier. *Opt Lett*, 28, 1022-4.
- TIAN, L., HIRES, S. A., MAO, T., HUBER, D., CHIAPPE, M. E., CHALASANI, S. H., PETREANU, L., AKERBOOM, J., MCKINNEY, S. A., SCHREITER, E. R., BARGMANN, C. I., JAYARAMAN, V., SVOBODA, K. & LOOGER, L. L. 2009. Imaging neural activity in worms, flies and mice with improved GCaMP calcium indicators. *Nat. Methods*, 6, 875-881.
- TODA, K., ISOBE, K., NAMIKI, K., KAWANO, H., MIYAWAKI, A. & MIDORIKAWA, K. 2017. Temporal focusing microscopy using three-photon excitation fluorescence with a 92-fs Yb-fiber chirped pulse amplifier. *Biomed Opt Express*, 8, 2796-2806.
- TORRADO PACHECO, A., BOTTORFF, J., GAO, Y. & TURRIGIANO, G. G. 2021. Sleep Promotes Downward Firing Rate Homeostasis. *Neuron*, 109, 530-544 e6.
- TRAN, T. P., CHRISTENSEN, H. L., BERTELSEN, F. C. B., BOUZINOVA, E., MOLLER, A. & WIBORG, O. 2016. The touchscreen operant platform for assessing cognitive functions in a rat model of depression. *Physiol Behav*, 161, 74-80.
- VAIDYA, C. J. & GORDON, E. M. 2013. Phenotypic variability in resting-state functional connectivity: current status. *Brain Connect*, 3, 99-120.
- VAN BORKULO, C. D., BORSBOOM, D., EPSKAMP, S., BLANKEN, T. F., BOSCHLOO, L., SCHOEVEERS, R. A. & WALDORP, L. J. 2014. A new method for constructing networks from binary data. *Sci Rep*, 4, 5918.
- VAN DER KOOIJ, M. A., JENE, T., TRECCANI, G., MIEDERER, I., HASCH, A., VOELXEN, N., WALENTA, S. & MULLER, M. B. 2018. Chronic social stress-induced hyperglycemia in mice couples individual stress susceptibility to impaired spatial memory. *Proc Natl Acad Sci U S A*, 115, E10187-E10196.
- VAN NES, E. H. & SCHEFFER, M. 2004. Large species shifts triggered by small forces. *Am Nat*, 164, 255-66.
- VAN VUGT, B., DAGNINO, B., VARTAK, D., SAFAAI, H., PANZERI, S., DEHAENE, S. & ROELFSEMA, P. R. 2018. The threshold for conscious report: Signal loss and response bias in visual and frontal cortex. *Science*, 360, 537-542.
- VELASCO, M. G. & LEVENE, M. J. 2014. In vivo two-photon microscopy of the hippocampus using glass plugs. *Biomed Opt Express*, 5, 1700-8.
- VOSS, P. 2013. Sensitive and critical periods in visual sensory deprivation. *Front Psychol*, 4, 664.
- WANG, Q. & BURKHALTER, A. 2007. Area map of mouse visual cortex. *J Comp Neurol*, 502, 339-57.
- WANG, T., OUZOUNOV, D. G., WU, C., HORTON, N. G., ZHANG, B., WU, C. H., ZHANG, Y., SCHNITZER, M. J. & XU, C. 2018. Three-photon imaging of mouse brain structure and function through the intact skull. *Nat Methods*, 15, 789-792.
- WANG, T., WU, C., OUZOUNOV, D. G., GU, W., XIA, F., KIM, M., YANG, X., WARDEN, M. R. & XU, C. 2020. Quantitative analysis of 1300-nm three-photon calcium imaging in the mouse brain. *Elife*, 9.
- WANG, Y. V., WEICK, M. & DEMB, J. B. 2011. Spectral and temporal sensitivity of cone-mediated responses in mouse retinal ganglion cells. *J Neurosci*, 31, 7670-81.

- WEI, W., HAMBY, A. M., ZHOU, K. & FELLER, M. B. 2011. Development of asymmetric inhibition underlying direction selectivity in the retina. *Nature*, 469, 402-6.
- WENDELMUTH, M., WILLAM, M., TODOROV, H., RADYUSHKIN, K., GERBER, S. & SCHWEIGER, S. 2020. Dynamic longitudinal behavior in animals exposed to chronic social defeat stress. *PLoS One*, 15, e0235268.
- WERNET, M. F., HUBERMAN, A. D. & DESPLAN, C. 2014. So many pieces, one puzzle: cell type specification and visual circuitry in flies and mice. *Genes Dev*, 28, 2565-84.
- WU, C. H., TATAVARTY, V., JEAN BELTRAN, P. M., GUERRERO, A. A., KESHISHIAN, H., KRUG, K., MACMULLAN, M. A., LI, L., CARR, S. A., COTTRELL, J. R. & TURRIGIANO, G. G. 2022. A bidirectional switch in the Shank3 phosphorylation state biases synapses toward up- or downscaling. *Elife*, 11.
- WU, Y. K., HENGGEN, K. B., TURRIGIANO, G. G. & GJORGJIEVA, J. 2020. Homeostatic mechanisms regulate distinct aspects of cortical circuit dynamics. *Proc Natl Acad Sci U S A*, 117, 24514-24525.
- XIAO, Y., DENG, P., ZHAO, Y., YANG, S. & LI, B. 2023. Three-photon excited fluorescence imaging in neuroscience: From principles to applications. *Front Neurosci*, 17, 1085682.
- XU, W. & SUDHOF, T. C. 2013. A neural circuit for memory specificity and generalization. *Science*, 339, 1290-5.
- YANG, J. W., PROUVOT, P. H., REYES-PUERTA, V., STUTTGEN, M. C., STROH, A. & LUHMANN, H. J. 2017. Optogenetic Modulation of a Minor Fraction of Parvalbumin-Positive Interneurons Specifically Affects Spatiotemporal Dynamics of Spontaneous and Sensory-Evoked Activity in Mouse Somatosensory Cortex in Vivo. *Cereb Cortex*, 27, 5784-5803.
- YANG, W., CARRILLO-REID, L., BANDO, Y., PETERKA, D. S. & YUSTE, R. 2018. Simultaneous two-photon imaging and two-photon optogenetics of cortical circuits in three dimensions. *Elife*, 7.
- YANG, Y., WU, M., WEGENER, A. J., VAZQUEZ-GUARDADO, A., EFIMOV, A. I., LIE, F., WANG, T., MA, Y., BANKS, A., LI, Z., XIE, Z., HUANG, Y., GOOD, C. H., KOZOROVITSKIY, Y. & ROGERS, J. A. 2022. Preparation and use of wireless reprogrammable multilateral optogenetic devices for behavioral neuroscience. *Nat Protoc*, 17, 1073-1096.
- YEHUDA, R., FLORY, J. D., SOUTHWICK, S. & CHARNEY, D. S. 2006. Developing an agenda for translational studies of resilience and vulnerability following trauma exposure. *Ann N Y Acad Sci*, 1071, 379-96.
- YING, J., KEINATH, A. T., LAVOIE, R., VIGNEAULT, E., EL MESTIKAWY, S. & BRANDON, M. P. 2022. Disruption of the grid cell network in a mouse model of early Alzheimer's disease. *Nat Commun*, 13, 886.
- YIZHAR, O., FENNO, L. E., DAVIDSON, T. J., MOGRI, M. & DEISSEROTH, K. 2011. Optogenetics in neural systems. *Neuron*, 71, 9-34.
- YONEHARA, K., ISHIKANE, H., SAKUTA, H., SHINTANI, T., NAKAMURA-YONEHARA, K., KAMIJI, N. L., USUI, S. & NODA, M. 2009. Identification of retinal ganglion cells and their projections involved in central transmission of information about upward and downward image motion. *PLoS One*, 4, e4320.
- YUSTE, R. 2015. From the neuron doctrine to neural networks. *Nat Rev Neurosci*, 16, 487-97.

- ZAGHA, E., CASALE, A. E., SACHDEV, R. N., MCGINLEY, M. J. & MCCORMICK, D. A. 2013. Motor cortex feedback influences sensory processing by modulating network state. *Neuron*, 79, 567-78.
- ZARHIN, D., ATSMON, R., RUGGIERO, A., BAELOHA, H., SHOOB, S., SCHARF, O., HEIM, L. R., BUCHBINDER, N., SHINIKAMIN, O., SHAPIRA, I., STYR, B., BRAUN, G., HAREL, M., SHEININ, A., GEVA, N., SELA, Y., SAITO, T., SAIDO, T., GEIGER, T., NIR, Y., ZIV, Y. & SLUTSKY, I. 2022. Disrupted neural correlates of anesthesia and sleep reveal early circuit dysfunctions in Alzheimer models. *Cell Rep*, 38, 110268.
- ZATKA-HAAS, P., STEINMETZ, N. A., CARANDINI, M. & HARRIS, K. D. 2021. Sensory coding and the causal impact of mouse cortex in a visual decision. *Elife*, 10.
- ZEKI, S. 1993. *A Vision of the Brain*, Oxford, UK, Oxford Univ. Press.
- ZHANG, F., WANG, L. P., BRAUNER, M., LIEWALD, J. F., KAY, K., WATZKE, N., WOOD, P. G., BAMBERG, E., NAGEL, G., GOTTSCHALK, A. & DEISSEROTH, K. 2007. Multimodal fast optical interrogation of neural circuitry. *Nature*, 446, 633-639.
- ZHANG, J., ACKMAN, J. B., DHANDE, O. S. & CRAIR, M. C. 2011. Visualization and manipulation of neural activity in the developing vertebrate nervous system. *Front Mol Neurosci*, 4, 43.
- ZHANG, L., PAN, R., CAI, Y. & PAN, J. 2021. The Prevalence of Post-Traumatic Stress Disorder in the General Population during the COVID-19 Pandemic: A Systematic Review and Single-Arm Meta-Analysis. *Psychiatry Investig*, 18, 426-433.
- ZOTT, B., BUSCHE, M. A., SPERLING, R. A. & KONNERTH, A. 2018. What Happens with the Circuit in Alzheimer's Disease in Mice and Humans? *Annu Rev Neurosci*, 41, 277-297.

7. Appendix

[Redacted text block]

7.2 List of publications and presentations

[Redacted text block]

- [Redacted list item]

[Redacted text block]

- [Redacted list item]

- [Redacted list item]

- [Redacted list item]

- [Redacted list item]

■ [REDACTED]
[REDACTED]
[REDACTED] [REDACTED] [REDACTED] [REDACTED] [REDACTED] [REDACTED] [REDACTED]
[REDACTED]

■ [REDACTED]
[REDACTED]
[REDACTED]
[REDACTED]
[REDACTED]

[REDACTED]

[REDACTED]

■ [REDACTED]
[REDACTED]

[REDACTED]

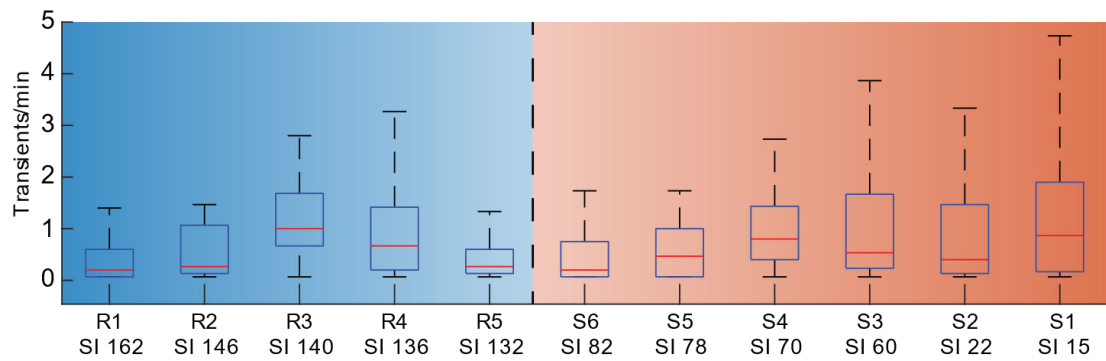
■ [REDACTED]
[REDACTED]
[REDACTED]
[REDACTED] [REDACTED] [REDACTED]

■ [REDACTED]
[REDACTED]
[REDACTED]
[REDACTED] [REDACTED] [REDACTED]

■ [REDACTED]
[REDACTED]
[REDACTED]
[REDACTED] [REDACTED] [REDACTED]

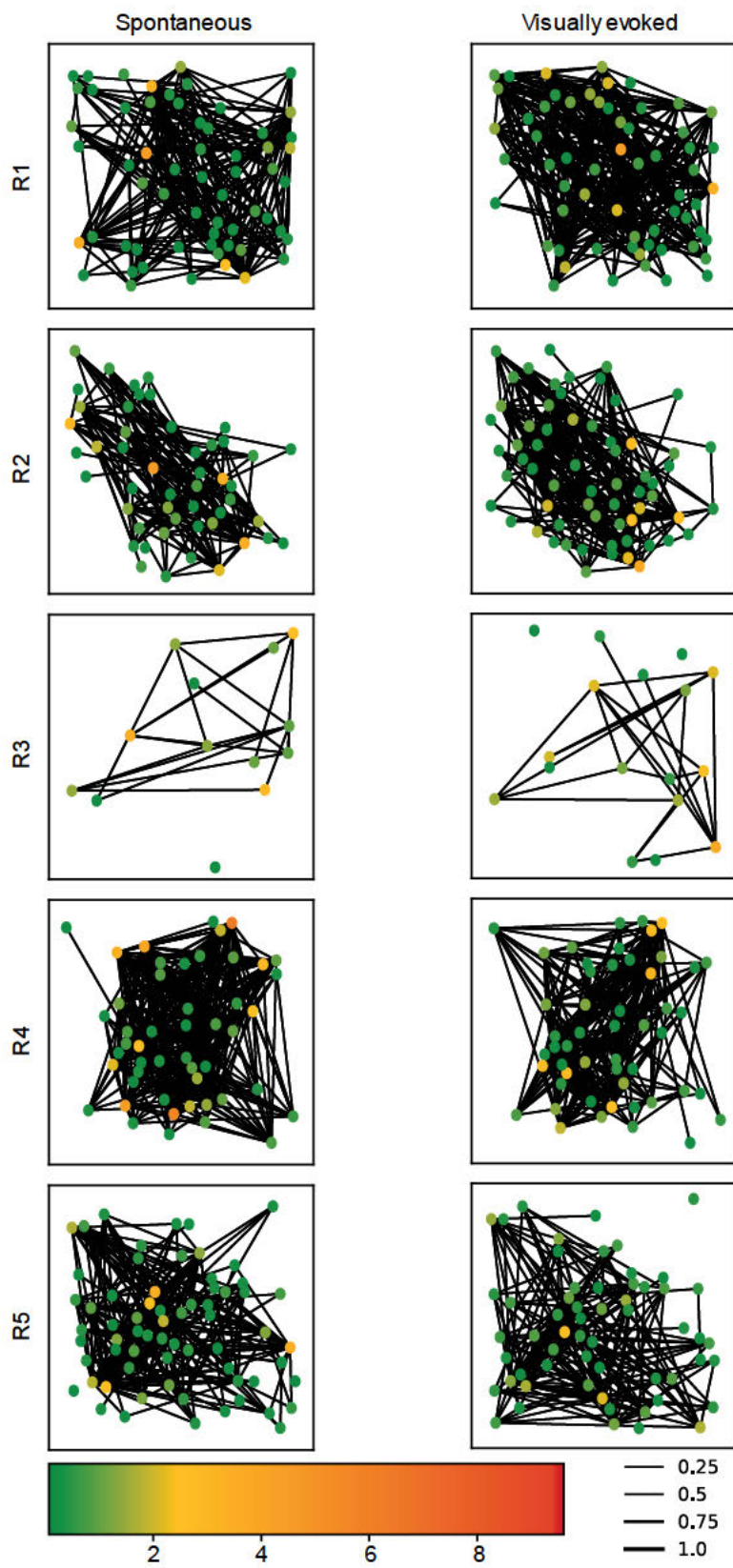
■ [REDACTED] [REDACTED] [REDACTED] [REDACTED] [REDACTED] [REDACTED] [REDACTED]
[REDACTED]
[REDACTED]
[REDACTED] [REDACTED] [REDACTED]
[REDACTED]

7.3 Spontaneous activity per animal



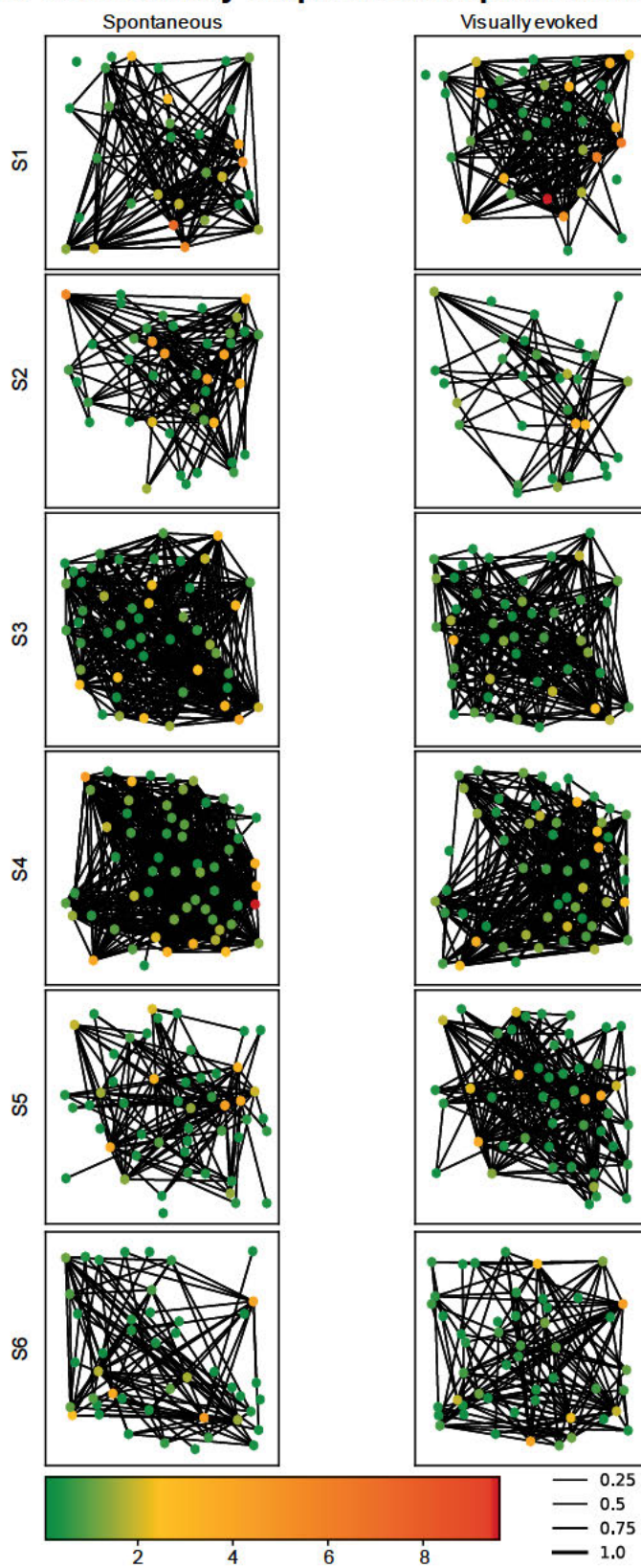
Supplement Figure 1: Boxplot of spontaneous activity frequency per animal. R1-R5 represents animals classified as stress resilient and S1-S6 their stress susceptible litter mates. Even though a tendency towards lower spontaneous activity in the most resilient classified animals (R1-R2) versus an increased activity within the group of most susceptible animals (S1-S3) is observable, also resilient animals can exhibit neuronal activity rates similar to susceptible animals (R3, R4) and vice versa (S6, S5).

7.4 Connectivity maps of resilient animals



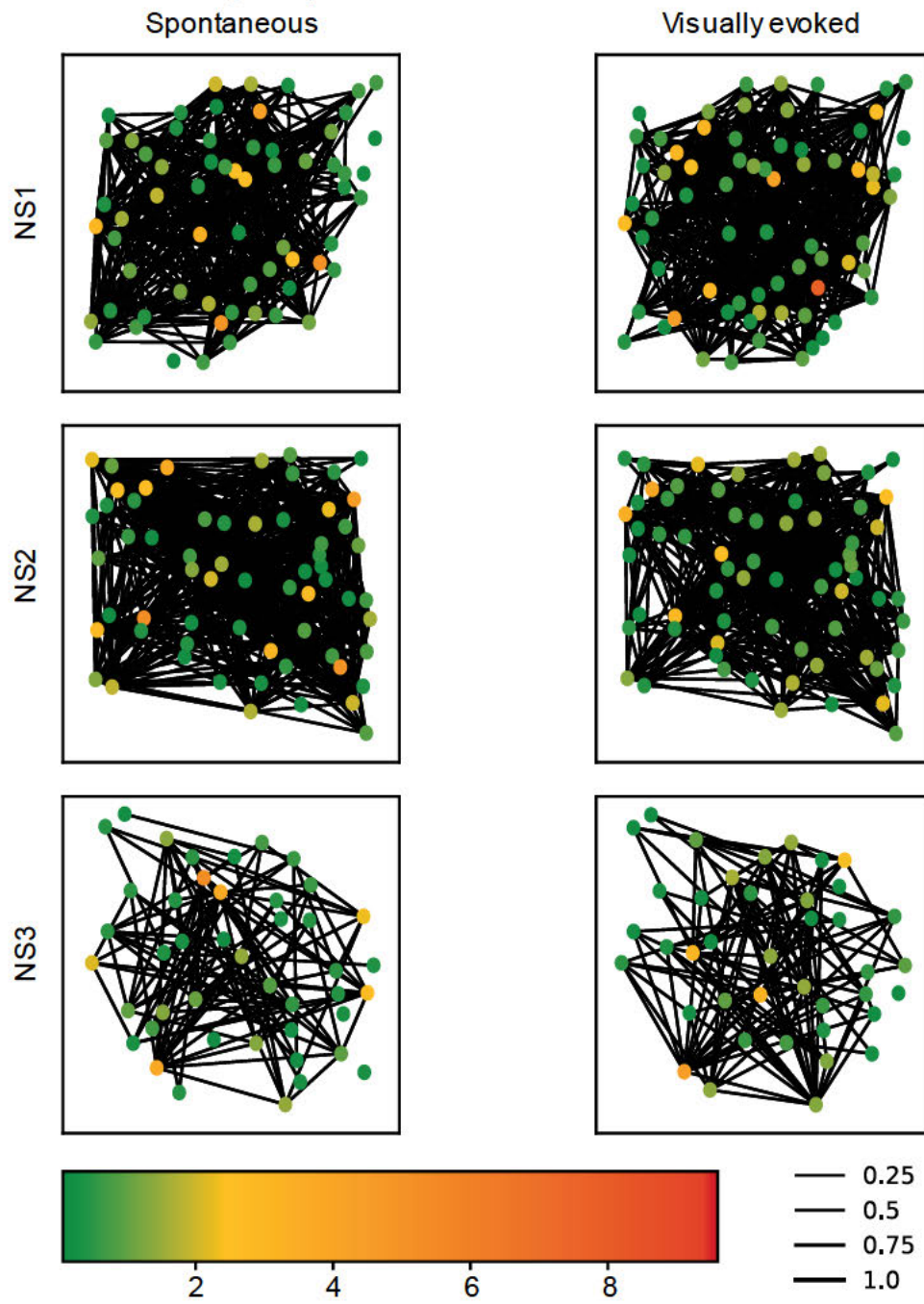
Supplement Figure 2: Overview of connectivity maps of stress-resilient animals.

7.5 Connectivity maps of susceptible animals



Supplement Figure 3: Overview of connectivity maps of stress-susceptible animals.

7.6 Connectivity maps of non-stressed animals



Supplement Figure 4: Overview of connectivity maps of non-stressed animals.